2016

Design and Analysis of Geothermal Wellbore Energy Conversion System Working on Zero Mass Withdrawal Principle

Ildar Akhmadullin
Louisiana State University and Agricultural and Mechanical College, iakhma1@lsu.edu

Recommended Citation
Akhmadullin, Ildar, "Design and Analysis of Geothermal Wellbore Energy Conversion System Working on Zero Mass Withdrawal Principle" (2016). *LSU Doctoral Dissertations*. 4046.
https://digitalcommons.lsu.edu/gradschool_dissertations/4046

DESIGN AND ANALYSIS OF GEOTHERMAL WELLBORE ENERGY CONVERSION SYSTEM WORKING ON ZERO MASS WITHDRAWAL PRINCIPLE

A Dissertation

Submitted to the Graduate Faculty of the
Louisiana State University and
Agricultural and Mechanical College
in partial fulfillment of the
requirements for the degree of
Doctor of Philosophy

in

The Craft and Hawkins Department of Petroleum Engineering

by
Ildar Akhmadullin
B.Sc., Mechanical Engineering, 1996
M.Sc., Mechanical Engineering, 2012
August 2016

To my lovely wife

ACKNOWLEDGEMENTS

The work presented in this thesis was carried out at the Louisiana State University in the School of Engineering, Craft and Hawkins Department of Petroleum Engineering. I would like to express my sincere thanks to the respective department for knowledge and skills I have gained and applied in my work.

I would particularly like to thank my PhD supervisor: Dr. Tyagi, for his mentoring throughout my PhD. Dr.Tyagi believed in my success from the beginning my PhD journey; and I am very proud to be his student.

I would also like to take this opportunity to thank the committee members: Dr. Hughes, Dr. Nandakumar, Dr.Akbari, and Dr. Bourdin for their help in writing this work. Additionally, I would like to mention Dr. Christopher White who started this project in our department.

I gratefully acknowledge financial support for this work from the US Department of Energy under the grant DE-EE0005125.

And finally, I would like to thank my wife Nuriya Khamidullina for her support and encouragement throughout the entire PhD experience.

TABLE OF CONTENTS

LIST OF TABLES

LIST OF FIGURES

NOMENCLATURE

a	Semi major axis of ellipse
A_{tubes}	Surface area of condenser tubes
$A_{cond.}$	Condenser area
b	Semi minor axis of ellipse
c	Distance between producer and injector
$Cp_{bulk.}$	Bulk specific heat
Cp_{wf}	Working fluid specific heat
CC	Capital cost
$C_{O\&M}$	Operation and maintenance cost
$C_{tot.}$	Total cost
$CC_{Cond.}$	Condenser cost
D_{prod}	Depth of production side of the well
D_{inj}	Depth of injection side of the well
D_{inner}	Inner diameter
D_{outer}	Outer diameter
D_{prod}	Depth of production side of the well
$D_{an2,i}$	DHE annulus 2 inner diameter
D_{inj}	Depth of injection side of the well
D_{a2}	Annulus 2 diameter
D_{well}	Well outer diameter
D_{DHE}	DHE diameter
D_h	Hydraulic diameter of working fluid stream
D_{tubes}	Condenser tubes diameter
$f_{I.}$	Installation expenses correction factor
$f_{M.}$	Material correction factor for cost determination
f_{perf}	Friction coefficient at the perforated wall
$f_{P.}$	Pressure correction factor for PC cost determination
f_{tot}	Total friction coefficient
f_{wall}	Friction coefficient at the circular wall
g	Gravitational acceleration
h_{wf}	Working fluid heat transfer coefficient

h_{air}	Air heat transfer coefficient
$h_{in.turb}$	Enthalpy at the turbine inlet
$h_{out.turb.}$	Enthalpy at the turbine outlet
$h_{DHE.out.}$	Enthalpy at the DHE outlet
H	Reservoir height
k_M	Thermal diffusivity
k_{rock}	Reservoir rock thermal conductivity
K	Reservoir permeability
$k_{br.}$	Reservoir brine thermal conductivity
L_{tubes}	Length of condenser tubes
L	Reservoir length
L_{DHE}	DHE length
$L_{ins.}$	Distance between producer and injector
$L_{inj.}$	Injection side length
L_{prod}	Production side length
$\dot{m}_{air}$	Air mass flow rate
$\dot{m}_{influx}$	Influx flow rate
$\dot{m}_{wf.}$	Working fluid mass flow rate
n_{tubes}	Number of tubes in the condenser
$Nu_{br.}$	Nusselt number of brine flow
M	Dimensionless ratio of reservoir bulk to brine thermal capacities
$P_{\substack{(pump)\\ in}}$	Inlet pressure of the pump
$P_{\substack{(pump)\\ out.}}$	Outlet pressure of the pump
$P_{br.pump}$	Brine pump pressure
P_{res}	Reservoir pressure
ΔP_{res}	Pressure drop in reservoir
ΔP_{perf}	Pressure drop at perforations
$\Delta P_{\substack{prod.\\ well}}$	Pressure drop in production side of the well
$\Delta P_{\substack{inj.\\ compl.}}$	Pressure drop in injection side of the well
$\Delta P_{ins.}$	Pressure drop in the circular section of the well
$\Delta P_{cond.}$	Pressure drop through the condenser

Pr	Prandtl number
$q_{br.}$	Brine volumetric flow rate
q_{x0}	Reservoir volumetric flow rate per unit legnth
$\dot{Q}_{Rej.}$	Rejected heat rate from the system
$\dot{Q}'''_{rock}$	Heat rate per unit volume extracted from reservoir rock
$\dot{Q}'''_{br.}$	Heat rate per unit volume extracted from reservoir brine
$(\dot{Q})_{DHE}$	Heat rate extracted by the DHE
Re	Reynolds number
$R_{an2/a1}$	Thermal resistance between annuluses 2 and 1
R_t	Thermal retardation factor
$\dot{S}_{gen}$	Entropy generation rate
ΔS	Entropy change
St	Stanton number
$T_{air.cold}$	Air temperature cold side
$T_{air.hot}$	Air temperature hot side
$T_{w.f.cold}$	Working fluid temperature cold side
$T_{w.f.hot}$	Working fluid temperature hot side
T_R	Reservoir temperature
$T_{br.}$	Brine temperature
T_{rock}	Rock temperature
ΔT_{DHE}	Pinch point temperature at the HDE
$\Delta T_{cond.}$	Pinch point temperature at the condenser
$\Delta T_{lm.cond}$	Log-mean temperature
$\Delta T_{w.f.pump.}$	Temperature gain after working fluid pump stage
$T_{avg.}^{annual}$	Annual average temperature
T_{day}	Day ambient temperature
T_{night}	Night ambient temperature
T_{summer}	Summer average temperature
T_{winter}	Winter average temperature
$T_{air.out}$	Air temperature at the outlet of the condenser
T_{an1}	Annulus 1 temperature
T_{an2}	Annulus 2 temperature
T_t	*w.f.* temperature inside the tubing

t	Time
t_D	Dimensionless time
U	Overall heat transfer coefficient
u	Fluid velocity
u_{a2}	Fluid velocity in the annulus 2
U_{cond}	Overall heat transfer coefficient at the condenser
V_{air}	Air velocity
V_R	Reservoir volume
$V_{therm.}$	Thermal front velocity
W	Reservoir width
$(\dot{W})_{\substack{br.\\pump.}}$	Brine pump work
$(\dot{W})_{electr.}$	Work rate
$\dot{W}_{fan}$	Fan power
$(\dot{W})_{Turb.}$	Turbine work
$(\dot{W})_{\substack{w.f.\\pump.}}$	Working fluid pump work
x_s	Stagnation point coordinate in x-direction
x	Horizontal direction coordinate
X	Reservoir drainage parameter
x_D	Dimensionless distance
x_{th}	Thermal front distance
$x_{br.}$	Brine flow distance
y	Vertical direction coordinate
y_s	Stagnation point coordinate in y-direction
Z	Reservoir depth

GREEK LETTERS

α	Well inclination angle
η_c	Carnot efficiency
$\eta_{cond.}$	Condenser efficiency
η_{fan}	Fan efficiency
$\eta_{gen.}$	Generator efficiency
$\eta_{mech.}$	Mechanical efficiency
η_{PC}	Power cycle efficiency
$\eta_{turb.}$	Turbine efficiency
θ	Stream line angle from the origin to the flowing node
λ	Overall thermal conductivity
$\mu_{br.}$	Brine viscosity
$\mu_{w.f.}$	Working fluid viscosity
π_i	Dimensionless number
ρ_{bulk}	Bulk density
$\rho_{br.}$	Brine density
$\Delta\rho_{wf}$	Working fluid's density difference between cold and hot streams
$\rho_{wf.cold}$	Working fluid cold stream density
$\rho_{wf.hot}$	Working fluid hot stream density
τ	Temperature ratio
Φ	Potential
ϕ	Porosity
ψ	Stream function
ω_1	Daily period
ω_2	Seasonal period

ABBREVIATIONS

DHE	Downhole heat exchanger
D&C	Drilling cost
ESP	Electric submersible pump
FRT	Fluid residence time
HES	Heat extraction subsystem
HRS	Heat rejection subsystem
ID	Inside diameter
LCOE	Levelized Cost of Electricity
MD	Measured depth
OD	Outside diameter
O&M	Operation and maintenance
ORC	Organic Rankine cycle
PC	Power cycle
PGS	Power generation subsystem
TD	Target depth
Spf	Shots per foot
w.f.	Working fluid
ZMW	Zero mass withdrawal

ABSTRACT

This project is sponsored by the Department of Energy of the United States and dedicated to development of electricity production from the low-enthalpy geothermal reservoirs. The prime interest are reservoirs that are characterized by low temperature of heat source located in deep saline aquifers with high permeable rock. Usually energy production from these resources are not economical by using a conventional binary power plant approach. The presented PhD work is a study of a new system that utilizes a single-well technology and working on supercritical power cycle (PC). The wellbore energy conversion system is operating with Zero Mass Withdrawal (ZMW) principle, which implies no geo-fluid pumping to the surface facility.

This study introduces analyses of three main subsystems of the power unit. The heat extraction subsystem (HES) is located at the reservoir depth. The power generation subsystem (PGS) is represented by power cycle, and the heat rejection subsystem (HRS) contains an air driven condenser as the only part located on the surface. Several working fluids were examined. Based on the thermodynamic study the best working fluid choice is carbon dioxide.

The project includes a simplified mathematical model derived from energy balance equations for each subsystem. Dimensionless analysis is performed in order to connect subsystems of different scales and show energy flow from the reservoir to the surface environment.

The reservoir prototype is a hot saline aquifer located in Vermilion Parish, LA. The numerical model illustrates application of the ZMW method to the energy production from this reservoir. The maximum net power production is constrained by the power spent on a brine pump, which is a function of frictional losses in the downhole heat exchanger (DHE). The numerical investigation defines the optimal operating brine flow regime for the maximum net power production.

One of the qualitative parameters of this design scheme is a thermal breakthrough time of injected cooled brine flowing toward the production side. This parameter is derived using potential flow theory application for several cases of flowing reservoirs, and various brine flow rates.

The project contains an economic analysis based on determination of Levelized Cost of Electricity (LCOE). The results are in a good agreement with references and show competitive results for low-enthalpy reservoir exploration in terms of electric power production.

CHAPTER 1: INTRODUCTION

“Modern technology owes ecology an apology”
Alan M. Edison

1.1 What is Geothermal Energy?

The economic development over the last century has involved an important growth in energy consumption. The energy production from coal and natural gas together constitutes up to 66% of the overall energy production according to US information administration report (2015) (Figure 1.1). This sector has a long history and well-developed technology starting from mining of natural resources up to the building energy production plants oriented on a simple burning process. As a result, there are several side effects we face nowadays, which include a greenhouse consequence, atmospheric pollution, and national energy dependence.

One of the promising substitutes for the fossil fuel power plants are renewable energy sources, which does not require fuel supply. The energy production comes from solar, wind, or geothermal resources. While the first two have some application limits, the geothermal energy is always available 365 days a year, green, safe, sustainable, and long term oriented (DiPippo, 2004).

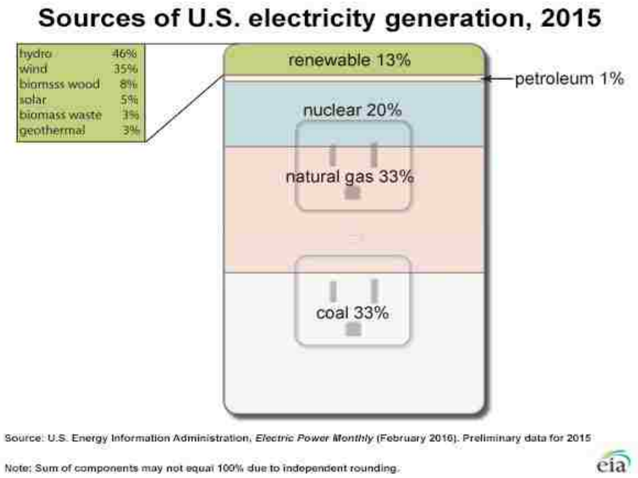

Figure 1.1: The US electric power generation by energy source (US Energy Information Administration, 2015).

The geothermal reservoirs are located at the Earth's depth and include three main features: geo-fluid, heat, and permeability created by sedimentation process. The fluid is mostly a water brine containing dissolved salts and gases. The heat source comes from the constant decay of radioactive isotopes, mainly ^{40}K, ^{232}Th, ^{235}U and ^{238}U, stored in the crust and mantle of the Earth. The energy is distributed between the constituent host rock and a geo-fluid and quantitatively can reach up to 56,000 EJ (10^{18}) (Papadopolus et al., 1975). Theoretically, this heat amount can supply all of mankind's energy needs for six million years (Lund, 2007).

The geothermal resources diverse by the range of temperatures and depths which vary by place. According to the Figure 1.2 (left) the temperature distribution of the US map area ranges with depth. The sediment thickness diverges from location to location (Figure 1.2 on the right). Comparing these data one can conclude that geothermal aquifers are mostly located at the depths deeper than 4 km and have a temperature range of 100-200℃ only, which classifies them as low enthalpy reservoirs.

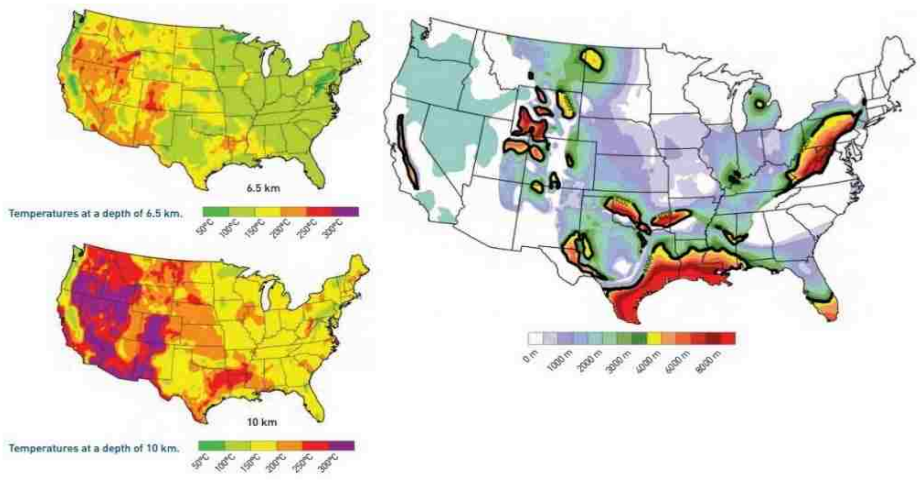

Figure 1.2: Temperature and sediment thickness map of the US area (EERE 2011).

The geothermal energy extraction process is associated by the number of problems. Firstly, the portion of the geothermal heat that can be transformed to electric power is restricted by the thermo-mechanical conversion processes. Due to inability of receiving steam at the surface a binary power cycle is included into the design. In this case a working fluid (*w.f.*) is a refrigerant having low boiling point. The steam production takes place at the surface facility utilizing heat from the extracted brine. The cycle efficiency of such power plants varies from 8 to 17% (DiPippo, 2004) and depends on hot and cold sides of the system.

Power is a function of brine and *w.f.*'s flow rates, as well as ambient and produced brine temperatures. Therefore, in order to maintain the same amount of power, the temperature reduction of the heat source leads to increasing brine flow rate (EERE, 2011). Table 1.1 presents some successful examples of small binary power plants. As it is seen from the Table 1.1 the efficiency does not go over 8.5% regardless of flow rates and produced power. The hydrocarbons produce higher net power than conventional refrigerants, however, require higher input temperature (DiPippo, 2008).

Table 1.1: Main characteristics of small size binary power plants.

Power plant	Power MW	LCOE $/kWh	Cycle efficiency %	Brine flow rate kg/sec	Well depth ft	Brine temperature ℃/F	Binary fluid and flow rate kg/s
Wabuska, Nevada[1]	1.2	0.06	8	60	350	103/218	Iso-Pentane N/A
Amedee, California[1]	1.5	0.045	5.8	205	850	104/219	R-114 N/A
Heber, California[2]	33.5	0.05	8.5	360	1,300	182/360	Mixture of iso-butane and iso-pentane 97.00
Chena, Alaska[3]	0.4	0.05	8.2	33	713	76/169	R-134a, 12.16

1 EERE, 2011
2 DiPippo, 2012
3 Erkan et al., 2008

There are other obstacles that make energy production from low-enthalpy reservoirs unattractive. Expensive deep drilling operation consumes a huge portion of the plant's installation cost (Lukawski, 2009). High operation and maintenance (O&M) costs are associated with geothermal well clogging problems. Also, it is obligatory by the US law to have a geo-fluid purification station before the injection, where hydrocarbons and other dissolved minerals are extracted from the brine for utilization. Additionally, long plant build up period leads to high cost of produced electric power. Therefore, there is a strong demand in a new design or technology that can makes low-enthalpy geothermal resources economically viable.

1.2 Zero Mass Withdrawal Method

A new approach of heat extraction from low-enthalpy aquifers seems possible by utilizing a down-hole heat exchanger. This method is called Zero Mass Withdrawal method. The system does not require geo-fluid extraction to the surface. One of the big advantages is a compact design that utilizes only a single well. (Feng et al., 2015). Figure 1.3 illustrates the comparison of both design schemes: traditional and ZMW cases.

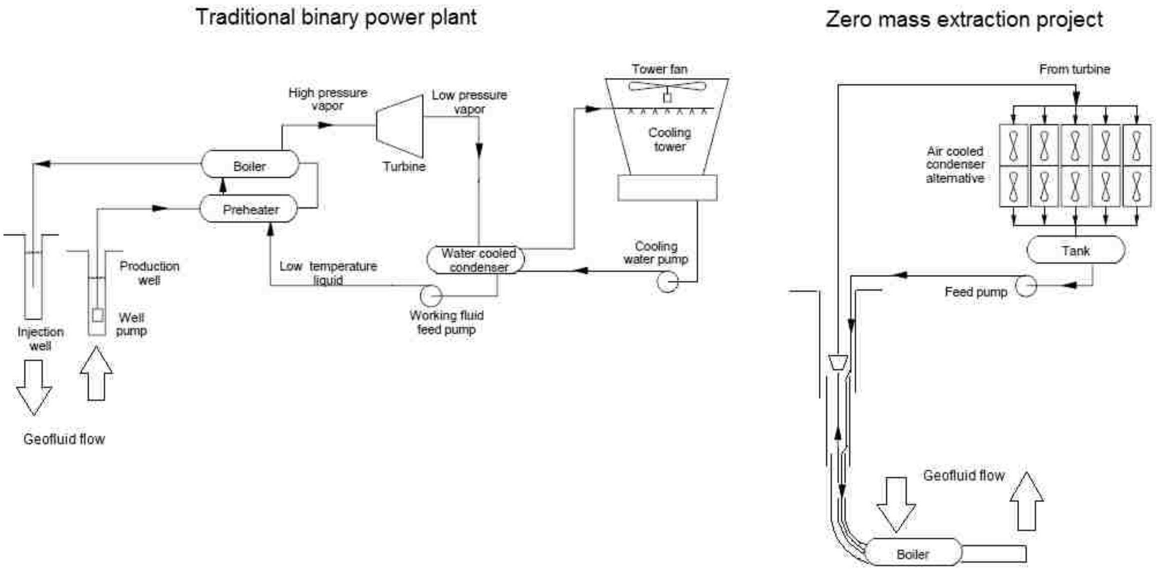

Figure 1.3: Traditional and proposed design schemes.

The traditional way requires a minimum of two wells: production and injection. The binary cycle including cooling tower and additional facilities consumes large surface area. To cover all installation expenses and get low LCOE the plant is required to produce high amount of electric power. The ZMW design employs reservoir brine circulation through the DHE located at the reservoir depth. The compact size of the turbine-generator assembly allows installation inside of the well. Only a condenser and electric power control unit are located on the surface. Therefore, this design significantly reduces the size of the surface facility and installation cost of the project (Kaiser, 2016). The system may produce smaller amount of electric power, however, the ratio of cost to net power production is expected to be higher than in the traditional case. The application of this system may be energy production for local usage: industrial manufacturing plant, living community, or petroleum industry production facilities.

1.3 Reservoir Prototype

The geo-pressured hot aquifer located near the Gueydan salt dome in Louisiana, Vermillion Parish was chosen as a reservoir prototype (Figure 1.4). The reservoir has a true vertical depth between 4253 and 4479 meters and varying dipping angles from 1.2 to 28 degrees. The 100m thickness A-sand stratum is characterized by average 12 mD permeability and 9 to 31 percent porosity. The temperature gradient consists of two parts: 23.04°C/1km from the surface to the top of the geo-pressured zone (3827 m); and 28.9°C/1km in the pressured zone (Gray, 2010).

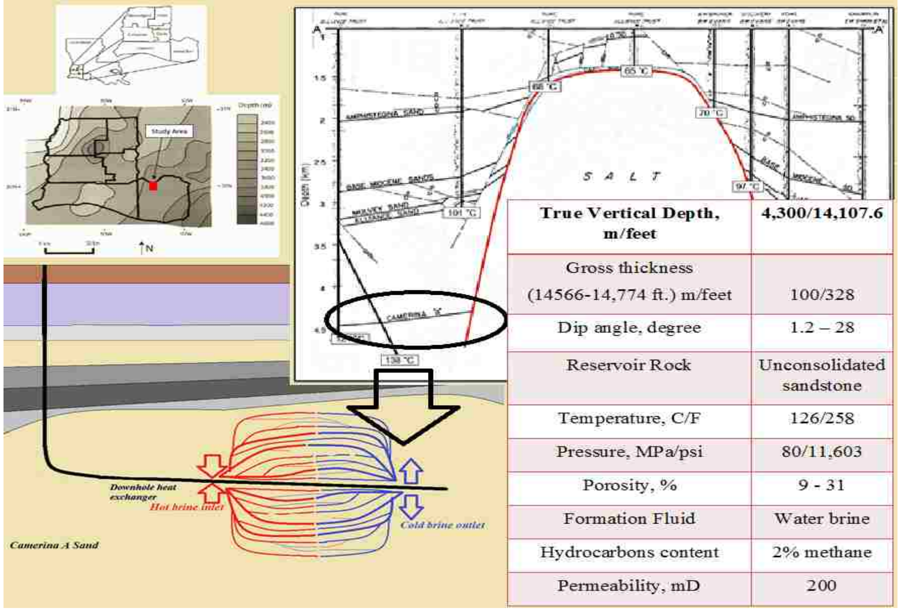

True Vertical Depth, m/feet	**4,300/14,107.6**
Gross thickness (14566-14,774 ft.) m/feet	100/328
Dip angle, degree	1.2 – 28
Reservoir Rock	Unconsolidated sandstone
Temperature, C/F	126/258
Pressure, MPa/psi	80/11,603
Porosity, %	9 - 31
Formation Fluid	Water brine
Hydrocarbons content	2% methane
Permeability, mD	200

Figure 1.4: Reservoir prototype (modified from Gray, 2010).

The top of pressured zone creates higher geothermal gradients which results in slightly higher temperatures for the formation than if it were hydrostatically pressured. Also, the Gueydan salt dome works as a heat carrier, which transfers thermal energy from the deeper layers to the reservoir (Gray, 2010).

Several exploration wells were drilled previously. The tests showed no sand content in the extracted brine, and high permeability and porosity of the reservoir rock (Durham, 1978). For these reasons, Camerina A sand can be one of the most geologically feasible sedimentary sand deposition reservoir in case of energy production (MIT report, 2010).

1.4 Research Aim and Scope

The motivation of this project is to design and analyze a system that is able to compete with traditional fossil fuel power plants in energy production rate for a long operation time. This study is expected to make positive impact on the development of low-enthalpy energy sources in the future.

There are several objectives to this dissertation. The first objective is to construct the design of a single wellbore energy conversion system. The second aim is to choose an optimal working fluid, and power cycle components. Based on these designs perform parametric study and define the most influencing features affecting the net power production for thirty years of operational life. Then, analyze the system for applicability to the range of low-enthalpy geothermal aquifers with different temperatures and permeabilities in order to gain the maximum possible net power production with respect to the cost of produced electric power.

Chapter 2 summarizes the state of the art of the binary Organic Rankin Cycle (ORC) technology used in geothermal energy production and introduces the new design scheme and the main parts of the system.

Chapter 3 derives a simplified analytical model and presents dimensionless analysis in order to connect subsystems of different scales: reservoir, well, and surface condenser into one equation. The examination of this equation illustrates the main factors affecting the net power production.

Chapter 4 make a comparison of potential working fluid (*w.f.*) candidates, examines the net power production of the cycle through the thermodynamic analysis.

Chapter 5 defines the main constraints of the system and presents numerical analysis based on reservoir prototype data. This chapter also includes the parametric study of the coaxial DHE and the system itself.

Chapter 6 contains breakthrough time analysis based on potential flow theory.

Chapter 7 discusses the thermo-economic evaluation of the project based on Levelized Cost of Electricity determination for thirty years of operational life.

Chapter 8 concludes the results and discussions and gives some ideas for future research development.

CHAPTER 2: ZMW DESIGN SCHEME. INTRODUCTION

“If you cannot measure it, you cannot improve it”
Lord Kelvin

2.1 Proposed Design

The well has a vertical and horizontal sections. The heat exchanger is installed into the cased horizontal portion of the well at the reservoir depth. The coaxial DHE scheme simplifies the installation process and allows using industry available parts. Horizontal orientation gives a maximum heat transfer area exposed directly at the heat source (Figure 2.1). The *w.f.* and geo-fluid loops do not mix with each other and have a thermal interaction through the DHE (Feng, 2015).

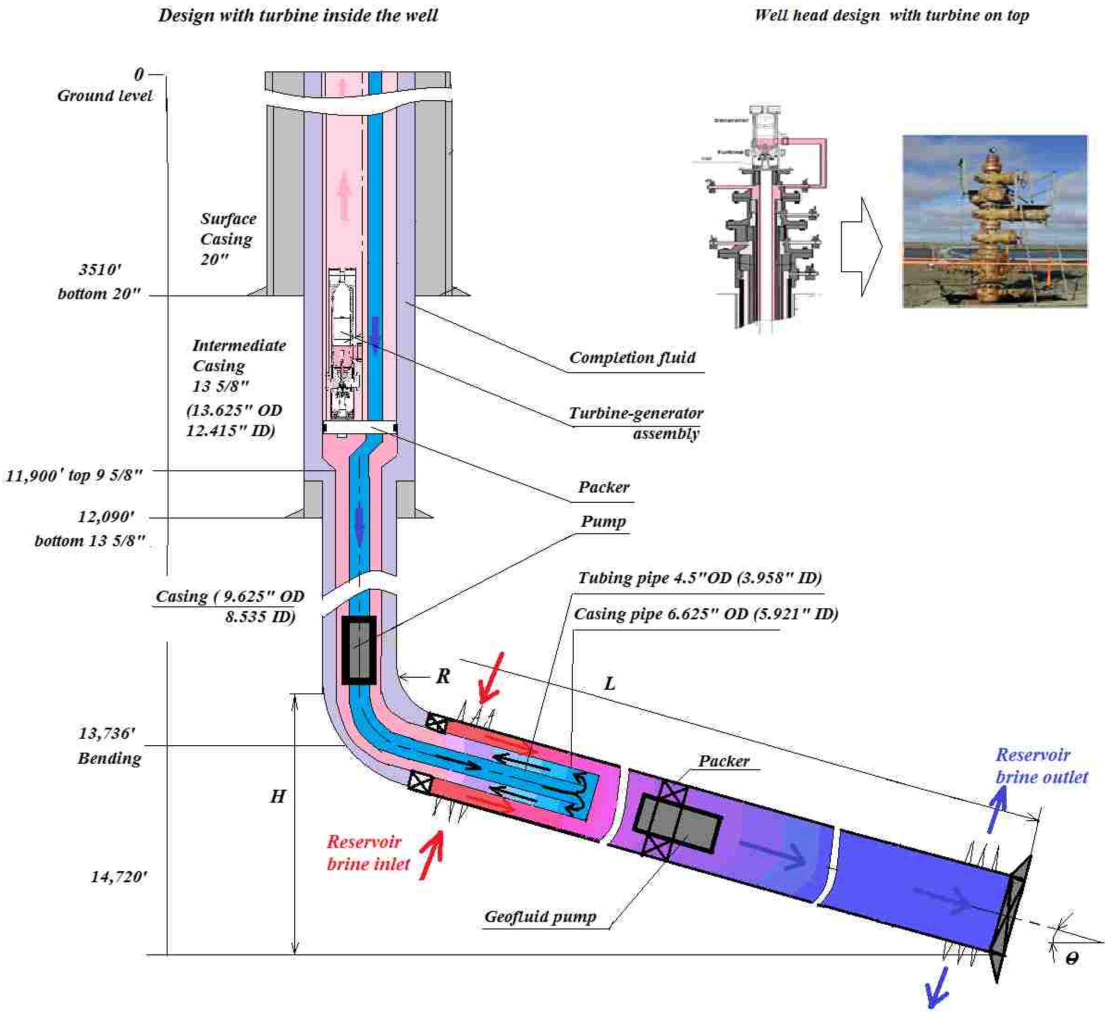

Figure 2.1: Zero mass extraction power unit schematic (not to scale).

As it is shown in the Figure 2.2 the horizontal section has production and injection sides. An electric submersible pump (ESP) drives brine from the DHE installed in the producer, circular portion of the well (insulator) and discharges back to the reservoir through the injection side. There is a risk of sand production if the reservoir rock is unconsolidated. To avoid DHE fouling and horizontal well clogging a gravel packed design is considered as a protection method at the production side. The well may have some inclination according to the reservoir dipping direction.

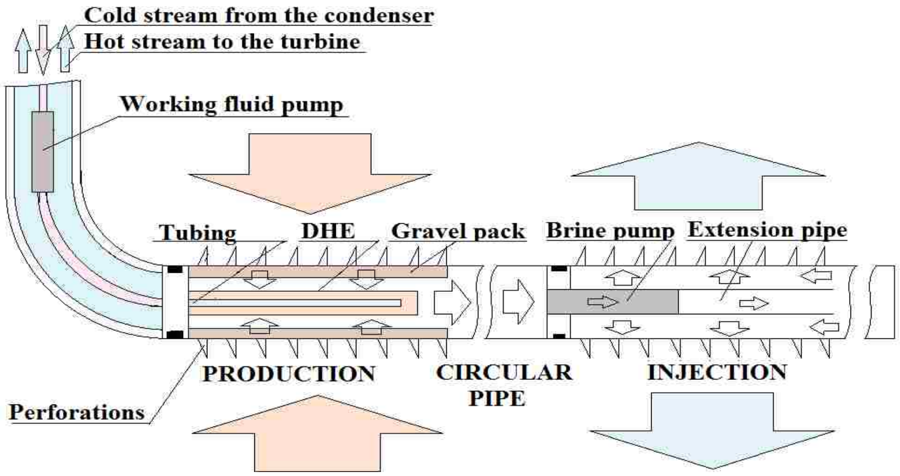

Figure 2.2: Completion design scheme for horizontal well with downhole heat exchanger.

A power cycle utilizes hot *w.f.* and produces electric power in the generator, which is connected to the turbine’s shaft through a reduction gearbox. The compact expander is installed on the top of the retrievable packer inside of the vertical well or on top of the christmas tree as shown in the Figure 2.1. The first case has more compact design but requires workover operation to dismantle the turbine for maintenance. The second case is much simpler in terms of installation and maintenance work, however, may require some development of the christmas tree. In this way the casing design might be simplified avoiding installation of tubing with changing cross sectional area.

After the expansion the discharged *w.f.* enters the condenser. An air driven condenser is used to convert vapor to liquid form. Later, the condensed *w.f.* is pumped down to the reservoir depth through the vertical insulated tubing. The fluid’s density is increased under the influence of high hydrostatic pressure proportional to the reservoir depth. Therefore, a working fluid pump is installed at the deepest possible vertical location of the tubing to reduce the pump work. After increasing temperature in the DHE the *w.f.* leaves the horizontal offset and travels vertically up toward the turbine through the annulus of variable cross sectional area.

2.2 Design of the Main Parts of the System

2.2.1 Expander

A turbine is a heat engine which is used to extract energy from the hot steam and turn it to kinetic energy of a shaft rotation. Then, kinetic energy is converted to electric power in the generator. The turbine design is not a primary interest of this project, however, the efficiency of the expander is needed for numerical for calculations. Therefore, the following chapter contains a brief literature overview of a turbine selection criteria and efficiency analysis.

A number of selection methodologies have been suggested for the different types of expanders (Balje, 1981; Dixon & Hall, 2010; Japikse & Baines, 1995; and Quoilin et al., 2013). Quoilin et al. (2013) proposed a selection method for scroll expanders, screw expanders and radial turbines based on nominal power. However, the most convenient classification is based on the turbine specific speed and diameter as is illustrated in Figure 2.3 (Balje, 1981; Dixon & Hall, 2010; Japikse & Baines, 1995).

The proposed design deals with high flow rates and high pressure ratios. A compact size expander is operating with single phase *w.f.*, therefore, the choice of a turbine falls in the region of radial and axial types in Figure 2.3, highlighted by the orange color box. The main difference between both types is flow organization. The inflow path in the radial turbines is perpendicular to the shaft axis. A single stage rotor orientates the flow at 90 degrees, which makes them highly efficient, up to 90%, at very low power output. The bearing load is much better distributed and the design provides long term operation. Additionally, the work per stage value is much higher, than in axial turbines (Japikse & Baines, 1995). However, the axial turbines can deal with higher pressure ratios and have more convenient flow path design. The flow direction coincides with the turbine axis and is more convenient in installation inside the well. Therefore, the choice is given to a multistage axial turbine.

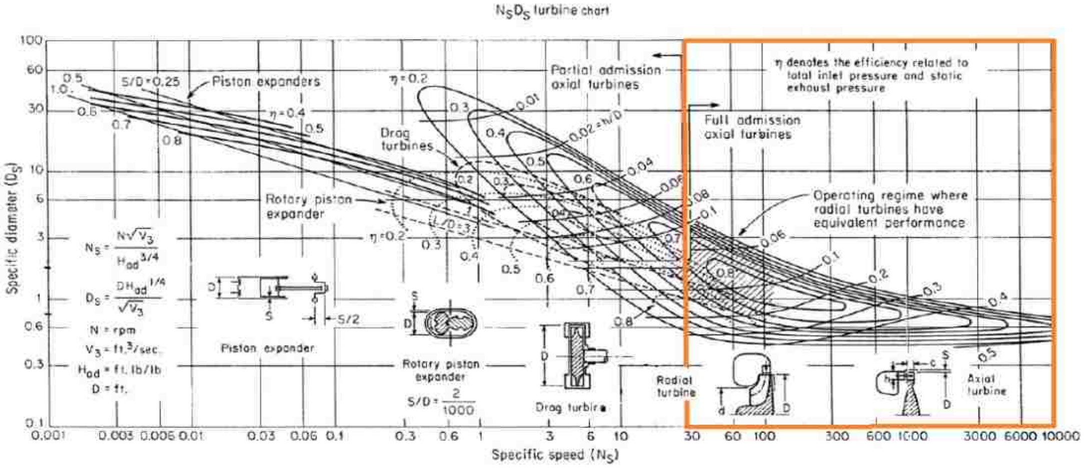

Figure 2.3: Turbine selection chart after Balie (1981).

The expander efficiency determination is based on the choice of the expander, *w.f.* properties, mass flow rate, and geometry of the blades. The design procedure starts from defining the inflow and outflow velocity triangle on the blade and finishing with produced work calculation (Church, 1959). The procedure is shown in the Appendix A, and results are summarized in Table 2.1. The expander is able to utilize 10 kg/sec *w.f.* mass flow rate with efficiency of 0.814. A single stage turbine has small diameter blades of 2.5 inch. The shaft has high revolutions of 19,018 rev/min, and, therefore, requires reduction box installation to connect with generator unit.

Table 2.1: Results of a single stage turbine calculations

Fluid	Turbine blade radius, inch	Turbine efficiency	Shaft Rev/min	Number of stages	Pressure inlet MPa	Pressure outlet MPa	Mass flow rate kg/sec
CO_2	2.5	0.814	19,018	1	21.27	8	10

The electric power produced by the turbine $(\dot{W})_{electr.}$ is calculated by equation 2.1:

$$(\dot{W})_{electr.} = \dot{m}_{wf.}(h_{in} - h_{out})_{vert.}\eta_{turb.}\eta_{gen.}\eta_{mech.} \tag{2.1}$$

where $\eta_{turb.}\eta_{gen.}\eta_{mech.}$ are turbine, generator and mechanical efficiencies.

Figure 2.4 illustrates the single stage turbine expansion process. Carbon dioxide was utilized as a working fluid operating at temperature range from 120°C to 30°C, and pressure range of 22MPa to 8MPa. The red line represents the two-phase boundary region. The dashed line is a constant entropy expansion (ideal case with 100% efficiency), and arrow shows the real turbine expansion with 0.81 efficiency. With 10 kg/s flow rate the calculated turbine work is 319.4 kW. To convert this work into electric power the generator efficiency of 0.96 and gearbox efficiency of 0.97 were assumed (Quoilin et al., 2013). The resulting electric power is 297.4 kW for a single turbine.

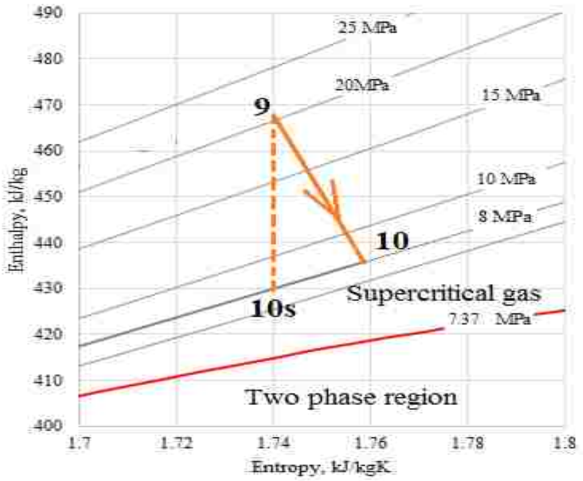

Figure 2.4: Turbine expansion Enthalpy-Entropy chart.

2.2.2 Condenser

Cooling of *w.f.* after the turbine stage is an important design aspect. The temperature drop in the condenser represents the bottom line of the T-S diagram and influences the overall power produced by thermodynamic cycle (Moran and Shapiro, 2006). An implementation of a traditional cooling tower or cooling pond is not always possible because water source may not be available at the well location (Varney et al., 2012). An air cooling condenser is comparatively cheap and easy to install (Wendt et al., 2011). There are many commercially available coolers ready to implement in this project, however, they are designed for a particular working fluid (R-22 or R134a) and cannot be simply applied to this project.

A condenser design was performed in order to define the necessary heat rejection area required to cool the power cycle. This area is a constant parameter and stands as constraint for the power unit design. It cannot be changed during operating life and may restrict the amount of heat rejected by the condenser. Rejected heat from the system $(\dot{Q}_{Rej.})$ is found from equation 2.2:

$$\dot{Q}_{Rej.} = U_{cond}\, A_{tubes} \Delta T_{lm.cond} \tag{2.2}$$

where U_{cond} is overall heat transfer coefficient; $\Delta T_{lm.cond}$ is log-mean temperature; A_{tubes} is heat transfer area of the condenser tubes, which can be simplified by the number of tubes (n_{tubes}) used in the design.

$$A_{tubes} = n_{tubes} \pi D_{tubes} L_{tubes} \tag{2.3}$$

where D_{tubes} and L_{tubes} are outer diameter and length of the condenser tubes.

There are several arrangements of placing tubings in the condenser (Incopera, 1990). Additionally, to reduce the heat transport area and make a condenser compact the designer may use finned tubings. This project is not interested in finding the optimal condenser design for the power unit, so a single row arrangement is implemented to track the condenser surface area.

The overall heat transfer coefficient (U_{cond}) is a function of convective heat transport from the *w.f.* to the ambient air with assumption of negligible conduction resistance through the tubing wall (Incopera, 1990).

$$U_{cond} = \frac{1}{\frac{1}{h_{wf}} + \frac{1}{h_{air}}} \tag{2.4}$$

where h_{wf} and h_{air} are heat transfer coefficients of *w.f.* and air.

The log mean temperature ($\Delta T_{lm.cond}$) of the condenser is a function of cold and hot sides of the air and *w.f.* streams:

$$\Delta T_{lm.cond} = \frac{\left(T_{w.f.hot} - T_{air.hot}\right) - \left(T_{w.f.cold} - T_{air.cold}\right)}{ln \dfrac{\left(T_{w.f.hot} - T_{air.hot}\right)}{\left(T_{w.f.cold} - T_{air.cold}\right)}} \tag{2.5}$$

In the equation 2.4 the overall heat transfer coefficient should be found from the numerical modelling. The simulator is mimicking a commercial cooler with parallel horizontal tubes and vertical air flow created by electric fan (Figure 2.5). The analysis is shown in the Appendix B.

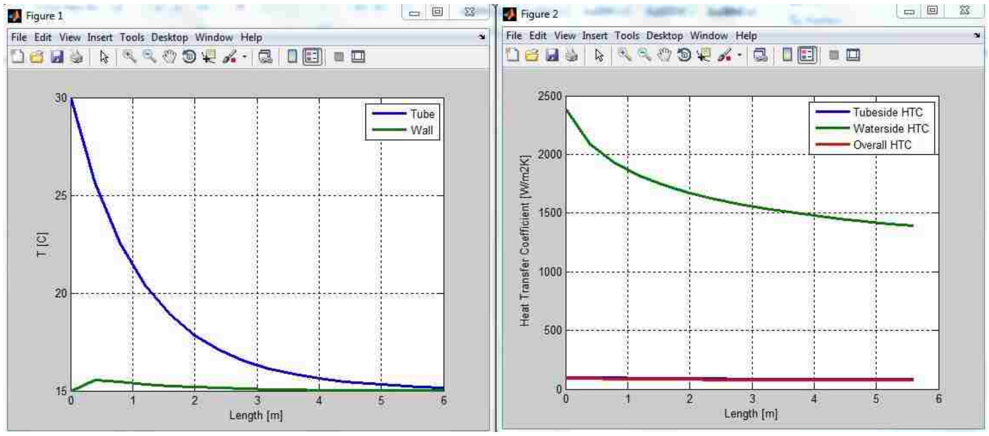

Figure 2.5: The condenser simulation results.

Here let us show some results and make some conclusions. Six meter length condenser with 20 pipes in total is enough to cool the unit with CO_2 as a working fluid. Total condenser area is 25 m^2. The cold side temperature was chosen as 15°C. Increasing the cooling temperature increase the condenser area.

Fan work is defined by the following expression:

$$\dot{W}_{fan} = \frac{V_{air} A_{cond.} \Delta P_{cond.}}{\eta_{fan}} \tag{2.6}$$

Combining Eqn. (2.2), (2.3), (2.4), (2.5), and (2.6) one can derive the relationship between the rejected heat rate and fan power requirement.

$$\dot{Q}_{Rej.} = \left(\frac{1}{\frac{1}{h_{wf}} + \frac{1}{h_{air}}}\right)\left(\frac{L_{tubes}\pi D_{tubes}\eta_{cond.}}{\dot{m}_{air}\Delta P_{cond.}}\right)\Delta T_{lm.cond}\dot{W}_{fan} \qquad (2.7)$$

The first term in brackets of the equation 2.7 is responsible for heat transfer between *w.f.* and air. It is a function of air and *w.f.* flow rate and fluids properties and cannot be found directly. The second term defines the size of the condenser and kinematic values of air flow. The third term defines the temperature factor of hot and cold sides of the condenser. As soon as the condenser's geometric parameters are defined as well as operating conditions, all three terms would be a constant values, and with changing $\left(\dot{Q}_{Rej.}\right)$ one can calculate $\left(\dot{W}_{fan}\right)$.

2.2.3 Brine Pump

A brine pump assembly includes an electric motor, a multistage pump, safety valves, and tubing. Coordinated operation of all parts in the pump system is the main key of efficient and longtime duty. Thus, there are some of requirements for choosing correct parts. For example, a pump flow rate fluctuations should be less than 10%. Instability greater than 40 % in revolution per minutes for some may cause cavitational, harmonical or vibrational problems. Pump assembly can reach up to 72 ft (Coltharp, 1984) and can be damaged during installation into the horizontal pipe from vertical well. Build up radius cannot exceed 20 degrees per 100ft for the 9 5/8 inch diameter casing string and pumping set is not going to be installed into the bending radius (Bassett L., 2010).

Figure 2.6 shows the general pressure distribution scheme. Here the brine pump creates suction pressure below the reservoir pressure in the production side (drain pressure), and higher than reservoir pressure in the injection side. For this analysis it is assumed that the drawdown is equal to the excessive pressure rise and the brine pump head is the sum of the drain and injection pressures. The choice of pump selection is strongly tied with the hydraulic head required to drive brine from the production to the injection sides, and overcome all pressure losses in the brine loop.

Additionally to that the circular pipe between producer and injector is working as an insulator. So, frictional pressure drop ($\Delta P_{ins.}$) should be added to the pump head pressure.

$$P_{br.pump} = \Delta P_{res.prod.} + \Delta P_{\substack{prod.\\compl.}} + \Delta P_{ins.} + \Delta P_{\substack{inj.\\compl.}} + \Delta P_{res.inj} \tag{2.8}$$

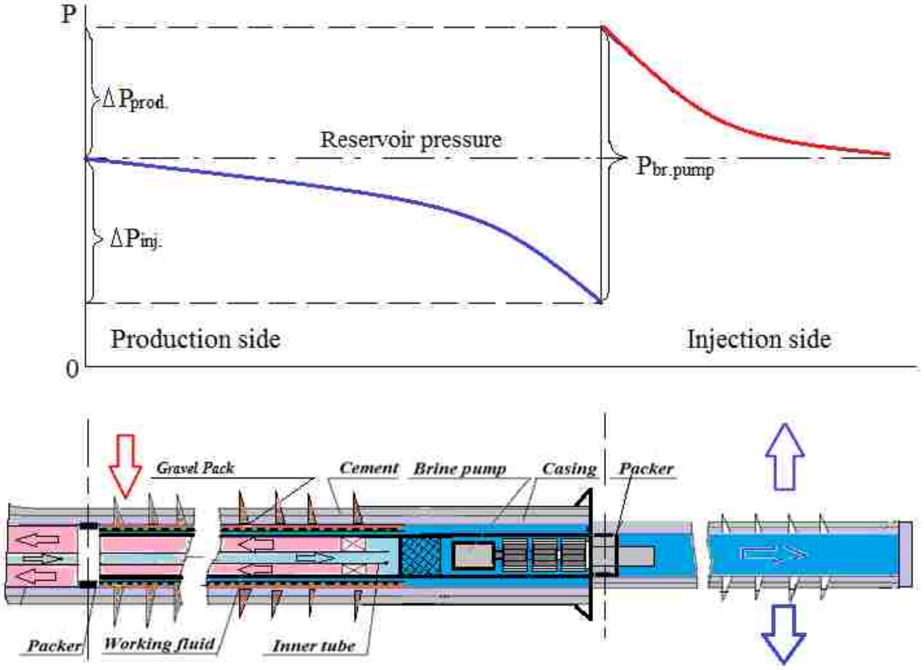

Figure 2.6: Pump placement in the horizontal offset.

2.2.4 Downhole Heat Exchanger

Various design ideas for the DHEs were proposed recently. In general, they can be divided into three main groups by interaction with reservoir rock/fluid: *conduction*, *natural convection, and forced convection* types. The first type is utilized in the condenser cooling schemes with shallow wells. The conductive heat transfer occurs from the vertical well to the reservoir (Figure 2.7 right). Electric power production for a long-term operation is commercially not feasible due to slow heat exchange process (Nalla et al., 2004).

Wang et al. (2009) considered natural convection type for a thermosiphon scheme (Figure. 2.7 left). The design consists of a vertical coaxial heat exchanger with working fluid moving through the inner tubing. At the same time, hot brine flows through the perforations into the outer annulus and discharges back to the reservoir driving by the density difference due to cooling.

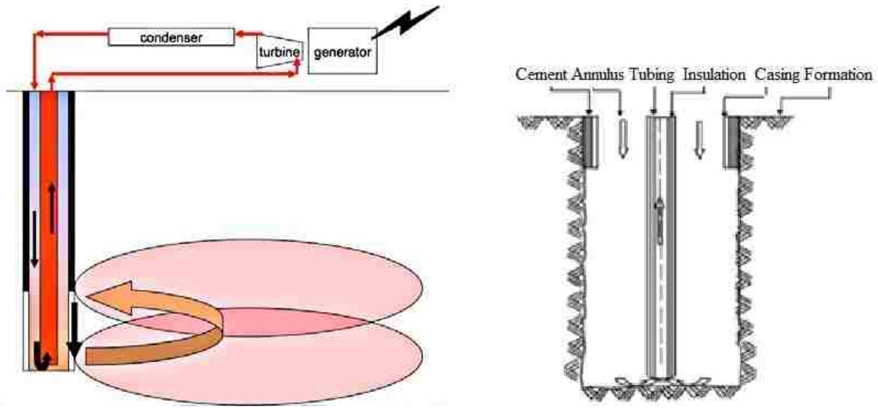

Figure 2.7: Reservoir and heat exchanger interaction schemes
(after Nalla 2004 and Wang et al. 2009).

The temperature distribution along the well is governed by geothermal gradient. The heat transfer occurs along the well, however, the hottest place is located on the bottom. To increase the efficiency the horizontal orientation of the DHE is more preferable. It enhances the contact area with a hot formation and therefore, the net power of the cycle (Feng, et al., 2015). Plaksina et al. (2011) proposed mono-bore scheme for geothermal heat recovery. Instead of using traditional scheme of separate injection and production wells, she combined both into one coaxial pipe. The design encloses the DHE that pumps geo-fluid through itself. Brine enters the DHE heats the working fluid and leaves back into the reservoir at the other end of the pipe.

The third type implies forced convection between DHE and a formation fluid. The DHE was assumed to be installed at the horizontal well drilled in geo-pressured reservoir. The pumping equipment controls brine circulation at the optimal rate. This allows managing the heat exchange process and significantly increasing the amount of energy extracted from the reservoir. Feng (2012) proposed a scheme that allows producing 225 kW of energy using binary Organic Rankine cycle (ORC) with n-Butane as a working fluid. The flow direction of *w.f.* and brine was chosen in counter flow direction due receiving higher temperature at the outlet (Incopera, 2006). The rest of the ORC sections were expected to run at the surface facility.

2.3 System Constraints

In geothermal projects the net power produced from the reservoir is defined by the temperatures of the *hot thermal source* and *cold sink*. Then the PC choice is based on hot and cold side temperature boundaries, pressures, and working fluid selection. Mostly, the ORC type with industry available refrigerants or hydrocarbons is taken into account. In our case the working fluid undergoes hydrostatically pressurizing to values higher than critical pressure. This condition adds some restrictions to the *w.f.* choice. Not every fluid may turn to the vapor form while travelling upward from the DHE depth. Additionally, the binary fluid should satisfy calculated operating parameters and criteria of toxicity and environmental safety.

Another parameter is *reservoir depth*. The traditional power plant analysis does not include hydrostatic and frictional pressure losses because the facility is placed at the surface and its parts are located close to each other. Here the *w.f.* is pumped into the reservoir depth, where the refrigerant becomes highly pressured. Thus, the *stability of the working fluid* becomes another constraint. The working fluid should be chosen from the single component type candidates.

The deep well application would require high amount of the refrigerant needed for the system. This would increase the installation costs unless cheap working fluid is used. Carbon dioxide is abundant and cheap. Several ongoing projects are dedicated to solve the problem of CO_2 sequestration. Using CO_2 in this project would have some positive impact on storing carbon dioxide in the well.

The reservoir pressure at the target depth tends to collapse the well. Pressure inside the DHE is serving against the reservoir to protect the heat exchanger from destruction. Hence, the *w.f.* should provide high pressure at the bottom of the well.

While it is difficult to maintain a supercritical stage at the surface facility, due to high pressure and temperature conditions, in this project pumping the *w.f.* to the target depth makes it reasonable. Supercritical stages are preferable to work with due to ability of receiving higher power production and efficiency. Additionally, the fluid properties (thermal conductivity, specific heat) increases with pressure as was mentioned before.

The heat transfer area of DHE is an important parameter. It is constrained by horizontal offset's *casing diameter* from the one side, and *length of exchanger* from the other. The casing diameter defines the DHE diameter size. The drill bit diameter is reduced gradually with depth while drilling a well. So, the DHE location will have small diameter in advance. In this project the 9 5/8 inch well is proposed. Further reduction of the diameter will increase the frictional losses and higher diameter size is impractical from a drilling operation standpoint. The length of the horizontal offset is defined by the heat exchange process, working fluid and brine flow rates, and frictional losses.

The *working fluid pump* defines the flow rate in the working fluid loop. A higher flow rate value is better for maximizing power production, however, this parameter is closely connected with brine flow rate. So, the brine and *w.f.* flow rates as well as DHE geometry are optimized in order to obtain both: hot working fluid entering the turbine stage and a maximum possible flow rate.

The geo-fluid *pump assembly* is responsible for the brine circulation and bounded by keeping necessary brine flow rate for the heat exchange process. Power requirement is to overcome all pressure losses in the injection, production sides, and reservoir itself. At the same time, pump work should not take a significant portion of the produced electric energy.

The turbine location is better to place close to the wellhead. If it is between the turbine exit and the condenser there is a long vertical flow distance of *w.f.* and an extra pressure drop is created, and an additional compressor would be needed to operate the system.

The *working fluid* circulation loop may have *phase change* from liquid to vapor and the prime interest is to have this process only at the condenser stage. From the other side, it is better to have *w.f.* circulation without any phase change in the condenser, or having operating conditions above the critical point. In this case no additional compressor is needed to operate the cycle.

The condenser has a constant *surface area*, but the amount of heat to be rejected varies with ambient air temperature fluctuations. It is necessary to have enough surface area and pinch point temperature difference to reject heat at the surface facility.

An air cooled condenser is proposed to cool the working fluid and complete the phase change back to the liquid stage. The seasonal variations of ambient air temperature have some impact on power production. For numerical analysis a yearly averaged value is assumed.

CHAPTER 3: SIMPLIFIED MATHEMATICAL MODEL

"Once we accept our limits, we go beyond them."
Albert Einstein

The purpose of this chapter is to introduce subsystems of the power unit, and derive an equation explaining the energy flow from the reservoir to the ambient air. Dimensionless analysis helps reduce the number of variables and connect subsystems with different scales. The chapter suggests several conclusions about the system application.

3.1 System Modelling

To simplify the design analysis the unit is divided into three subsystems: Heat Extraction Subsystem, which includes a reservoir, a brine ESP and a horizontal well; Power Generation Subsystem with Power Cycle (PC) and DHE; and Heat Rejection Subsystem that includes a condenser part on the surface (Figure 3.1).

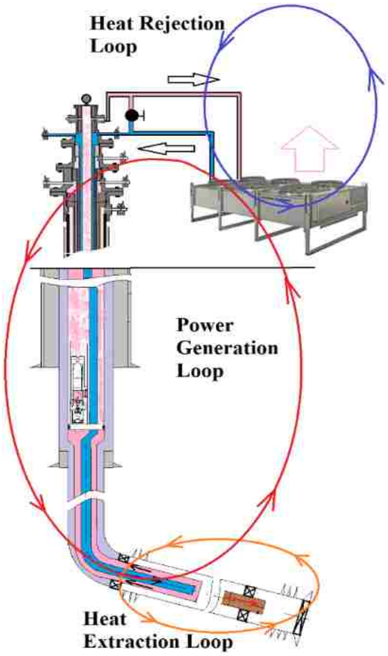

Figure 3.1: Subsystems of the power unit.

Let us discuss the energy flow in the system starting from the reservoir as a heat source and finishing by ambient environment as a cold sink. Figure 3.2 illustrates energy flow in the system. The red and grey arrows represent the energy flow from the reservoir to the ambient and energy losses respectively. The reservoir plays a role of a virtual battery, whose energy is extracted by the DHE. The reservoir recharge is coming from the hot surroundings and the brine pump work is needed to create a circulation of a geo-fluid inside the reservoir.

The extracted energy is transferred to the PC where some portion is discharged to the ambient air through the condenser, and some is turned to mechanical rotation work in the turbine stage and later to the electric power in the generator. This gross power is distributed among the w.f. and brine pumps, and a condenser fan. The rest is net power, which one would like to have as much as possible. At each energy transfer stage there are energy losses from the system due to entropy generation (Moran and Shapiro, 2010).

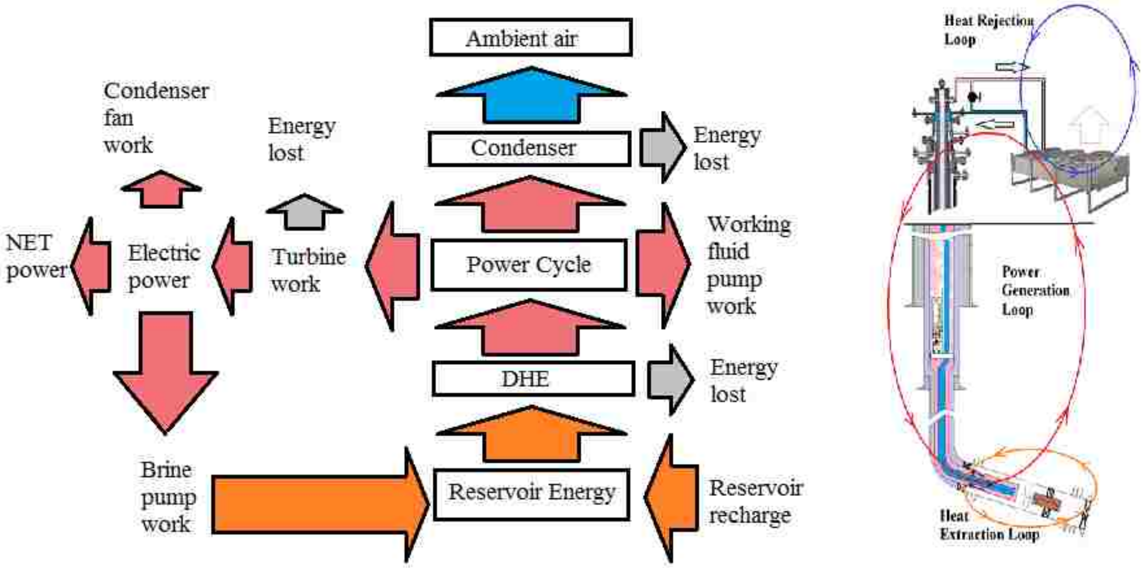

Figure 3.2: Energy flow chart.

To better understand system behavior let us introduce a mathematical formulation of the system as a combination of equations based on energy balance. According to the energy conservation law the control volume energy change is equal to the energy flow in and out and some stored energy inside:

$$\begin{pmatrix} Change\ in \\ CV \\ energy \end{pmatrix} = \begin{pmatrix} Energy \\ rate\ in \end{pmatrix} - \begin{pmatrix} Energy \\ rate\ out \end{pmatrix} + \begin{pmatrix} Energy \\ rate \\ stored \end{pmatrix} \tag{3.1}$$

This principle is used at any subsystem's equation derivation that is introduced below.

3.1.1 Heat Extraction Subsystem (HES)

Let us assume no stored and generated energy is in the HES. Then, the rate of reservoir energy change per unit volume of the whole reservoir is triggered by the heat extraction rate in the DHE, and reservoir recharge mechanism associated by heat flow from the hot surroundings:

$$\begin{pmatrix} Change\ in \\ Reservoir \\ energy \end{pmatrix} = \begin{pmatrix} Energy \\ rate \\ recharge \end{pmatrix} - \begin{pmatrix} Energy \\ rate\ out \\ in\ DHE \end{pmatrix} \tag{3.2}$$

Assumptions:

- Radiative effects, viscous dissipation and work done by pressure changes are negligible;
- Isotropic medium in the reservoir;
- Steady-state energy extraction in the DHE, and PC.

Then for solid (rock) and fluid (brine) phases presented in the elementary volume of the reservoir medium one can write an energy balance equation as shown in the Eqn. (3.3) and (3.4) respectively:

$$(1-\phi)\rho_{rock}\, Cp_{rock}\frac{\partial T_{rock}}{\partial t} = (1-\phi)\nabla\cdot(k_{rock}\nabla T_{rock}) + h(T_{br.} - T_{rock}) - (1-\phi)\dot{Q}'''_{rock} \tag{3.3}$$

$$\phi\rho_{br.}Cp_{br.}\frac{\partial T_{br.}}{\partial t} + \rho_{br.}Cp_{br.}u\cdot\nabla T_{br.} = \phi\nabla\cdot(k_{br.}\nabla T_{br.}) + h(T_{br.} - T_{rock}) - \phi\dot{Q}'''_{br.} \tag{3.4}$$

where ϕ is reservoir porosity, Cp is specific heat, k is thermal conductivity, $\dot{Q}'''$ heat extracted per unit volume, and h is heat transfer coefficient.

Additional assumption of local thermal equilibrium between rock and reservoir brine gives us equal temperatures: $T_{br.} = T_{rock}$. Here we accept that heat conduction in the solid and fluid phases takes place in parallel so that no net heat transfer occurs from one phase to the other (Nield and Bejan, 1998). Combining both equations into one will have:

$$\rho_{bulk}\, Cp_{bulk.} \frac{\partial T_R}{\partial t} = -\rho_{br.} Cp_{br.} u \cdot \nabla T_R + \lambda \nabla^2 T_R - \dot{Q}\,'''_{DHE} \tag{3.5}$$

where λ is overall thermal conductivity:

$$\lambda = (1-\phi)\nabla \cdot (k_{rock}) + \phi k_{br.} \tag{3.6}$$

and $\rho_{bulk}\, C_{pbulk.}$ is found from:

$$\rho_{bulk}\, Cp_{bulk.} = (1-\phi)(\rho_{rock}\, Cp_{rock}) + \phi \rho_{br.} Cp_{br.} \tag{3.7}$$

Heat extracted from the reservoir per unit volume:

$$\dot{Q}\,'''_{DHE} = \frac{(\dot{Q})_{DHE}}{V_R} = (1-\phi)\left(\dot{Q}'''_{rock}\right) + \phi \dot{Q}'''_{br.} \tag{3.8}$$

Heat extracted by the heat exchanger $(\dot{Q})_{DHE}$ is assumed with no fouling take place in the DHE and constant pump work at steady state conditions:

$$(\dot{Q})_{DHE} = \dot{m}_{br.}(h_{in} - h_{out})_{DHE} = \dot{m}_{br.} Cp_{br.}(T_R - T_{br.cold})_{DHE} \tag{3.9}$$

Brine flow in the reservoir is initiated by pressure difference between the production and injection regions and can be approximated with Darcy flow equation:

$$u = -\frac{K}{\mu}(\nabla P - \rho_{br.} g) \tag{3.10}$$

Let us rearrange the Eqn. (3.2) as:

$$\frac{\partial T_R}{\partial t} = -\frac{\rho_{br.} Cp_{br.}}{\rho_{bulk}\, Cp_{bulk.}}\left(-\frac{K}{\mu}(\nabla P - \rho_{br.} g)\right) \cdot \nabla T_R + \frac{\lambda}{\rho_{bulk}\, C_{pbulk.}} \nabla^2 T_R - \frac{\rho_{br.} C_{pbr.} q_{br.} (T_R - T_{br.cold})_{DHE}}{\rho_{bulk}\, C_{pbulk.} V_R} \tag{3.11}$$

where T_R is a reservoir temperature.

Introducing k_M as a thermal diffusivity, and M as a dimensionless constant:

$$k_M = \frac{\lambda}{\rho_{bulk}\, C_{pbulk.}} \tag{3.12}$$

$$M = \frac{\rho_{bulk}\, C_{pbulk.}}{\rho_{br.} C_{pbr.}} \tag{3.13}$$

The final equation is:

$$\frac{\partial T_R}{\partial t} = \frac{1}{M}\left(\frac{K}{\mu}(\nabla P - \rho_{br.} g)\right) \cdot \nabla T_R + k_M \nabla^2 T - \frac{q_{br.}(T_R - T_{br.cold})_{DHE}}{M V_R} \tag{3.14}$$

3.1.2 Power Generation Subsystem

Heat absorbed by the DHE is utilized by the Power Cycle and spent on turbine work, heat rejection, pumps feed power, and losses. The balance energy equation is:

$$\left(\frac{dE}{dt}\right)_{PC} = (\dot{Q})_{DHE} - (\dot{W})_{Turb.} - (\dot{Q})_{HR} - \left(\frac{dE}{dt}\right)_{losses} - (\dot{W})_{\substack{w.f.\\ pump.}} - (\dot{W})_{\substack{br.\\ pump.}} = 0 \tag{3.15}$$

The rate of change in PC energy is equal to zero, so one can assume a steady state regime.

$$(\dot{Q})_{DHE} = (\dot{W})_{Turb.} + (\dot{Q})_{HR} + (\dot{W})_{w.f.pump.} + (\dot{W})_{br.pump.} + \left(\frac{dE}{dt}\right)_{losses} \tag{3.16}$$

To define the net power some corrections are used including turbine, generator and mechanical gearbox efficiencies:

$$(\dot{W})_{Turb.} = \frac{(\dot{W})_{NET.}}{\eta_{turb.}\eta_{gen.}\eta_{mech.}} = \frac{(\dot{W})_{NET.}}{\eta_{electr.}} \tag{3.17}$$

The energy lost from the PC $\left(\frac{dE}{dt}\right)_{losses}$ is thermal energy that is absorbed by the subsurface formation from the hot working fluid. The entire tubing, where the hot fluid is flowing from the DHE to the turbine inlet, is assumed insulated in this project, thus, the heat losses are presumed negligible. However, the hot *w.f.* pumped toward the surface is expanding at constant temperature. This causes *w.f.* enthalpy growth (more detailed explanation is in Chapter 4) and, therefore, should be included into the equation:

$$(\dot{Q})_{DHE} = \frac{(\dot{W})_{NET.}}{\eta_{electr.}} + (\dot{Q})_{HR} + (\dot{W})_{w.f.pump.} + (\dot{W})_{br.pump.} + \dot{m}_{wf.}(h_{in} - h_{out})_{vert.} \quad (3.18)$$

- Brine pump work

Brine pump power requirement should be subtracted from the PC energy rate.

$$\dot{W}_{pump(br).} = \frac{P_{br.pump}\dot{m}_{br}}{\rho_{br}} \quad (3.19)$$

where $P_{br.pump}$ was defined previously as:

$$P_{br.pump} = \Delta P_{res.} + \Delta P_{\substack{prod.\\compl.}} + \Delta P_{ins.} + \Delta P_{\substack{inj.\\compl.}} \quad (2.8)$$

The frictional pressure losses inside the well have two terms: flow in the circular section and flow through the DHE. The friction coefficient is not the same for flow through the circular pipe with outflow through the perforations and classical pipe flow. However, for simplicity purposes let us assume no difference. Then:

$$\Delta P_{ins.} = \frac{f\dot{m}_{br}^{\ 2}(L_{ins.} + L_{inj.})}{2D_{horiz.}\rho_{br}A_{c(w)}^{\ 2}} + \frac{f_{DHE.}\dot{m}_{br}^{\ 2}L_{DHE.}}{2D_{DHE.}\rho_{br}A_{c(DHE)}^{\ 2}} \quad (3.20)$$

where $L_{ins.}$ is a separation length between injection and production sides; $D_{horiz.}$ is a horizontal well diameter without DHE inside; $D_{DHE.}$ is the heat exchanger's hydraulic diameter.

The $\Delta P_{res.}$ term is defined by Darcy law for simplicity purposes (More detailed discussion about the flow inside the reservoir is continues in the Chapter 6).

Eventually, the Equation. (3.19) includes well inclination term as well:

$$\dot{W}_{pump(br).} = \frac{\dot{m}_{br}}{\rho_{br}}\Bigg(\Delta P_{res.} + \Delta P_{\substack{prod.\\compl.}} + \Delta P_{\substack{inj.\\compl.}} + \frac{f\dot{m}_{br}^{\ 2}(L_{ins.} + L_{inj.})}{2D_{horiz.}\rho_{br}A_{c(w)}^{\ 2}} + \frac{f\dot{m}_{br}^{\ 2}L_{DHE.}}{2D_{DHE.}\rho_{br}A_{c(DHE)}^{\ 2}}$$

$$- \rho_{br.}g(L_{ins.} + L_{inj.} + L_{prod.})\cos\theta\Bigg) \quad (3.21)$$

- The working fluid pump work

Pump work for working fluid is obtained from the analogous formulation to (3.19):

$$\dot{W}_{pump(wf).} = \frac{\Delta P_{wf.} \dot{m}_{wf}}{\rho_{wf.cold}} \tag{3.22}$$

The density $\rho_{wf.cold}$ in the equation. 3.22 is marked as *cold* because the w.f. pump is installed at the cold stream. Neglecting pressure drop in the condenser and inside the DHE due to their short length compared to the vertical well the $\Delta P_{wf.}$ term has two components:

$$\Delta P_{wf.} = \Delta P_{gravity} + \Delta P_{frict.} \tag{3.23}$$

The working fluid is travelling up and down through the tubing and the annulus of the vertical well, which length is *Z* measured from the surface to the DHE. The pressure difference in the hydrostatic column is defined by thermosiphon driving force of density difference $\Delta\rho_{wf}$ between cold and hot streams.

$$\Delta P_{gravity} = (\rho_{wf.cold} - \rho_{wf.hot})gZ = \Delta\rho_{wf} gZ \tag{3.24}$$

The frictional pressure drop $\Delta P_{frict.}$ is a sum of frictional losses in the cold and hot sides of the subsystem. Approximating diameter as an average hydraulic diameter D_h ,which is constant for both sides one can write the expression for $\Delta P_{frict.}$ as shown in the Eqn. (3.25):

$$\Delta P_{frict.} = \left(\frac{f \rho_{wf.cold} V^2{}_{cold} Z}{2D_h}\right)_{down} + \left(\frac{f \rho_{wf.hot} V^2{}_{hot} Z}{2D_h}\right)_{up} \tag{3.25}$$

Then the w.f. pump work is:

$$\dot{W}_{pump(wf).} = \frac{\dot{m}_{wf}{}^3 f Z}{2D_h A^2 \rho_{wf.cold}} \left(\frac{\rho_{wf.cold} + \rho_{wf.hot}}{\rho_{wf.cold}\rho_{wf.hot}}\right) - \frac{\Delta\rho_{wf} gZ \dot{m}_{wf}}{\rho_{wf.cold}} \tag{3.26}$$

The second term in equation. 3.26 reduces pump load due to thermosiphon effect, when the colder fluid displaces hot fluid and create circulation helping to the *w.f.* pump. Finally, heat rate gained by the DHE is expressed by the following equation:

$$\left(\dot{Q}\right)_{DHE}=\frac{\left(\dot{W}\right)_{NET.}}{\eta_{electr.}}+\left(\dot{Q}\right)_{HR}+\frac{\dot{m}_{wf}{}^{3}fZ}{2D_hA^2\rho_{wf.cold}}\left(\frac{\rho_{wf.cold}+\rho_{wf.hot}}{\rho_{wf.cold}\rho_{wf.hot}}\right)-\frac{\Delta\rho_{wf}gZ\dot{m}_{wf}}{\rho_{wf.cold}}$$

$$+\frac{\dot{m}_{br}}{\rho_{br}}\left(\Delta P_{res.}+\Delta P_{prod.}+\Delta P_{inj.}+\frac{f\dot{m}_{br}{}^{2}\left(L_{ins.}+L_{inj.}\right)}{2D_{horis.}\rho_{br}A_{c(w)}{}^{2}}+\frac{f\dot{m}_{br}{}^{2}L_{DHE.}}{2D_{DHE.}\rho_{br}A_{c(DHE)}{}^{2}}\right.$$

$$\left.-\rho_{br.}g\left(L_{ins.}+L_{inj.}+L_{prod.}\right)\cos\alpha\right)+\dot{m}_{wf}\left(h_{DHE\,out}-h_{turb.in}\right)\qquad(3.27)$$

3.1.3 Heat Rejection Subsystem

Let us assume negligible heat losses from the condenser to the ambient air. This is true with assumption of predominant convective type of heat exchanger powered by fan. Because the condenser may have two-phase condensation region it is more convenient to formulate energy equation in terms of flow rate and temperature of ambient air:

$$\left(\dot{Q}\right)_{cond.}=\dot{m}_{air}Cp_{air}\left(T_{air.in}-T_{air.out}\right)\qquad(3.28)$$

The ambient air usually is assumed as a constant term and equal to the yearly averaged temperature. However, the net power production depends on cold sink temperature variations during day/night periods and seasonal changes. In general, the following idealized expression is mimicking the process:

$$T_{air.in}=T_{avg.}^{annual}+\frac{T_{day}-T_{night}}{2}\sin(\omega_1t)+\frac{T_{summer}-T_{winter}}{2}\sin(\omega_2t)\qquad(3.29)$$

where ω_1 and ω_2 are daily and seasonal periods [1/sec].

$$\left(\dot{Q}\right)_{HR}=\dot{m}_{air}Cp_{air}(T_{avg.}^{annual}+\frac{T_{day}-T_{night}}{2}\sin(\omega_1t)+\frac{T_{summer}-T_{winter}}{2}\sin(\omega_2t)$$

$$-T_{air.out})\ +\left(\dot{W}\right)_{fan}\qquad(3.30)$$

Finally, the system of equations describing the system is shown by the following three expressions:

$$\frac{\partial T_R}{\partial t}=\frac{1}{M}\left(\frac{K}{\mu}\left(\nabla P-\rho_{br.}g\right)\right)\cdot\frac{\partial T_R}{\partial x}+k_M\nabla^2T-\frac{\left(\dot{Q}\right)_{DHE}}{V_R\rho_{bulk}\,C_{pbulk.}}$$

$$
\begin{aligned}
\left(\dot{Q}\right)_{DHE} = {} & \frac{\left(\dot{W}\right)_{NET.}}{\eta_{electr.}} + \frac{\dot{m}_{wf}{}^{3} f Z}{2 D_h A^2 \rho_{wf.cold}} \left(\frac{\rho_{wf.cold} + \rho_{wf.hot}}{\rho_{wf.cold} \rho_{wf.hot}} \right) - \frac{\Delta \rho_{wf} g Z \dot{m}_{wf}}{\rho_{wf.cold}} \\
& + \frac{\dot{m}_{br}}{\rho_{br}} \left(\Delta P_{res.} + \Delta P_{prod.} + \Delta P_{inj.} + \frac{f \dot{m}_{br}{}^{2} \left(L_{ins.} + L_{inj.}\right)}{2 D_{horis.} \rho_{br} A_{c(w)}{}^{2}} + \frac{f \dot{m}_{br}{}^{2} L_{DHE.}}{2 D_{DHE.} \rho_{br} A_{c(DHE)}{}^{2}} \right. \\
& \left. - \rho_{br.} g \left(L_{ins.} + L_{inj.} + L_{prod.} \right) \cos \alpha \right) + \dot{m}_{wf} \left(h_{DHE\,out} - h_{turb.in} \right) + \left(\dot{Q}\right)_{HR}
\end{aligned}
$$

$$
\begin{aligned}
\left(\dot{Q}\right)_{HR} = {} & \dot{m}_{air} Cp_{air} \Big(T_{avg.}^{annual} + \frac{T_{day} - T_{night}}{2} \sin(\omega_1 t) + \frac{T_{summer} - T_{winter}}{2} \sin(\omega_2 t) \\
& - T_{air.out} \Big) + \left(\dot{W}\right)_{fan} \qquad (3.31)
\end{aligned}
$$

3.2 Dimensionless form

The equation 3.31 has forty five variables. To reduce the number of variables and simplify the equation let us present the dimensionless form formulation. First, let us introduce a dimensionless time as was discussed by Ansari (2016):

$$t_D = \frac{\rho_{br.} C_{pbr.}}{\rho_{bulk}\, C_{pbulk}} \frac{q_{br.} t}{HWL} = \frac{q_{br.} t}{V_R M} \qquad (3.32)$$

where $q_{br.}$ is a volumetric brine flow rate.

The relation between time and dimensionless time is:

$$dt = \frac{M V_R}{q_{br.}} dt_D \qquad (3.33)$$

Dimensionless temperature is expressed in the following equation:

$$T_{R(D)} = \frac{T_R}{T_R{}^{*}} \qquad (3.34)$$

where $T_R{}^{*}$ is initial reservoir temperature before cooling process.

$$dT_R = T_R{}^{*} dT_{R(D)} \qquad (3.35)$$

Then:

$$\frac{\partial T_R}{\partial t} = \frac{q_{br.} T_R{}^{*} dT_{R(D)}}{MV_R dt_D} \tag{3.36}$$

The dimensionless distance (dx_D) from the injector to the producer:

$$dx_D = \frac{x}{L_{ins.}} \tag{3.37}$$

where $L_{ins.}$ is a distance between injection and production sides of the well.

Combining all equations of the system (3.31) in into one and converting to the dimensionless form will have the expression for the reservoir temperature change with time.

$$\begin{aligned}
\frac{\partial T_{R(D)}}{dt_D} = {} & \frac{\rho_{br.} V_R \left(\frac{K}{\mu}(\nabla P - \rho_{br.} g)\right)}{\dot{m}_{br.}(\,L_{ins.})} \frac{\partial T_{R(D)}}{dx_D} + \frac{\rho_{br.} M V_R k_M}{\dot{m}_{br.}(\,L_{ins.})^2} \frac{\partial^2 T_{R(D)}}{dx_D{}^2} - \frac{\rho_{br.} M \big(\dot{W}\big)_{NET.}}{\rho_{bulk.} \dot{m}_{br.} C_{pbulk.} T_R{}^{*} \eta_{elect.}} \\
& - \frac{\rho_{br.} \dot{m}_{air} C_{p\,air} M}{\rho_{bulk.} \dot{m}_{br.} C_{pbulk.} T_R{}^{*}} \left[T_{avg.}^{annual} + \frac{T_{day} + T_{night}}{2} \sin(\omega_1 t) \right. \\
& \left. + \frac{T_{summer} + T_{winter}}{2} \sin(\omega_2 t) - T_{air.out} \right] - \frac{\rho_{br.} M \big(\dot{W}\big)_{fan}}{\rho_{bulk.} \dot{m}_{br.} C_{pbulk.} T_R{}^{*}} \\
& - \frac{\rho_{br.} M \dot{m}_{wf}}{\dot{m}_{br.} \rho_{bulk.} C_{pbulk.} T_R{}^{*}} \frac{V_{wf}{}^2 f Z}{D_h} \left(\frac{\rho_{wf.cold} + \rho_{wf.hot}}{2 \rho_{wf.hot}} \right) \\
& + \frac{\rho_{br.} M \dot{m}_{wf} g Z \Delta\rho_{wf}}{\dot{m}_{br.} \rho_{bulk.} C_{pbulk.} T_R{}^{*} \rho_{wf.cold}} \\
& - \frac{M}{C_{pbulk.} T_R{}^{*}} \frac{\dot{m}_{br.}}{\rho_{br} \rho_{bulk}} \big(\Delta P_{res.} + \Delta P_{prod.} + \Delta P_{inj.} \big) \\
& - \frac{M \rho_{br.} f V_{horiz.}{}^2 \big(L_{ins.} + L_{inj.} \big)}{2 D_{horiz.} \rho_{bulk.} C_{pbulk.} T_R{}^{*}} - \frac{f V_{DHE}{}^2 L_{DHE.} \rho_{br.} M}{\rho_{bulk.} C_{pbulk.} T_R{}^{*} 2 D_{DHE.}} \\
& - \frac{\rho_{br.} M g \big(\, L_{ins.} + L_{inj.} + L_{prod.} \big) \cos\alpha}{\rho_{bulk.} C_{pbulk.} T_R{}^{*}} - \frac{\rho_{br.} M \dot{m}_{wf} \big(h_{DHE\,out} - h_{turb.in} \big)}{\rho_{bulk.} C_{pbulk.} T_R{}^{*} \dot{m}_{br.}}
\end{aligned} \tag{3.38}$$

In the dimensionless form the equation 3.38 has only twenty two variables.

$$\frac{dT_{R(D)}}{dt_D} - \pi_1 \frac{\partial T_{R(D)}}{dx_D} - \pi_2\pi_3 \frac{\partial^2 T_{R(D)}}{{dx_D}^2} + \pi_2\pi_4\pi_5 + \pi_2\pi_5\pi_6\pi_7 + \pi_2\pi_5\pi_8 + \pi_2\pi_5\pi_9\pi_{10}\pi_{11} - \pi_2\pi_5\pi_{10}\pi_{12}\pi_{13} + \pi_2\pi_{14} + \pi_2\pi_5\pi_{15}\pi_{16} + \pi_2\pi_5\pi_{17}\pi_{18} + \pi_2\pi_5\pi_{19} + \pi_2\pi_5\pi_{10}\pi_{20} = 0 \tag{3.39}$$

The equation 3.39 cannot be solved analytically due to having highly nonlinear terms and dependent variables. The dimensionless numbers are presented in the Table 3.1.

Table 3.1: Dimensionless numbers derived from equation (3.39)

Dimensionless number	Formula	Interpretation
$\boldsymbol{\pi_1}$	$\dfrac{V_R\left(\frac{K}{\mu}(\nabla P - \rho_{br.}g)\right)}{q_{br.}(L_{ins.})}$	Ratio of brine velocity flow inside the reservoir volume to the flow inside the horizontal well
$\boldsymbol{\pi_2}$	$M = \dfrac{\rho_{bulk}\, C_{pbulk.}}{\rho_{br.}C_{pbr.}}$	Ratio of reservoir bulk to brine thermal capacities. The same dimensionless number was used by (Ansari, 2016)
$\boldsymbol{\pi_3}$	$\dfrac{\rho_{br.}V_R k_M}{\dot{m}_{br.}(L_{ins.})^2}$	Ratio of volumetric thermal diffusivity to the volumetric flow rate
$\boldsymbol{\pi_4}$	$\dfrac{(\dot{W})_{NET.}}{\dot{m}_{br.}C_{pbr.}{T_R}^{*}\eta_{elect.}}$	Dimensionless net power
$\boldsymbol{\pi_5}$	$\dfrac{\rho_{br.}}{\rho_{bulk.}}$	Dimensionless density
$\boldsymbol{\pi_6}$	$\dfrac{\dot{m}_{air}C_{p\,air}}{\dot{m}_{br.}C_{pbulk.}}$	Heat capacity ratio (air to geo- fluid)
$\boldsymbol{\pi_7}$	$\dfrac{1}{{T_R}^{*}}\left(T_{avg.}^{annual} + \dfrac{T_{day}+T_{night}}{2}\sin(\omega_1 t) + \dfrac{T_{summer}+T_{winter}}{2}\sin(\omega_2 t) - T_{air.out}\right)$	Dimensionless ambient temperature
$\boldsymbol{\pi_8}$	$\dfrac{(\dot{W})_{fan}}{\dot{m}_{br.}C_{pbulk.}{T_R}^{*}}$	Ratio of fan consumed energy requirement to the thermal energy of the reservoir

Table 3.1 (continued)

Dimensionless number	Formula	Interpretation
$\boldsymbol{\pi_9}$	$\frac{fV_{w.f.}{}^2 Z}{C_{pbr.} T_R{}^* D_h}$	Ratio of friction energy in the vertical well to the thermal energy
$\boldsymbol{\pi_{10}}$	$\frac{\dot{m}_{wf}}{\dot{m}_{br.}}$	Ratio of w.f. and brine flow rates
$\boldsymbol{\pi_{11}}$	$\frac{\rho_{wf.cold} + \rho_{wf.hot}}{2\rho_{wf.hot}}$	Ratio of average w.f. density of the system to the hot stream density
$\boldsymbol{\pi_{12}}$	$\frac{\Delta\rho_{wf}}{\rho_{wf.cold}}$	Ratio of density change to cold stream density
$\boldsymbol{\pi_{13}}$	$\frac{gZ}{C_{pbr.} T_R{}^*}$	Ratio of gravity to thermal energy
$\boldsymbol{\pi_{14}}$	$\frac{\dot{m}_{br.}(\Delta P_{res.} + \Delta P_{prod.} + \Delta P_{inj.})}{C_{pbulk.} \rho_{br.} \rho_{bulk.} T_R{}^*}$	Ratio of circulation work to the heat transfer energy
$\boldsymbol{\pi_{15}}$	$\frac{L_{ins.} + L_{inj.}}{2D_{hor.}}$	Ratio of horizontal circular section length to its diameter
$\boldsymbol{\pi_{16}}$	$\frac{fV_{horiz.}{}^2}{C_{pbr.} T_R{}^*}$	Ratio of frictional energy in the horizontal well to the thermal energy
$\boldsymbol{\pi_{17}}$	$\frac{L_{DHE}}{D_{DHE}}$	Ratio of DHE length to its diameter
$\boldsymbol{\pi_{18}}$	$\frac{fV_{DHE}{}^2}{C_{pbr.} T_R{}^*}$	Ratio of frictional energy in the DHE to the thermal energy
$\boldsymbol{\pi_{19}}$	$\frac{g(L_{ins.} + L_{inj.} + L_{prod.}) \cos\alpha}{C_{pbr.} T_R{}^*}$	Ratio of gravitational energy in the horizontal well to the heat transfer
$\boldsymbol{\pi_{20}}$	$\frac{(h_{DHE\ out} - h_{turb.in})}{C_{pbr.} T_R{}^*}$	Entropy change in the vertical hot stream to the reservoir thermal energy

The first dimensionless number π_1 can be simplified to the ratio of total reservoir volume to the volume of reservoir fluid flow from the injection to the production sides:

$$\pi_1 = \frac{V_R\left(\frac{K}{\mu}(\nabla P - \rho_{br.}g)\right)}{q_{br.}(\,L_{ins.})} = \frac{V_R}{A_{cr.}L_{ins.}} \tag{3.40}$$

The volume of the reservoir (V_R) compared to the flowing volume ($A_{cr.}L_{ins.}$), should be high enough to provide the reservoir recharge against the cooling process.

The third dimensionless group π_3 in the Table 3.1 again has the reservoir volume.

$$\pi_3 = \frac{\lambda V_R}{\dot{m}_{br.}(\,L_{ins.})^2 Cp_{br.}} \tag{3.41}$$

Figure (3.3) illustrates the point. The producer is separated from the injector by the distance ($L_{ins.}$). The flow can be approximated as a Darcy flow through the cylindrical portion of the reservoir with the volume of ($A_{cr.}L_{ins.}$). If the reservoir volume (V_R) is big enough then the cooling process will take a longer time.

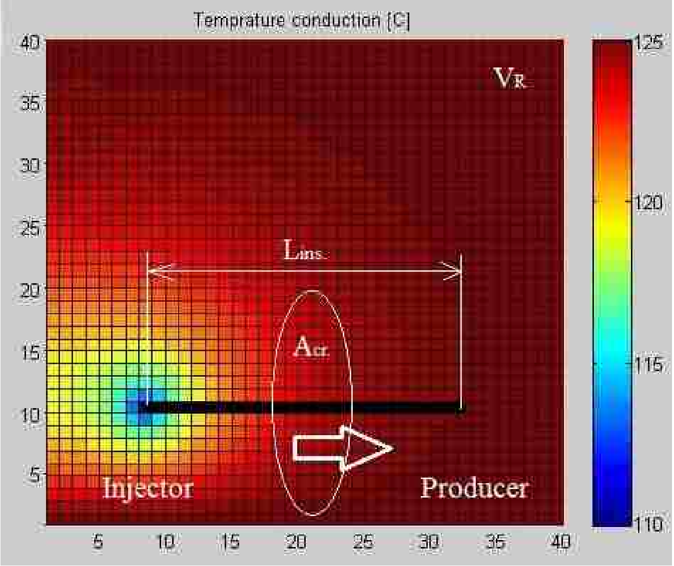

Figure 3.3: Reservoir fluid flow schematic from the injector to the producer.

If one would like to have steady state conditions for the reservoir temperature: $\frac{\partial T_{R(D)}}{dt_D} = 0$, the dimensionless groups in the equation. 3.40 and 3.41 should have the maximum values.

3.3 Net Power Change with Dimensionless Time

Ansari (2016) solved for an equation for the reservoir temperature change with respect to time and presented the results as a set of linear functions with respect to the dimensionless time intervals. More information is in the Figure 3.4.

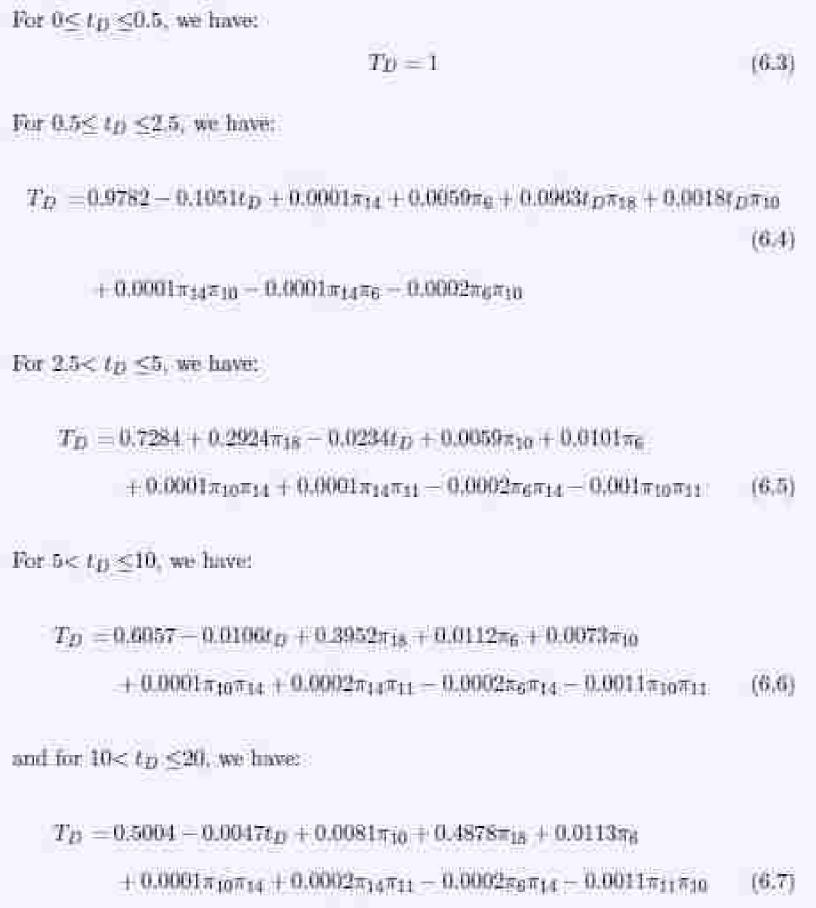

For $0 \leq t_D \leq 0.5$, we have:

$$T_D = 1 \tag{6.3}$$

For $0.5 \leq t_D \leq 2.5$, we have:

$$T_D = 0.9782 - 0.1051 t_D + 0.0001\pi_{14} + 0.0059\pi_6 + 0.0963 t_D \pi_{18} + 0.0018 t_D \pi_{10} + 0.0001\pi_{14}\pi_{10} - 0.0001\pi_{14}\pi_6 - 0.0002\pi_6\pi_{10} \tag{6.4}$$

For $2.5 < t_D \leq 5$, we have:

$$T_D = 0.7284 + 0.2924\pi_{18} - 0.0234 t_D + 0.0059\pi_{10} + 0.0101\pi_6 + 0.0001\pi_{10}\pi_{14} + 0.0001\pi_{14}\pi_{11} - 0.0002\pi_6\pi_{14} - 0.001\pi_{10}\pi_{11} \tag{6.5}$$

For $5 < t_D \leq 10$, we have:

$$T_D = 0.6057 - 0.0106 t_D + 0.2952\pi_{18} + 0.0112\pi_6 + 0.0073\pi_{10} + 0.0001\pi_{10}\pi_{14} + 0.0002\pi_{14}\pi_{11} - 0.0002\pi_6\pi_{14} - 0.0011\pi_{10}\pi_{11} \tag{6.6}$$

and for $10 < t_D \leq 20$, we have:

$$T_D = 0.5004 - 0.0047 t_D + 0.0081\pi_{10} + 0.4878\pi_{18} + 0.0113\pi_6 + 0.0001\pi_{10}\pi_{14} + 0.0002\pi_{14}\pi_{11} - 0.0002\pi_6\pi_{14} - 0.0011\pi_{11}\pi_{10} \tag{6.7}$$

Figure 3.4: Reservoir temperature change in dimensionless form (after Ansari, E., 2016).

In this project the main interest is tracking the net power change. Let us take the derivative of equation 3.39 with respect to time.

$$\frac{d^2T_{R(D)}}{{dt_D}^2} - \pi_1 \frac{\partial^2 T_{R(D)}}{dx_D dt_D} - \pi_2\pi_3 \frac{\partial^3 T_{R(D)}}{{dx_D}^2 dt_D} + \frac{d\pi_4}{dt_D}(\pi_2\pi_4\pi_5) + \frac{d\pi_4}{dt_D}(\pi_2\pi_5\pi_6\pi_7) + \frac{d\pi_4}{dt_D}(\pi_2\pi_5\pi_8)$$
$$+ \frac{d\pi_4}{dt_D}(\pi_2\pi_5\pi_9\pi_{10}\pi_{11}) - \frac{d\pi_4}{dt_D}(\pi_2\pi_5\pi_{10}\pi_{12}\pi_{13}) + \frac{d\pi_4}{dt_D}(\pi_2\pi_{14})$$
$$+ \frac{d\pi_4}{dt_D}(\pi_2\pi_5\pi_{15}\pi_{16}) + \frac{d\pi_4}{dt_D}(\pi_2\pi_5\pi_{17}\pi_{18}) + \frac{d\pi_4}{dt_D}(\pi_2\pi_5\pi_{19})$$
$$+ \frac{d\pi_4}{dt_D}(\pi_2\pi_5\pi_{10}\pi_{20}) = 0 \tag{3.42}$$

The only terms of equation 3.42 that have dependence on dimensionless time are listed in the formula below:

$$\frac{d\pi_4}{dt_D} = \frac{\pi_1}{\pi_2\pi_5} \frac{\partial^2 T_{R(D)}}{dt_D dx_D} + \frac{\pi_3}{\pi_5} \frac{\partial^3 T_{R(D)}}{dt_D {dx_D}^2} - \pi_6 \frac{d\pi_7}{dt_D} \tag{3.43}$$

Note, this is true with the assumptions of no fouling or sand production happening inside the well, and no leakage of w.f. from the system. Both pumps are working at steady-state conditions with constant flow rates.

The equation 3.43 has an essential meaning. The change in net power produced by the geothermal unit is a function of reservoir energy recharge drop due to reservoir cooling process (first two terms in the right hand side) and seasonal ambient air fluctuations with respect to time (the last term in the RHS). Our objective is to have maximum power extracted from the reservoir for the operational life, thus, the primary interest of the project is to stay at $\frac{dT_{R(D)}}{dt_D} = 0$ interval. According to Ansari (2016) the change in reservoir temperature is a first derivative from data in the Figure 3.4 (see Table 3.2). The first time interval ($0 \leq t_D \leq 0.5$) shows no temperature change in produced reservoir brine, meaning that the cold fluid front did not reach the production side.

Analyzing the equation 3.43 one can say that the dimensionless coefficients are the functions of the horizontal well length:

$$\frac{\pi_1}{\pi_2\pi_5} = \frac{C_{pbulk.}V_R}{C_{pbr.}A_{cr.}(\ L_{ins.})} \tag{3.44}$$

$$\frac{\pi_3}{\pi_5} = \frac{V_R\lambda}{\dot{m}_{br.}C_{pbulk.}(\ L_{ins.})^2} \tag{3.45}$$

Thus, increasing the length would help on avoiding the cooled brine entering the production side.

Table 3.2. Time derivatives for dimensionless reservoir temperature

Time interval	Expression
$\boldsymbol{0 \leq t_D \leq 0.5}$	$\frac{dT_{R(D)}}{dt_D} = 0$
$\boldsymbol{0.5 \leq t_D \leq 2.5}$	$\frac{dT_{R(D)}}{dt_D} = -0.1051 + 0.0963\pi_{18} + 0.0018\pi_{10}$ $\pi_{18} = \frac{T_{inj.}}{T_{avg.}}; \pi_{10} = \frac{L_{prod.}}{H}$ (these dimensionless numbers are borrowed from (Ansari, 2016)
$\boldsymbol{2.5 \leq t_D \leq 5}$	$\frac{dT_{R(D)}}{dt_D} = -0.0234$
$\boldsymbol{5 \leq t_D \leq 10}$	$\frac{dT_{R(D)}}{dt_D} = -0.0106$
$\boldsymbol{10 \leq t_D \leq 20}$	$\frac{dT_{R(D)}}{dt_D} = -0.0047$

Understanding that reservoir cooling mechanism is semi-steady state let us take first derivative of reservoir temperature with respect to time. Then one can ignore the reservoir cooling and only the surface temperature fluctuations would affect the net power production.

$$\frac{d\pi_4}{dt_D} = -\pi_6 \frac{d\pi_7}{dt_D} \sim \frac{\partial}{\partial t_D}\left(\frac{T_{avg.}^{annual} + \frac{T_{day} - T_{night}}{2}\sin(\omega_1 t) + \frac{T_{summer} - T_{winter}}{2}\sin(\omega_2 t) - T_{air.out}}{{T_R}^*}\right) \tag{3.46}$$

$$\frac{d\pi_4}{dt_D} \sim \omega_1 \frac{MV_R}{q_{br.}} \frac{T_{day} - T_{night}}{2{T_R}^*} \cos\left(\omega_1 \frac{MV_R}{q_{br.}} t_D\right) + \omega_2 \frac{MV_R}{q_{br.}} \frac{T_{summer} - T_{winter}}{2{T_R}^*} \cos\left(\omega_2 \frac{MV_R}{q_{br.}} t_D\right) \tag{3.47}$$

3.4 Efficiency of the Cycle

Let us introduce the efficiency of the cycle as a ratio of total work done by the cycle to the heat added through the DHE:

$$\eta_{PC} = \frac{\dot{W}_{cycle}}{\dot{Q}_{DHE}} = \frac{\dot{W}_{out} - \dot{W}_{in}}{\dot{Q}_{DHE}} = \frac{\dot{W}_{turb.} - \dot{W}_{wf.pump}}{\dot{Q}_{DHE}} \tag{3.48}$$

$$\dot{W}_{turb.} = \dot{m}_{wf}(h_{in.turb} - h_{out.turb.}) \tag{3.49}$$

The pump work was defined previously in the equation 3.22:

$$\dot{W}_{pump(wf).} = \frac{{\dot{m}_{wf}}^{3} fZ}{2D_h A^2 \rho_{wf.cold}} \left(\frac{\rho_{wf.cold} + \rho_{wf.hot}}{\rho_{wf.cold}\rho_{wf.hot}} \right) - \frac{\Delta\rho_{wf} gZ \dot{m}_{wf}}{\rho_{wf.cold}} \tag{3.22}$$

$$\dot{Q}_{DHE} = \dot{m}_{wf} C_{pwf} \big(T_{wf.hot} - T_{wf.cold.}\big) = \dot{m}_{wf} C_{pwf} T_R(\eta_c) - \dot{m}_{wf} C_{pwf} (\Delta T_{DHE} + \Delta T_{cond.}) \tag{3.50}$$

$$\eta_{PC} = \frac{(h_{in.turb} - h_{out.turb.}) - \dfrac{{\dot{m}_{wf}}^{2} fZ}{2D_h A^2 \rho_{wf.cold}} \left(\dfrac{\rho_{wf.cold} + \rho_{wf.hot}}{\rho_{wf.cold}\rho_{wf.hot}} \right) + \dfrac{\Delta\rho_{wf} gZ}{\rho_{wf.cold}}}{C_{pwf} T_R(\eta_c) - C_{pwf}(\Delta T_{DHE} + \Delta T_{cond.}) + \dot{m}_{wf}(h_{turb.in} - h_{DHE.out.})} \tag{3.51}$$

Now, instead of T_R one can put reservoir temperature reduction to track the PC efficiency drop with operational time.

3.5 Conclusions

Choosing the reservoir for ZMW applications it is recommended picking a heat source with high initial reservoir temperature ${T_R}^*$, large reservoir volume V_R, high thermal conductivity of the rock λ with high porosity ϕ, to design a system with high geo-fluid flow rate $\dot{m}_{br.}$ with sufficient distance between producer and injector, $L_{ins.}$. At the same time, the other terms of the equation (3.39) have to be small in order to get maximum net power production: small fan power consumption $(\dot{W})_{fan}$, negligible pressure drop at the completions $(\Delta P_{prod.} + \Delta P_{inj.})$ and frictional losses inside the well.

CHAPTER 4: THERMODYNAMICS AND WORKING FLUID SELECTION

"I just invent, then wait until man comes around to needing what I've invented."
R. Buckminster Fuller

The purpose of this chapter is to define the power cycle type suitable for the well energy conversion unit design and make a choice of the working fluid. This chapter presents thermodynamic analysis of the cycle for the chosen fluid, and DHE geometry optimization using enthalpy minimization approach. The example of thermodynamic analysis is performed for the reference reservoir data.

4.1 Introduction to Power Cycle

Regardless of the operating PC type, the energy extraction system works between cold and hot sides defined by ambient air and brine surface temperatures as indicated in the Figure 4.1. If the produced geo-fluid is hot water, not steam, the PC modification is needed. If the cycle utilizes organic fluids instead of water, the thermodynamic process is called Organic Rankine Cycle (ORC) (Schuster, 2009). This fluid is typically a refrigerant, which has boiling point lower than that of water.

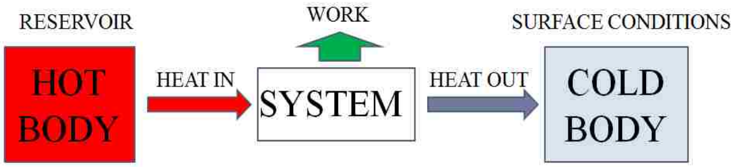

Figure 4.1: Work extraction scheme

Traditionally, the power plant is located at the surface, and the main components are: boiler, turbine, condenser, and a pump. Heat is transferred from the geo-fluid at the boiler stage to the working fluid, which undergoes a phase change. Working fluid vapor enters the turbine at the node 1 and produces work $\dot{W}_{turb.}$ (Figure 4.2). Exhaust vapor then transfers to saturated liquid at the condenser stage. The excessive heat from the working fluid is rejected to the ambient air. Condensed fluid is delivered to the boiler to accomplish the cycle (Moran and Shapiro 2008).

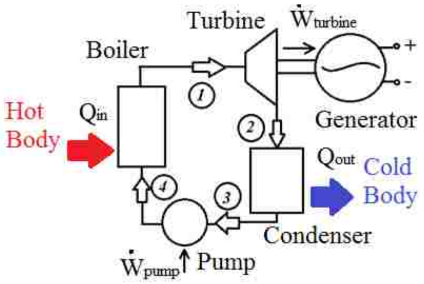

Figure 4.2: Simple Rankine cycle schematic

Literature distinguishes several types of ORCs. If only a portion of the working fluid is converted to vapor at the boiler stage the cycle is recognized as a trilateral flash cycle. It has the lowest efficiency and requires two-phase type expander. Subcritical cycle is one of the widely applied in industrial devices. The two phase region of the working fluid's phase envelope is crossed twice while heating at the boiler and cooling at the condenser (Figure 4.3). However, to get the maximum efficiency of the cycle a secondary working fluid should be compressed and heated to a temperature higher than critical point (Karla et al. 2012). Then the cycle is named as supercritical.

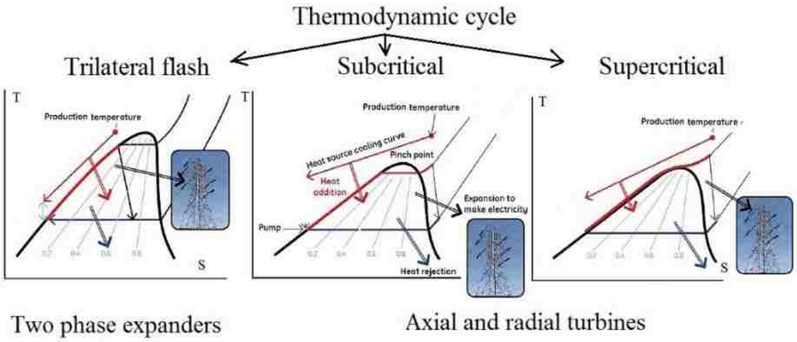

Figure 4.3: Thermodynamic cycle schemes (modified from Karla et al. 2012).

4.2 Working Fluid Selection

4.2.1 Overview of Potential Refrigerants

Despite the fact that water is a natural refrigerant widely used in geothermal applications, the utilization of organic fluids has several advantages: small size turbines with fewer stages are possible, a compact and, hence, less expensive air-cooling system, a possibility to run a cycle at temperatures below the water freezing point, etc. Therefore, commercially available refrigerants applied in the heat and air conditioning industry become more and more popular for small heat harvesting applications (Nalla et. al., 2004; DiPippo, 2004).

The ideal refrigerant characteristics are widely discussed in the literature. In general researchers mentioned an environmental safety, small toxicity, low boiling point with high thermal conductivity, high critical point, low melting point, and no corrosiveness (Karla et al., 2012; Saleh et al. 2007). No real fluid can meet all these requirements. The number of potential candidates diminishes to a short list considering the Kyoto and Montreal protocols prescribing to phase out the production of numerous substances that are responsible for ozone depletion.

All refrigerants are divided into several categories of flammability and toxicity according to the American Society of Heating, Refrigerating, and Air-Conditioning Engineers (ASHRAE) standard 34 (Stand, A., 2010). Fluids with high molecular weight, high thermal conductivity, and high heat transfer coefficients and low critical temperatures are more preferable. According to Karla et al. (2012), Saleh et al. (2007), Schuster et al. (2009), and Hettiarachchi et al., (2007) Iso-Pentane, R123, and n-Butane are the primary fluids for the low enthalpy applications. It is noteworthy to say that the most suitable for this project candidates belong to high flammable and high toxic categories. Unfortunately, there is no a clear-cut winner in the refrigerant selection; hence, only a thermodynamic analysis can clarify the right choice. The optimal energy conversion performance of thermodynamic cycle depends on the type of organic fluid used in the system (Ismail, 2011).

To ease the process of selection, all typical organic fluids are divided into several subgroups as indicated in the Figure 4.4.

- Pure hydrocarbons (e.g. pentane, butane, propane, etc.) (Song, J., 2015),
- Industrial refrigerants (e.g. R134a, R218, R123, R113, R125, etc.),
- Organic mixtures (Panea et al., 2010; Saleh et al., 2007; Hung, 2001; Wei et al., 2007).

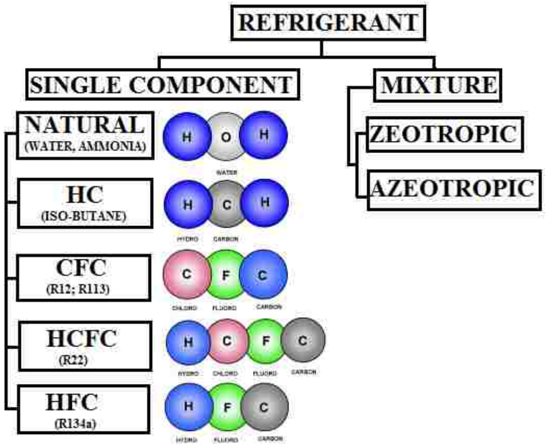

Figure 4.4: Classification of refrigerants according to ASHRAE standards

Hydrocarbons group is characterized with carbon content. Increase in the molecular weight raises the critical pressure and temperature values and, therefore, the two-phase area on the T-S diagram representing useful work of the cycle. These features are highly attractive for this project.

The second group of fluids belongs to commercially available refrigerants widely applicable in air-conditioning and heat pump applications. Mostly they have a positive slope of the vapor line in T-s diagram (R134a) and some of them an infinite slope (R245fa). This may be a turbine safety issue. Additionally, these refrigerants are flammable and toxic.

The last group is organic fluid mixtures that contain the second group's fluids with experimentally defined proportions. Several researchers illustrated superiority of the mixture features compared to single fluid refrigerants (Song, J., 2015; Hung, 2001; Wei et al., 2007), however, it is unclear how stable they are under high pressure and temperature conditions. Therefore, this group is out of consideration.

The selection criteria of organic fluid are listed below (Hettiarachchi et al., 2007; Saleh et al., 2007; Chandrasekharam&Bundschuh, 2008; Ismail, 2011):

Critical pressure and temperature designates the type of thermodynamic process of the system (trilateral, subcritical, or supercritical).

Slope of T-S diagram after the turbine expansion process depends on fluid choice. The dry type fluids (hydrocarbons) have negative vapor line slope on the T-S diagram. This gives some advantages to have superheated gas after the turbine stage. No liquid content ease the vapor transportation into the condenser, and safe turbine blades from destruction.

Specific volume of the fluid defines pump work required to force fluid at a certain rate. The specific volume by definition is inversely proportional to the density, thus, higher the density then less pump work requirement and smaller the expander size.

Safety. The ASHRAE classification describes fluids according to the flammability and toxicity. Flammability is defined according to Lower Flammability Limit (LFL), and toxicity identifies by Threshold Limit Value (TLV). Water and CO_2 belongs to A1/B1 desired class. The hydrocarbons, as well as commercial refrigerants, are mostly highly flammable and toxic, therefore, placed in the A3/B3 group (Figure 4.5).

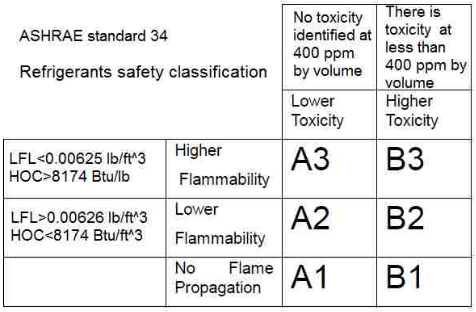

ASHRAE standard 34 Refrigerants safety classification		No toxicity identified at 400 ppm by volume	There is toxicity at less than 400 ppm by volume
		Lower Toxicity	Higher Toxicity
LFL<0.00625 lb/ft^3 HOC>8174 Btu/lb	Higher Flammability	A3	B3
LFL>0.00626 lb/ft^3 HOC<8174 Btu/ft^3	Lower Flammability	A2	B2
	No Flame Propagation	A1	B1

Figure 4.5: ASHRAE standard 34 refrigerants safety classification (Stand, A., 2010).

An environmental criterion is evaluated by both ozone depletion potential (ODP) and global warming potential (GWP). ODP is a measure of substances to react with ozone molecules and destroy the stratospheric ozone layer. R11 refrigerant is taken as a reference with ODP = 1.

GWP is a measure of ability of the fluids to act as a greenhouse gas. The reference is CO_2 with GWP = 1 to evaluate atmospheric lifetime until the gas would decompose or react with other substances. Figure 4.6 illustrates the point. The hydrocarbons have smaller GWP comparing with other popular refrigerant solutions, but the absolute minimum belongs to carbon dioxide.

Gas	Lifetime (years)	20 year	100 year	500 year
CO_2		1	1	1
CFC-11	45	6730	4750	1620
CFC-12	100	11,000	10,900	5,200
HCFC-141b	9.3	2250	725	220
HFC-134a	14	3830	1430	435
Cyclopentane	weeks	<3*	<3*	<3*
Isobutane	weeks	<3*	<3*	<3*
Propane	months	<3*	<3*	<3*

Figure 4.6: Global Warming Potential comparison of popular refrigerants
(Larkin, A., & Davies, K., 2009).

4.2.2 Carbon Dioxide as a Working Fluid

Several researchers experimentally tested carbon dioxide as a working fluid in the PC. Chen et al. (2006) compared CO_2 with R123 in a supercritical power cycle and found that carbon dioxide has higher system efficiency when accounting for heat transfer ability. Additionally, there is no pinch point limit in the heat exchanger. Zhang et al. (2002) suggested using CO_2 as a working fluid for supercritical cycle due to higher cycle efficiency and coefficient of performance (COP). The other researchers (Sarkar, 2015) mentioned satisfying features such as moderate critical point, stability at high pressure/temperature conditions, safety, and low cost. The only problem might be low critical point of 31.1℃ while using it in hot climate regions. Note, carbon dioxide has to be cooled below this critical temperature to be able to condense.

From the other side, operating conditions of 6-16 MPa have safety issues in traditional power plants. In this project, though, it is a suitable advantage for implementation in the deep wells where high hydrostatic pressure will keep CO_2 in supercritical condition at the reservoir depth.

4.2.3 Working Fluid Candidates

All of the mentioned criteria are important but this project have some additional requirements for the fluid selection. First is thermodynamic properties change at high pressure and high temperature. Let us compare the working fluid candidates by their properties change with pressure at assumed constant reservoir temperature of 126℃. Three groups of working fluid candidates were compared: natural refrigerants (CO_2), pure hydrocarbons (n-pentane, butane, etc.), and industrial refrigerants (R245ca, R134a). Water was used for illustration purposes in the plots.

Three parameters were chosen:

- Density, to track the backup pressure at the DHE (Figure 4.7),
- Specific heat, to predict heat extraction at the DHE (Figure 4.8), and
- Thermal conductivity, to predict DHE length (Figure 4.9).

The density change with pressure is tracked in the Figure 4.7. The industrial refrigerants showed the best performance in creating high hydrostatic pressure according to their density change with pressure. Though, this group has the lowest energetic parameters, which would lead to increased DHE length and bigger condensation area. Additionally, they are toxic and moderately flammable.

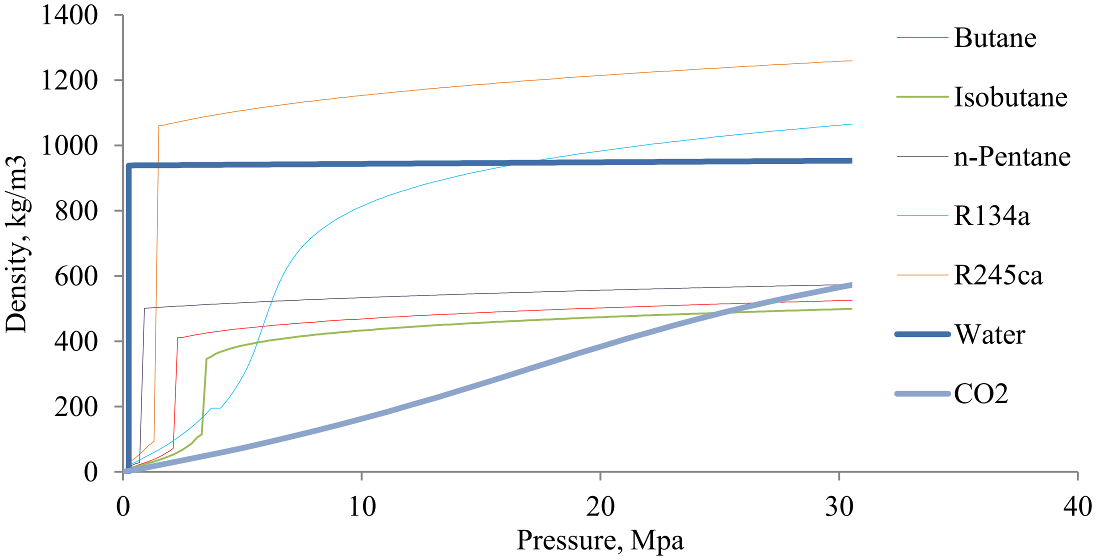

Figure 4.7: Density change with pressure for working fluid candidates.

The hydrocarbons group showed the best performance for energy parameters as was predicted by the literature review. Using them as a working fluids would pay back with a maximum efficiency and power production due to high values of specific heat and thermal conductivity (Figures 4.8 and 4.9).

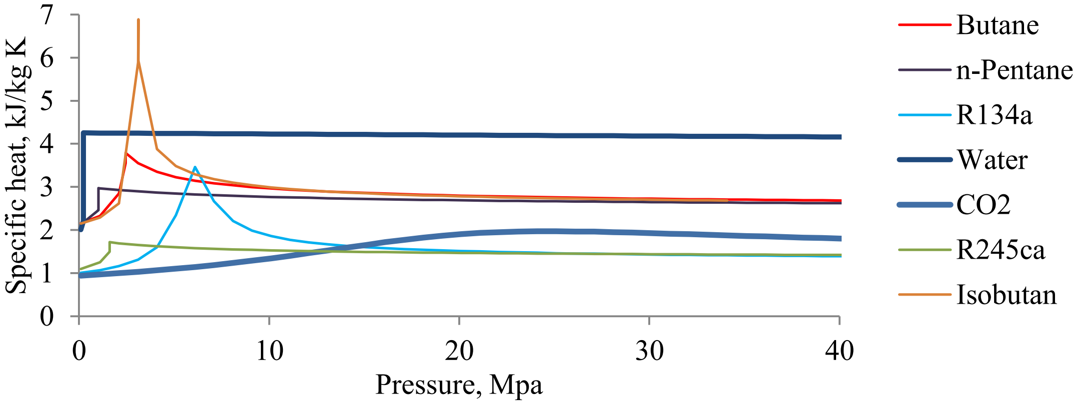

Figure 4.8: Specific heat change with pressure for working fluid candidates.

The greater the molecular weight, the better the power production. However, the increase in molecular weight leads to reduction of condensing temperature, which has a negative effect on the condenser performance. Therefore, N-pentane is the heaviest fluid one can allow to use in this project. The industrial refrigerants showed the worst performance mainly because they are not designed for use in high pressure applications.

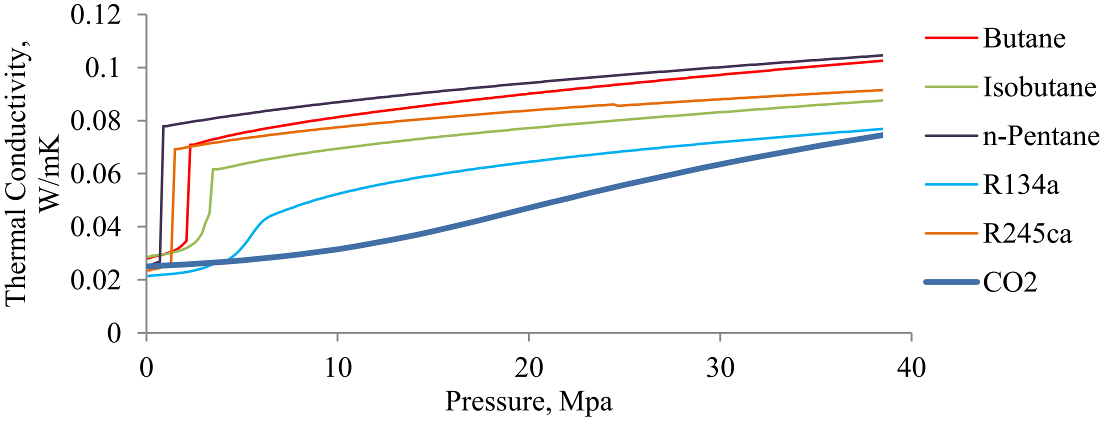

Figure 4.9: Thermal conductivity change with pressure for working fluid candidates. Water thermal conductivity is mainly constant for all range of pressures and equal to 0.7 W/m K.

The next step is to check whether the candidates would stay in one phase at the turbine stage or transform to a two-phase fluid at the vertical hot stream movement. This predetermines the turbine design. Two-phase flow calculations in the vertical section of the well were done using Beggs and Brill method (Brill and Beggs, 1986). The working fluid temperature was kept constant at 126℃ while assuming perfectly insulated vertical pipe with maximum length of 3,048m. Pentane was used as a working fluid. The pipe diameter is 3 inches.

Flow rate was 0.00184m^3/sec. As a result, the flow pattern changed from liquid stage to distributed and then to intermittent regimes between 1905m and 1829m. From 381m up to the top of the well the flow regime changes back to distributed. The fluid does not appear as a pure vapor at the inlet of the turbine, thus, a two phase expander will be required. This phenomenon happens due to no heat flux coming from the walls of the well and phase change occurs only due to pressure drop below saturation pressure. The two phase expanders are not suitable for this project.

Table 4.1: Two-phase flow calculation results using Beggs and Brill method.

Depth, m	3.048 – 1,905	1,905 – 1,829	1,829 – 381	381 - 0
Fluid pattern	100% liquid	Distributed	Intermittent	Distributed

Additionally, hydrocarbons are the lightest candidates and would not be able to create high pressure at the bottom of the well to overcome reservoir pressure. The last comment is that hydrocarbons are very flammable.

Let us construct T-S diagrams for *w.f.* candidates at different reservoir temperatures as shown in the Figures 4.10 and 4.11. As can be seen from the plots the hydrocarbons and popular refrigerant (R22) unavoidably have a two-phase region after the turbine expansion when the reservoir temperature is less than 200℃. To avoid this, the cycle is required to run at high reservoir temperatures. The supercritical stage is possible for n-Pentane at 260C, for R245 ca at 240℃, and for R22 at 220℃. Conversely, carbon dioxide works fine at any reservoir temperature range. As a result this project left with the only choice of natural refrigerant CO_2, which is ecologically clean, non-flammable and has moderate properties. Additionally, there are no state or governmental restrictions or additional requirements for pumping carbon dioxide into a well.

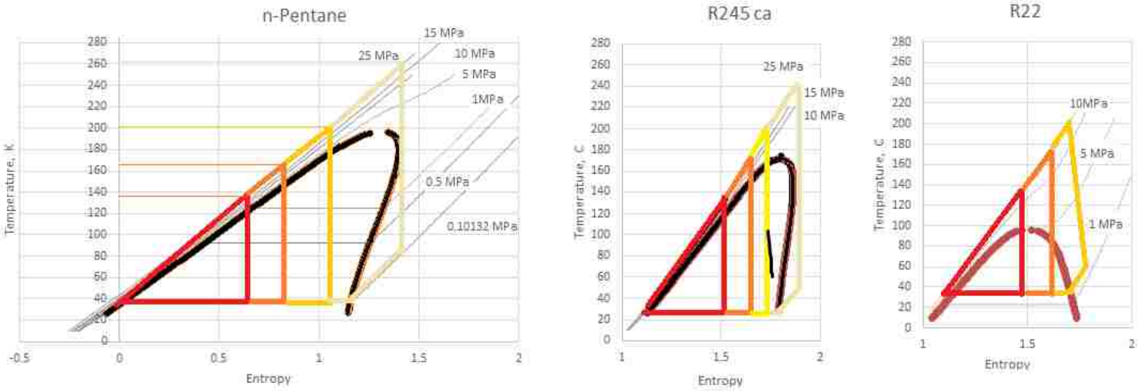

Figure 4.10: Working fluid candidates' T-S diagrams.

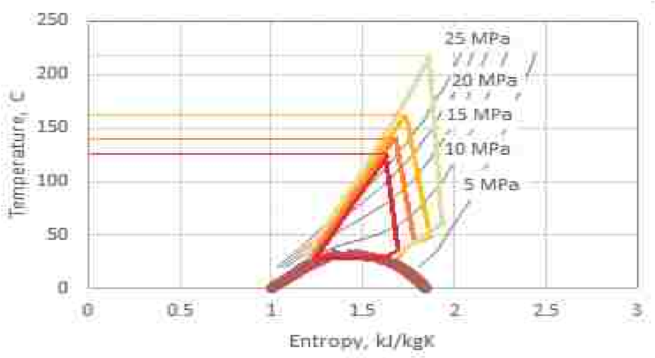

Figure 4.11: CO_2 supercritical cycle.

4.3 Entropy Generation Minimization Analysis

As was said previously, the outer diameter of the horizontal well is predetermined by casing design, which was assumed as 9 5/8 inch. The rest of the DHE diameters installed inside of the gravel pack screen pipe are unknown for now. One may assign randomly the DHE diameters from the available petroleum casings data tables, but the best way is to make the choice based on analysis. To define the flow rate and DHE geometric properties the Entropy Generation Minimization analysis was involved. Note, that the entropy is a measure of imperfection of the system and is defined as (Bejan, 1996):

$$\dot{S}_{gen} = \dot{m}\Delta S - \frac{\dot{Q}}{T} \tag{4.1}$$

From the general combination of the following thermodynamic relations:

$$dh = C_p dT \tag{4.2}$$

$$TdS = dh - \frac{dP}{\rho} \tag{4.3}$$

$$d\dot{Q} = \dot{m}dh \tag{4.4}$$

One can derive for entropy change per DHE unit length:

$$\frac{\dot{S}_{gen}}{dx} = \dot{S}_{gen}{}' = \dot{m}_{br.}C_{pbr.}\frac{\Delta T}{T_m^2(1+\tau)}\frac{dT}{dx} + \frac{\dot{m}_{br.}}{\rho_{br.}T_m}\left(-\frac{dP}{dx}\right)_{br.} \tag{4.5}$$

where $\Delta T = T_m - T_{DHE(wall)}$ is the temperature difference between mean brine stream temperature T_m and the DHE heat transfer wall temperature $T_{DHE(wall)}$; and τ is a temperature ratio:

$$\tau = \frac{\Delta T}{T_m} \tag{4.6}$$

The first and second terms represent entropy generation rate per unit length of heat exchanger due to heat transfer to the working fluid and brine pressure drop due to frictional losses respectively.

- First term development of the equation 4.5

Under steady state assumptions the heat transfer rate through the heat exchanger is:

$$d\dot{Q} = \dot{m}_{br.}C_{pbr.}dT = h_{a2}\pi D_{DHE}dx\Delta T_{lm} \tag{4.7}$$

Assuming linear change of the temperature difference between the inner wall and mean temperature for the distance dx of the heat exchanger one can approximate:

$$\Delta T = \Delta T_{lm} = \frac{\dot{m}_{br.}C_{pbr.}}{h_{a2}\pi D_{DHE}}\frac{dT}{dx} \tag{4.8}$$

Substituting equation (4.8) to equation (4.7) with assumption of $\tau \ll 1$:

$$\dot{m}_{br.}C_{pbr.}\frac{\Delta T}{T_m^2(1+\tau)}\frac{dT}{dx} = \frac{\left(\dot{m}_{br.}C_{pbr.}\right)^2}{h_{a2}\pi D_{DHE}T_m^2}\left(\frac{dT}{dx}\right)^2 \tag{4.9}$$

The heat transfer process takes place across the DHE wall. Then the heat transfer coefficient is:

$$h_{a2} = St\,\rho_{br.}\,C_{pbr.}\,u_{a2} \tag{4.10}$$

where

$$u_{a2} = \frac{4\dot{m}_{br.}}{\pi\rho_{br.}{D_{a2}}^{2}} \tag{4.11}$$

Hydraulic diameter of brine flow annulus (see Figure 4.12):

$$D_{a2} = D_{well} - D_{DHE} = D_{DHE}(r-1) \tag{4.12}$$

where

$$r = \frac{D_{well}}{D_{DHE}} \tag{4.13}$$

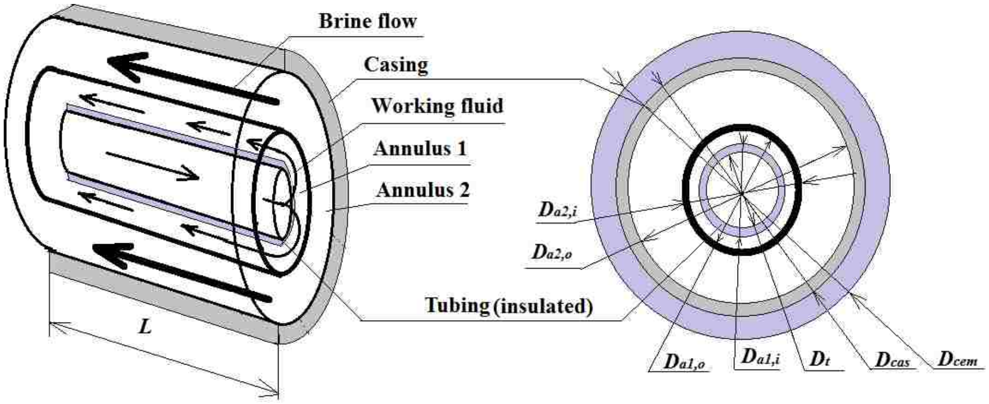

Figure 4.12: DHE schematic

Introducing Nusselt number (Incopera, 1990):

$$Nu_{br.} = St\,Re_{br.}Pr_{br.} \tag{4.14}$$

Eventually the first term of equation 4.5 becomes:

$$\frac{\left(\dot{m}_{br.}C_{pbr.}\right)^{2}}{h_{a2}\pi D_{DHE}T_{m}^{2}}\left(\frac{dT}{dx}\right)^{2} = \frac{\pi\dot{m}_{br.}C_{pbr.}\rho_{br.}D_{DHE}Re_{br.}Pr_{br.}(r-1)^{2}}{4Nu_{br.}T_{m}^{2}}\left(\frac{dT}{dx}\right)^{2} \tag{4.15}$$

The flow in the production side has a complicated pattern. The DHE is a circular pipe, but the outer wall is a design of porous gravel pack and screen pipe from which the influx occur. Let us assume that the flow is fully developed. To simplify the problem let us take Petukhov and Roizen correlation for Nu in turbulent flow:

$$Nu_{br.} = 0.023{Re_{br.}}^{0.8}{Pr_{br.}}^{0.3} \tag{4.16}$$

Then, eventually the first term of equation (4.5) becomes:

$$\frac{\left(\dot{m}_{br.}C_{pbr.}\right)^2}{h_{a2}\pi D_{DHE}T_m^2}\left(\frac{dT}{dx}\right)^2 = 10.87\frac{\pi\dot{m}_{br.}C_{pbr.}\rho_{br.}D_{DHE}{Re_{br.}}^{0.2}{Pr_{br.}}^{0.7}(r-1)^2}{T_m^2}\left(\frac{dT}{dx}\right)^2 \tag{4.17}$$

- Second term development of the equation 4.5

The pressure drop per unit length is defined as follows and expanding Reynolds number as:

$$Re_{br.} = \frac{4\dot{m}_{br.}}{\pi\mu_{br.}(D_{well} - D_{DHE})} = \frac{4\dot{m}_{br.}}{\pi\mu_{br.}D_{DHE}(r-1)} \tag{4.18}$$

$$\left(\frac{dP}{dx}\right)_{DHE} = f\frac{8{\dot{m}_{br.}}^2}{\pi^2\rho_{br.}{D_{DHE}}^5(r-1)^5} = f\frac{{Re_{br.}}^2{\mu_{br.}}^2}{2\rho_{br.}{D_{DHE}}^3(r-1)^3} \tag{4.19}$$

Using Blasius approximation for frictional pressure drop with assumption of equal friction at the outer and inner pipes:

$$f = 0.316{Re_{br.}}^{-0.25} \tag{4.20}$$

Expanding Reynolds number and substituting into the second term will receive:

$$\frac{\dot{m}_{br.}}{\rho_{br.}T_m}\left(-\frac{dP}{dx}\right)_{br.} = -0.158\frac{\dot{m}_{br.}{\mu_{br.}}^2{Re_{br.}}^{1.75}}{{\rho_{br.}}^2T_m{D_{DHE}}^3(r-1)^3} \tag{4.21}$$

Finally:

$$\frac{\dot{S}_{gen}}{dx} = \frac{10.87\pi\dot{m}_{br.}C_{pbr.}\rho_{br.}D_{DHE}{Re_{br.}}^{0.2}{Pr_{br.}}^{0.7}(r-1)^2}{T_m^2}\left(\frac{dT}{dx}\right)^2 - \frac{0.158\dot{m}_{br.}{\mu_{br.}}^2{Re_{br.}}^{1.75}}{{\rho_{br.}}^2T_m{D_{DHE}}^3(r-1)^3} \tag{4.22}$$

At any system design the entropy generation rate should be close to zero to maintain high efficiency. So, equating ${\dot{S}_{gen}}' = 0$ and finding the expression for $Re_{br.}$:

$$Re_{br.}{}^{1.55} = 68.79\frac{\pi\dot{m}_{br.}C_{pbr.}\rho_{br.}D_{DHE}Re_{br.}{}^{0.2}Pr_{br.}{}^{0.7}(r-1)^2\rho_{br.}{}^2T_mD_{DHE}{}^3(r-1)^3}{\dot{m}_{br.}\mu_{br.}{}^2T_m^2}\left(\frac{dT}{dx}\right)^2$$

(4.23)

or simplifying will have:

$$Re_{br.} = \left\{68.79\left(\frac{\pi C_{pbr.}\rho_{br.}{}^3Pr_{br.}{}^{0.7}}{\mu_{br.}{}^2}\right)\left[D_{DHE}{}^4(r-1)^5\right]\left[\left(\frac{dT}{dx}\right)^2\frac{1}{T_m}\right]\right\}^{0.645} \tag{4.24}$$

In terms of brine mass flow rate:

$$\dot{m}_{br.} = 4D_{DHE}{}^{3.58}(r-1)^{4.22}\left(\frac{dT}{dx}\right)^{1.29}N^{0.645} \tag{4.25}$$

where

$$N = \frac{C_{pbr.}\rho_{br.}{}^3Pr_{br.}{}^{0.7}}{\mu_{br.}{}^2T_m} \tag{4.26}$$

Integrating the equation 4.25 one can predict the flow rate change depending on DHE diameter variation and reservoir temperature drop in the heat extraction system. Note: in this derivation the pressure drop in the completion was ignored. Figures 4.13, 4.14, and 4.15 show brine mass flow rate development with respect to the chosen Annulus 2 diameter for different temperature drops at the DHE. Unrealistic flow rates were received with simulations of 20°C temperature drop at the heat exchanger (Figure 4.13). Increasing temperature up to 50°C gives the desired flow rate range.

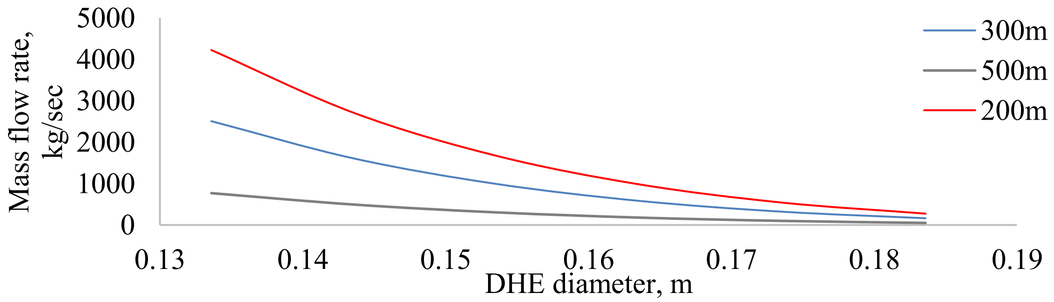

Figure 4.13: Brine mass flow rate change with DHE diameter variation. 20°C temperature drop at the heat exchanger.

The Figure 4.16 shows data in dimensionless form. With increasing the 1/r value (or reducing the annular space D_{a2}) the $Re_{br.}$ reduces, due to frictional pressure losses. Besides, shorter the DHE length gives higher Reynolds number as expected.

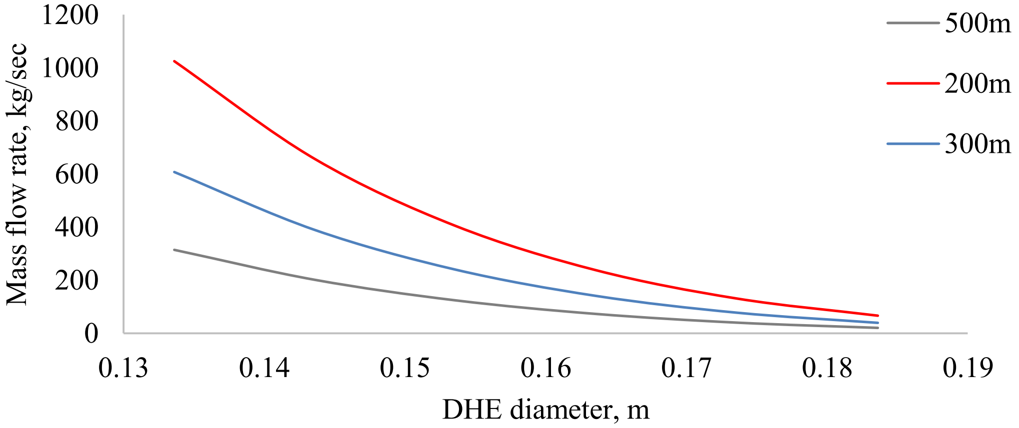

Figure 4.14: Brine mass flow rate change with DHE diameter variation.
10°C temperature drop at the heat exchanger.

The outer diameter (screen pipe) is constant. The flow rate drops with decreasing the annulus hydraulic diameter.

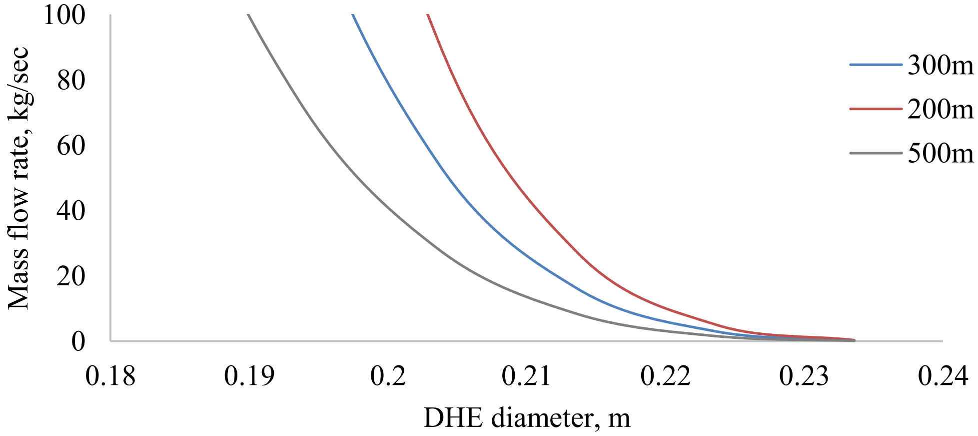

Figure 4.15: Brine mass flow rate change with DHE diameter variation.
50°C temperature drop at the heat exchanger.

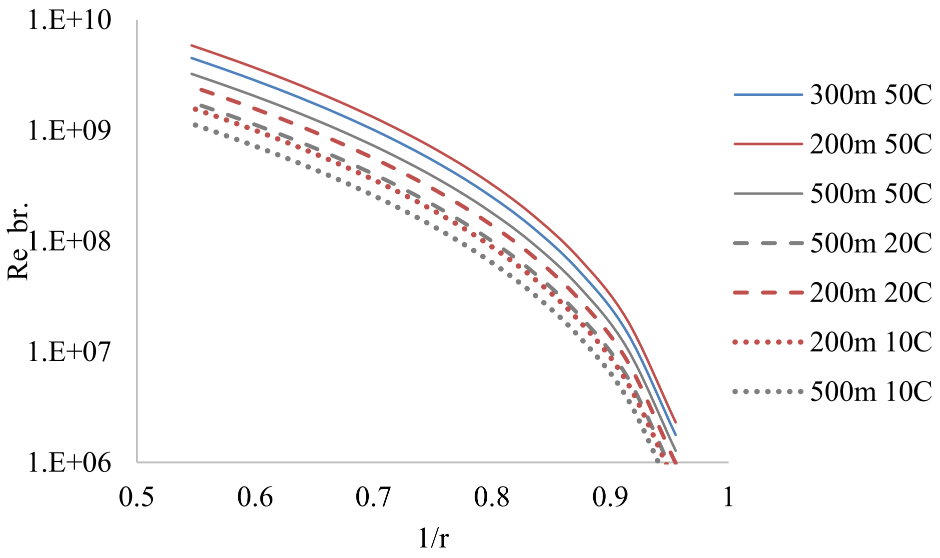

Figure 4.16: Reynolds number change with reducing annular space of the DHE.

The same derivation process was done for the working fluid. The only difference is in determining the Nusselt number. Here the heat transfer occur at the outer diameter, so Petukhov and Roizen correlation was used for circular pipe annulus and insulated tubing.

$$\frac{Nu_{wf.}}{Nu_{tub.}} = 1 - 0.14s^{0.6} \tag{4.27}$$

where

$$Nu_{tub.} = 0.023{Re_{br.}}^{0.8}{Pr_{br.}}^{0.4} \tag{4.28}$$

and

$$s = D_{DHE(in)} - D_{tub.} \tag{4.29}$$

The obtained solution for the Reynolds number is:

$$Re_{wf.} = \left\{68.79\left(\frac{\pi Cp_{wf.}{\rho_{wf.}}^{3}{Pr_{wf.}}^{0.7}}{{\mu_{wf.}}^{2}}\right)\left[\frac{{D_{DHE}}^{4}(1-q)^{5}}{1-0.14s^{0.6}}\right]\left[\left(\frac{dT}{dx}\right)^{2}\frac{1}{T_m}\right]_{wf.}\right\}^{0.645} \tag{4.30}$$

Figure 4.17 shows the mass flow rate growth with DHE diameter reduction for 200m DHE length case. Increase in temperature leads to increasing the flow rate.

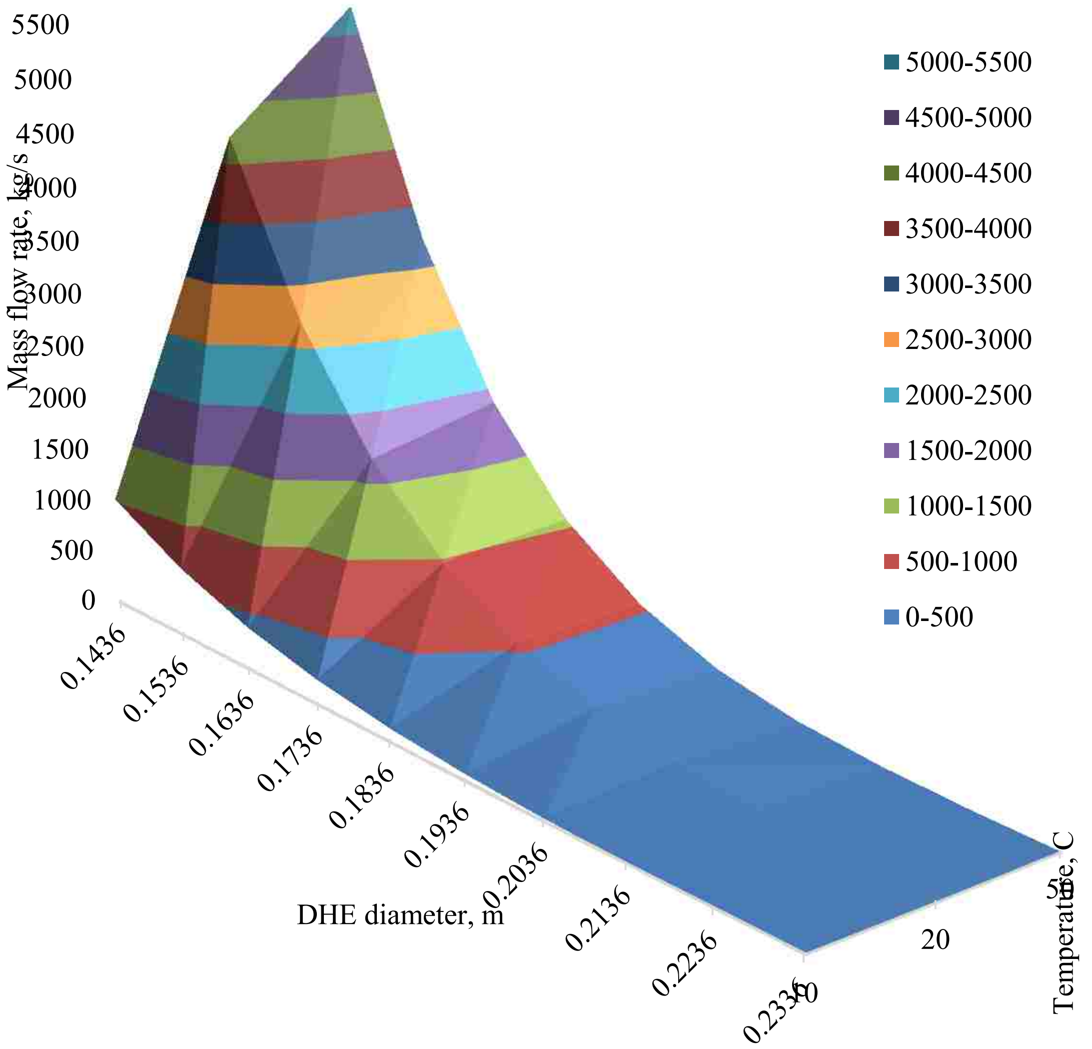

Figure 4.17: 200m DHE length performance.

Interesting relation can be obtained if one takes the ratio of the Reynolds numbers in both annuluses:

$$\frac{Re_{br.}}{Re_{wf.}} = \left(\frac{68.79\left(\frac{\pi Cp_{br.}\rho_{br.}{}^{3}Pr_{br.}{}^{0.7}}{\mu_{br.}{}^{2}}\right)\left[D_{DHE(out.)}{}^{4}(r-1)^{5}\right]\left[\left(\frac{dT}{dx}\right)^{2}\frac{1}{T_m}\right]_{br.}}{68.79\left(\frac{\pi Cp_{wf.}\rho_{wf.}{}^{3}Pr_{wf.}{}^{0.6}}{\mu_{wf.}{}^{2}}\right)\left[\frac{D_{DHE(in.)}{}^{4}(1-q)^{5}}{1-0.14q^{0.6}}\right]\left[\left(\frac{dT}{dx}\right)^{2}\frac{1}{T_m}\right]_{wf.}} \right)^{0.645} \qquad (4.31)$$

or simplifying:

$$\frac{Re_{br.}}{Re_{wf.}} = \left(\left(\frac{Cp_{br.}}{Cp_{wf.}}\right) \left(\frac{\rho_{br.}}{\rho_{wf.}}\right)^{3} \left(\frac{D_{DHE(out.)}}{D_{DHE(in.)}}\right)^{4} \left(\frac{r-1}{1-q}\right)^{5} (1 - 0.14q^{0.6}) \left(\frac{{Pr_{br.}}^{0.7}}{{Pr_{wf.}}^{0.6}}\right) \left(\frac{\left(\frac{dT}{dx}\right)_{br.}}{\left(\frac{dT}{dx}\right)_{wf.}}\right)^{2} \left(\frac{T_{mwf.}}{T_{mbr.}}\right) \left(\frac{\mu_{wf.}}{\mu_{br.}}\right)^{2} \right)^{0.645} \qquad (4.32)$$

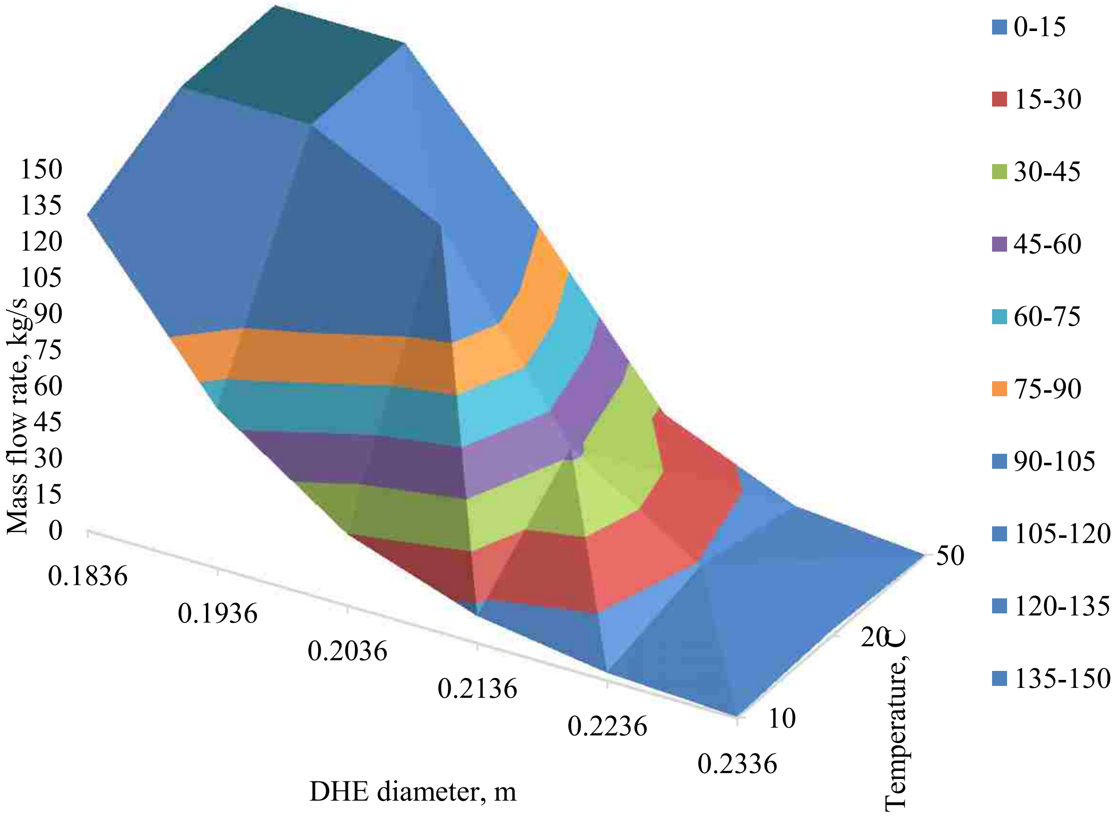

Figure 4.18: 200m DHE length performance. Closer look at 0.18-0.23 m interval.

From equation 4.32 it is easy to see the dimensionless parameters. From observation, one would desire the brine flow rate to be small to reduce brine pump load. High *w.f.* flow rate means more net power production. Table 4.2 illustrates the DHE design data based on previous analysis.

Table 4.2: Chosen completion geometry of production and injection sides

Cement sheath	
OD	12.527 inch (0.318 m)
Casing 2	
OD	9.625 inch (0.244m)
ID	8.031 inch (0.204 m)
Screen pipe (gravel pack, ICD)	
OD	6.190 inch (0.157 m)
ID	4.890 inch (0.124 m)
Casing 1 (only production)	
OD	3.5 inch (0.089 m)
ID	2.992 inch (0.076m)
Coiled tubing (only production)	
OD	1.990 inch (0.051 m)
ID	1.650 inch (0.042 m)

4.4 Nodal Analysis.

A reservoir prototype data was used for the numerical analysis. The thermodynamic analysis was performed by dividing the *w.f.* flow path into several intervals by the nodes as shown in the Figure 4.19, where fluid properties are defined using NIST Chemistry Web book fluid properties solver. The red and blue colors represent hot and cold streams respectively. The pressure drop is negligible between turbine exit and condenser inlet (node 10) as well as condenser outlet and well inlet (node 1). Therefore, the condenser is omitted in the scheme. Table 4.3 gives a location description of each node on the scheme.

Frictional pressure drop ΔP $_{\text{friction}}$ is obtained from integration of frictional pressure gradient:

$$\frac{dP}{dz} = -\frac{f\rho_{w.f.}\, v_{w.f.}{}^{2}}{2\, D_{w.f.}} \tag{4.33}$$

where z is the well depth; $v_{w.f.}$ is fluid velocity; $D_{w.f.}$ is pipe diameter.

Friction factor f was obtained from the Chen's relationship:

$$\frac{1}{f} = \left[2\log\left(\frac{\epsilon/d}{3.7065} - \frac{5.0452}{Re}\log \Delta\right)\right]^{2} \tag{4.34}$$

$$\Delta = \frac{\epsilon/d^{1.1098}}{2.8257} + \left(\frac{7.149}{Re}\right)^{0.8981} \tag{4.35}$$

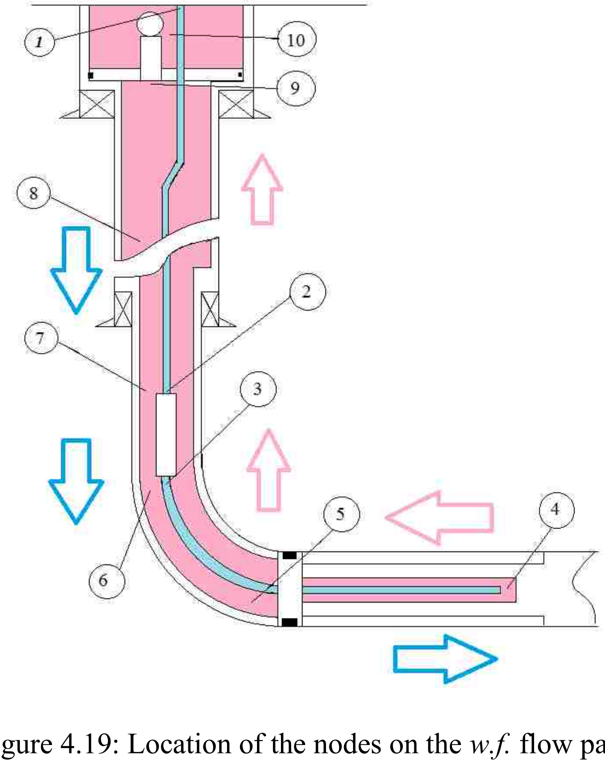

Figure 4.19: Location of the nodes on the *w.f.* flow path.

Reynolds number for annulus is calculated from:

$$Re = \frac{\rho V D_h}{\mu} \tag{4.36}$$

Pipe diameter (D_h) can be assumed as a hydraulic diameter for the annulus flow:

$$D_h = \frac{D_{outer} - D_{inner}}{2} \tag{4.37}$$

Turbine efficiency:

$$\eta_t = \frac{h_9 - h_{10}}{h_9 - h_{10s}} \tag{4.38}$$

W.f. pump efficiency:

$$\eta_{pump} = \frac{h_2 - h_3}{h_2 - h_{3s}} = \frac{P_4 - P_3}{\rho(h_4 - h_3)} \tag{4.39}$$

Table 4.3: Nodal analysis description

Node intervals	Description
1-2	Flow downward vertically inside the 5” casing to the DHE
2-3	Pump work
3-4	Flow downward through the curvature radius and inside the insulated 2” production tubing toward the end of DHE
4-5	Enthalpy increase in the DHE.
5-6; 6-7; 7-8; 8-9	Flow vertically upward inside the radius, and (6.625-5)”, (8.825-5”); (15-5”) annuluses respectively
9-10	Turbine pressure expansion line
10-1	Cooling process in the condenser

The T-S diagram is illustrated in the Figure 4.19. Intervals 5-9, 1-2, and 3-4 are insulated, therefore, illustrated as a straight lines of constant temperature. Node 1 represents the liquid CO_2 stage entering the well. Fluid is directed into the vertical well and travels downward inside the 5 inch OD insulated tubing. Pressure increases gradually from 7.5 to 48.87 MPa with constant temperature 30℃ (Figure 4.20). Fluid density grows from 661 to 1012 kg/m^3. Entropy and enthalpy are reduced, except the interval 2-3 (Figure 4.21). This jump in pressure and temperature represents w.f. pump work. The location of the pump is 4770 m right before the radius. This position was chosen with pump safety concerns and minimum power requirement. Additionally, the highest density location is preferable to reduce pump energy consumption.

Table 4.4: Thermodynamic properties of working fluid.

Node	P MPa	ρ kg/m^3	T ℃	h kJ/kg	S kJ/kg K	Cp kJ/kg K	k W/K	μ*10^(-5) Pa*s
1	7.50	661.10	30.0	291.7	1.30	8.13	0.078	5.6
	14.54	840.00	30.0	260.5	1.17	2.45	0.094	7.8
	22.36	907.05	30.0	253.5	1.11	2.07	0.108	9.4
	30.81	952.02	30.0	250.6	1.07	1.91	0.110	10.5
	39.69	988.11	30.0	249.9	1.04	1.81	0.120	11.7
2	48.87	1016.2	30.0	250.7	1.02	1.76	0.134	12.7
3	53.87	1017.0	35.0	260.2	1.04	1.73	0.135	12.7
	55.01	1020.1	35.0	260.3	1.03	1.72	0.135	12.8
	55.00	1019.9	35.0	260.3	1.03	1.72	0.135	12.6
4	54.99	895.39	80.3	338.7	1.27	1.72	0.109	9.08
	54.99	840.46	101.0	373.8	1.36	1.70	0.099	8.01
	54.98	813.06	111.2	391.6	1.41	1.69	0.097	7.55
	54.98	800.08	116.5	400.0	1.43	1.69	0.094	7.34
5	54.96	792.48	120.3	405.1	1.44	1.68	0.093	7.24
6	53.34	783.04	120.3	405.1	1.44	1.70	0.092	7.09
7	51.12	782.00	120.3	407.8	1.45	1.72	0.087	7.08
	49.25	760.20	120.3	409.6	1.46	1.72	0.087	7.01
	47.22	747.15	120.3	411.0	1.49	1.75	0.085	6.51
	45.21	734.09	120.3	415.0	1.53	1.75	0.083	6.30
	43.18	719.83	120.3	420.1	1.55	1.78	0.081	6.185
8	39.22	687.23	120.3	427.0	1.59	1.82	0.083	7.71
	35.59	653.51	120.3	438.3	1.62	1.91	0.073	6.39
	32.06	613.30	120.3	444.8	1.65	1.94	0.069	4.90
	28.74	568.26	120.3	449.3	1.67	1.98	0.063	4.54
	25.67	519.12	120.3	453.9	1.69	2.03	0.056	3.97
	24.55	498.76	120.3	458.6	1.71	2.04	0.055	3.71
	22.34	454.03	120.3	461.8	1.72	2.03	0.051	3.50
9	21.27	432.10	120.3	467.6	1.74	2.03	0.051	3.46
10	8.00	301.69	49.51	435.7	1.76	4.33	0.043	2.38

The 3-4 interval is again insulated pipe flow through the well curvature inside of the horizontal well. Node 4 is the end of the heat exchanger. After this the flow is reversed and returns toward the surface.

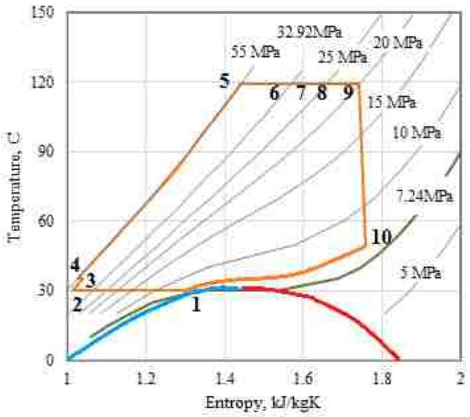

Figure 4.20: T-S diagram.

The line 4-5 represents the temperature rise inside of the DHE. Pressure is slowly reduced by friction, and temperature is increased to 120.3°C. Temperature rise affects density drop by 100kg/m^3, and entropy, enthalpy growth.

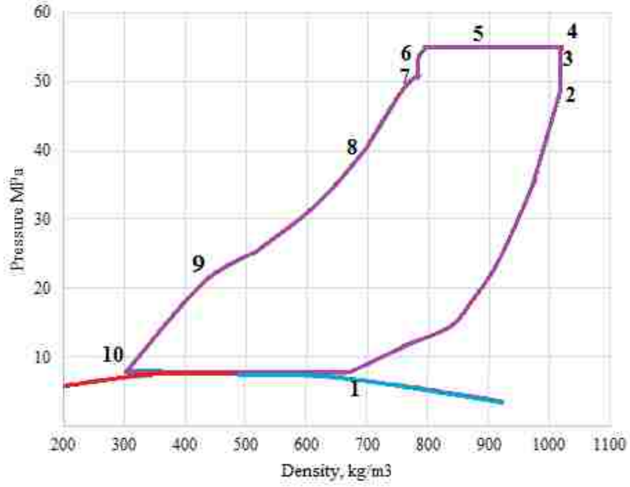

Figure 4.21: Pressure-density diagram.

The following nodes 5,6,7,8,9 represent flow inside of the vertical insulated annuluses according to the casing design right up to the turbine. Pressure is reduced to 21.2MPa, but temperature is assumed constant 120.3C. The enthalpy in this stage is the maximum of the cycle and equal to 467 kJ/kg. The turbine expansion reduces pressure to 8 MPa. Graphically the thermodynamic properties change is illustrated in the figures below. The red and blue lines represent liquid and vapor sides of saturation curve.

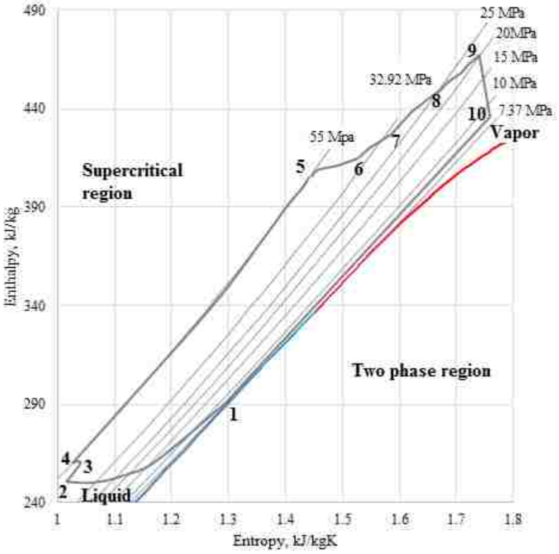

Figure 4.22: Enthalpy-entropy diagram. The well locations are shown by the numbers.

4.5 Ambient and reservoir Temperature Change

With changing the hot and cold sides of the system the T-S diagram is reflects the cycle properties alteration. The Figure 4.23 shows four cases of study.

Case1: Initial diagram (T_R=126℃; $T_{amb.}$=25℃)

The turbine drops pressure from 20 to 8 MPa as was described previously. Condenser pressure is higher than CO_2 critical pressure, therefore, the process has only a single phase flow in the condenser (Figure 4.23 a).

Case 2: Ambient temperature increase (T_R=126℃; $T_{amb.}$=35℃);

Increase in ambient temperature associated with increasing the condenser pressure up to 10 MPa. This process reduces turbine work and increases DHE pressure (Figure 4.23 b).

Case 3: Reservoir temperature drop (T_R=105°C; $T_{amb.}$=25°C)

Here the reservoir temperature drops. The process is associated with turbine work reduction, due to hot w.f. enthalpy drop (Figure 4.23 c).

Case 4: Ambient temperature drop (T_R=126°C; $T_{amb..}$=15°C)

The ambient temperature reduction leads to increasing the turbine work and rejected heat from the condenser. The pressure after the turbine is reduced and the process undergoes through the two-phase region (Figure 4.23 d).

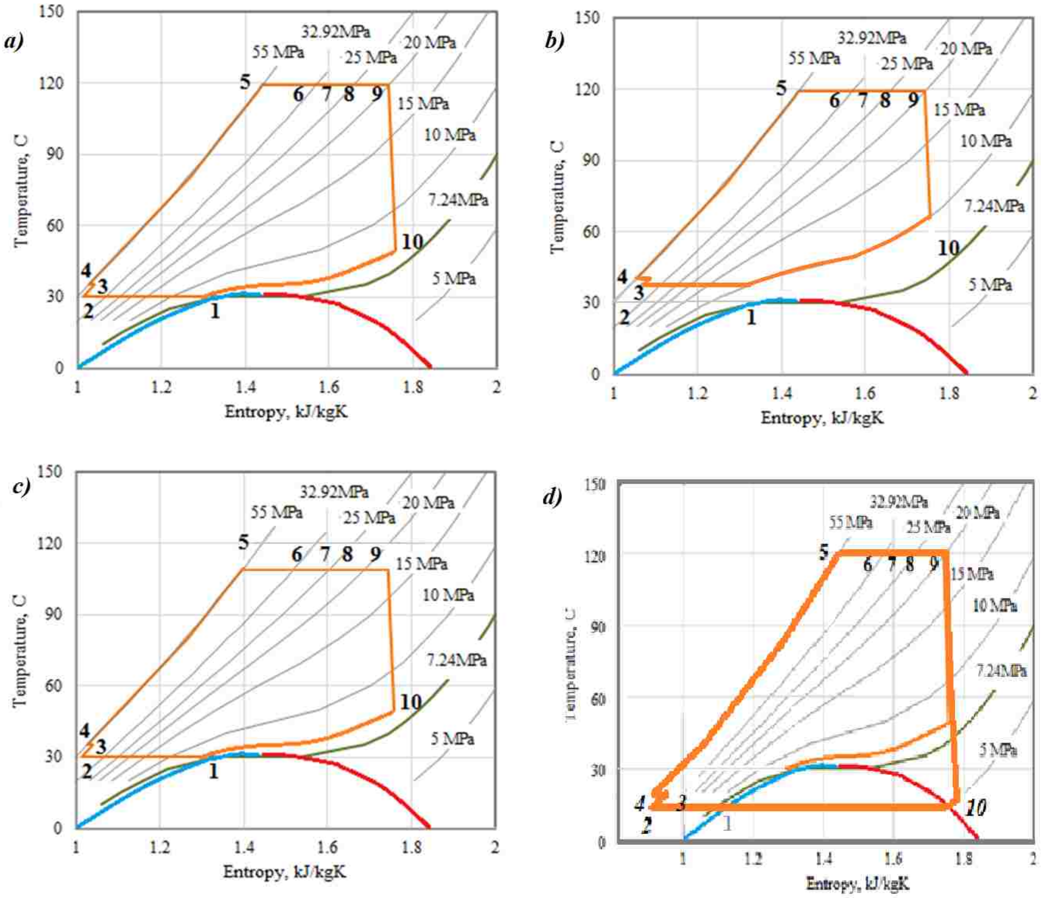

Figure 4.23: T-S diagram shift with ambient and reservoir temperature changes.
a) Initial diagram (T_R=126°C; $T_{amb.}$=25°C);
b) Ambient temperature increase (T_R=126°C; $T_{amb.}$=35°C);
c) Reservoir temperature drop (T_R=105°C; $T_{amb.}$=25°C);
d) Ambient temperature drop (T_R=126°C; $T_{amb..}$=15°C).

4.6 Conclusions

- The choice of the working fluid fell on carbon dioxide due to safety and toxicity requirements; satisfactory thermodynamic properties to produce work in the system, and ability to provide high pressure at the DHE. Additionally, CO_2 is chemically stable, cheap and abundant.
- Thermodynamic analysis proved sustainability of the supercritical CO_2 cycle.
- The ambient temperature fluctuations make some impact on condenser pressure and thermodynamic cycle. Increasing the ambient temperature leads to increasing the condenser pressure. At the same time turbine work is reduced. Drop in ambient temperature reduces condenser pressure and process undergoes two phase region in the T-S diagram.
- The maximum condenser area is expected when the cycle works at low ambient temperatures. Therefore, in condenser calculations the lowest ambient temperature should be taken as a design parameter for the particular geographical location of the reservoir.

CHAPTER 5: NUMERICAL MODELING

“Where we cannot invent, we may at least improve”
Charles Caleb Colton

The purpose of this chapter is to introduce the reader with numerical analysis of the system. The input data is taken from the reference reservoir and in later discussion is expanded for any kind (temperature, permeability, depth) of sediment aquifer. Another goal is to track the net power production in order to choose the “right” reservoir for ZMW application.

5.1 Assumptions

- The geo-fluid is assumed as incompressible single phase Newtonian fluid. There is no fluid accumulation in the pipe; flow regimes are fully developed. Brine’s chemical composition change due to reservoir temperature change is negligible.
- The system operates at a steady state condition.
- The pressure drawdown area around the well is assumed to have an elliptical shape for both production and injection sides.
- The well is performed as a cased cemented completion to avoid collapsing on the producer side and burst on the injection side. The horizontal casing diameter for this project was chosen as 9 5/8 inch outside diameter (OD). For simplicity purposes it was assumed to run the same diameter pipe for both: the production and injection sides of the well.

5.2 Completion Design Modeling

There are three main sections in the deviated portion of the well: production, injection, and insulation section in between. To analyze the pressure development in the completion scheme, the wellbore was divided by nodes as illustrated in the Figure 5.1. As soon as the brine pump starts driving geo-fluid from the production to the injection side the pressure difference from the reservoir pressure develops at each node. The maximum flow rate is expected in the closest node to the pump due to the unequal well flowing pressure distribution (Anklam et al., 2005; Ouyang et al., 1997).

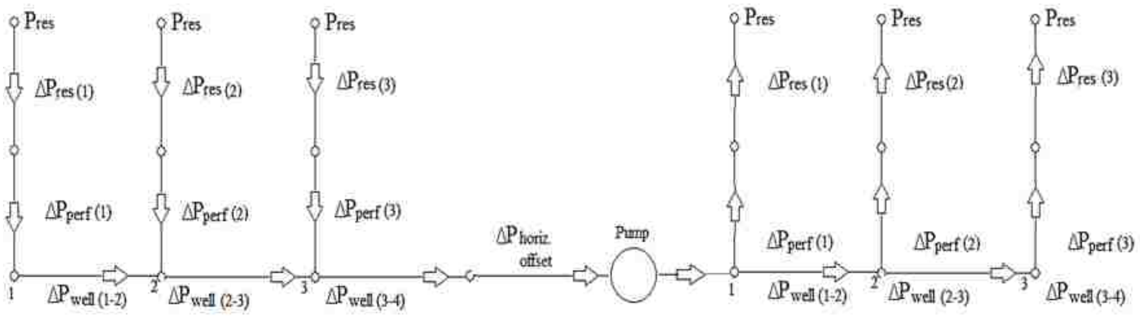

Figure 5.1: Pressure distribution scheme along the horizontal well.
Only three nodes are illustrated for clarity.

5.2.1 Production-Injection Intervals

The mathematical problem describing fluid flow with influx through the horizontal porous pipe wall was considered as unsolvable several of decades ago. The first attempts were to assume a single phase isothermal fluid flowing with no energy losses along the pipe. This assumption leads to the wrong conclusions such that constant influx rate along the pipe. In fact, the inflow rate is not constant due to pressure losses in the pipe (Ouyang et. al., 1997).

Traditional methods of pressure drop analysis account for three main terms of energy losses caused by friction, acceleration, and gravity. To obtain valuable results these parameters should be carefully evaluated with great concern of the fluid flow regime. Anklam (2005) explored horizontal perforated wells and derived a tubing performance relationship equation. She showed that pressure in the well increases along the pipe length moving from the heel to the toe region, and flow rate decreases from the reservoir into the well.

The method of mathematical modelling is straight forward. The arrangement is divided into several intervals, containing influx and outflow segments and a circular horizontal pipe between them. Assuming the reservoir pressure as known, one can specify the brine pump pressure. According to the mass conservation law for incompressible fluids, the total flow into the horizontal well is described by sum of the reservoir i-flows through the n-interval perforations:

$$q_{tot} = \sum_{i=1}^{n} q_{(i)} \tag{5.1}$$

The well flowing pressure of the each node is a conceptual pressure at which the influx for the interval is calculated. The difference in reservoir P_e and well flowing pressure at each *i-th* node $P_{wf(i)}$ is a sum of losses in the perforations, gravel pack and rock porous media.

$$\Delta P_{(i)} = P_{res.} - P_{wf(i)} \tag{5.2}$$

where the pressure $\Delta P_{(i)}$ is a sum of pressure resistances in the reservoir ΔP_{res} and a gravel pack ΔP_{gravel} :

$$\Delta P_{(i)} = \Delta P_{res(i)} + \Delta P_{gravel(i)} \tag{5.3}$$

Combining equations (5.2) and (5.3) and explaining each pressure term as a multiplication of flow resistance and flow rate will receive:

$$P_{res} - P_{wf(i)} = \Delta R_{res(i)} q_{in(i)} + DF_{(i)} q_{in(i)}^2 + NDF_{(i)} q_{in(i)} \tag{5.4}$$

where *DF* and *NDF* are flow resistances (non-Darcy and Darcy terms) of gravel pack pressure drop. The gravel pack is assumed as 20/40 mesh sand with 135D permeability from the Weatherford catalog.

From the other side, the pressure drop between the nodes is defined in terms of friction *F*, acceleration *Ac*, direction *Dr*, and gravity *Gr* components of pressure losses in the circular pipe. The friction factor for production/injection intervals is defined from (Ouyang et al., 1997). The gravity term is positive with assumption of negative slope inclination from the horizontal axis.

$$P_{wf(i-1)} - P_{wf(i)} = F_{(i)} q_{tot}^2 + Ac_{(i)} q_{(i)} + Dr_{(i)} q_{in(i)}^2 - Gr_{(i)} \tag{5.5}$$

To eliminate the unknown well flowing pressure term let us add equations (5.4) and (5.5):

$$P_{res} - P_{wf(i-1)} = \\ R_{perf(i)} q_{in(i)} + DF_{(i)} q_{in(i)}^2 + NDF_{(i)} q_{in(i)} + F_{(i)} q_{tot}^2 + Ac_{(i)} q_{(i)} + Dr_{(i)} q_{in(i)}^2 - Gr_{(i)} \tag{5.6}$$

For *i=1* the well flowing pressure is equal to the pump drawdown $P_{\substack{br.\\pump.}}$. The quadratic equation 5.6 contains only one unknown $q_{(i)}$, and solving for a positive root:

$$q_{(i)} = \frac{-B + \sqrt{B^2 - 4AC}}{2A} \tag{5.7}$$

where

$$A = DF_{(i)} + Dr_{(i)} \quad (5.8)$$

$$B = \Delta P_{perf(i)} + NDF_{(i)} + Ac_{(i)} \quad (5.9)$$

$$C = F_{(i)} q_{tot}^2 - \left(P_{res.} - P_{b.p.}\right) - Gr \quad (5.10)$$

The solution algorithm based on equation 5.6, which gives the system of equations equal to the number of nodes. The system components are shown in the Table 5.1. Three interval case is shown for illustration purposes. At the last node the acceleration pressure drop is equal to zero.

Table 5.1: Coefficients of the Eqn. (5.6).

Node	A	B	C
1	DF_1 $+ Dr_1$	$R_{perf1} + NDF_1$	$F_1(q_{tot} - q_3 - q_2)^2 + F_2(q_{tot} - q_3)^2 + F_3(q_{tot})^2 + Ac_2 q_2 + Ac_3 q_3 + Dr_2 q_2^2 + Dr_3 q_3^2 - 3Gr - (P_e - P_{prod.})$
2	DF_2 $+ Dr_2$	$R_{perf2} + NDF_2$ $+ Ac_2$	$F_2(q_{tot} - q_3)^2 + F_3(q_{tot})^2 + Ac_3 q_3 + Dr_3 q_3^2 - 2Gr$
3	DF_3 $+ Dr_3$	$R_{perf3} + NDF_3$ $+ Ac_3$	$F_3(q_{tot})^2 - (P_e - P_{Prod}) - Gr$

The obtained influxes then are converted to the mass flow rates using corresponding brine densities at the each node:

$$\dot{m}_{(i)} = q_{(i)} \rho_{(i)} \quad (5.10)$$

The first guess of total flow rate is assumed by the user. Then computer code calculates flow rate distribution along the pipe and well flowing pressures at each node, according to the pressure drops in the pipe and the reservoir.

Pressure development inside of the injection pipe is developed in opposite order than in production side. There is no heat exchanger here, therefore, the friction pressure drop is lower comparing with the production side, and the well flowing pressure values at each node are expected to be very close to each other.

5.2.2 Reservoir Side Pressure Distribution

The reservoir drainage area was assumed to have an elliptical shape (Joshi, 1998). This is the first term in the bracket of the equation 5.11 and defines x-y plane flow into the well. According to (Giger, 1985) the second term represents the z-x plane flow into the well with Muskat's solution for anisotropic porous medium (Cho H. et al., 2001).

$$P_{res} - P_{wf} = R_1 \dot{m}_{reservoir} = \frac{\mu B_{br.} \left[ln(X) + \frac{h\beta}{L} ln\left(\frac{2\beta}{1+\beta} \frac{h}{2\pi r_w} \right) + S \right]}{2\pi k_c h \rho_{br.}} \dot{m}_{br.} \tag{5.11}$$

where L is production or injection interval length, and S is a perforations skin factor (Bellarby, 2009). Parameter X depends on shape of drainage area and with assumption of drainage ellipse semi major axis is greater than producer length $(a > L)$ can be found from:

$$X = \frac{a + \sqrt{a^2 - \left(\frac{L}{2}\right)^2}}{\frac{L}{2}} \tag{5.12}$$

$$a = \frac{L}{2} \sqrt{0.5 + \sqrt{0.25 + \left(\frac{2r_e}{L}\right)^4}} \tag{5.13}$$

Gravel pack model is described by the following expression (Brown, 1984):

$$\Delta P_{gravel} = DFq^2 + NDFq = \frac{\gamma B_{br.}^2}{A_G^2 \rho_{br.}} \dot{m}_i{}^2 + \frac{\mu_{br.} B_{br.} L_G}{A_G k_G \rho_{br.}} \dot{m}_i \tag{5.14}$$

where $B_{br.}$ is formation volume factor, A_G, L_G are gravel pack area and length, k_G is gravel pack permeability.

$$\gamma = \frac{1.47 * 10^7}{k_G^{0.55}} \tag{5.15}$$

$$A_G = A_{perf} \times (spf) \times L_{perf} \tag{5.16}$$

Pressure change along the pipe for any section (producer, insulation, injector):

$$\Delta P = P_{fric} + P_{accel} \pm P_{gravity} = F\dot{m}_{pipe}^2 + Ac\, \dot{m}_{influx} \pm Gr \tag{5.17}$$

where

$$F = \frac{f_{total}\dot{m}_{br.}^{2}.\Delta L_{ins.}}{2A_{pipe}{}^{2}\rho_{br.}D_{h}} \tag{5.18}$$

$$Ac = \frac{\dot{m}_{pipe}}{A_{pipe}A_{influx}\,\rho} \tag{5.19}$$

$$Gr = \rho_{br.}g\Delta L sin(\alpha) \tag{5.20}$$

where for flow in the annulus:

$$A_{ann.} = \frac{\pi\left(D_{o}^{2} - D_{i}^{2}\right)}{4} \tag{5.21}$$

An influx area in a case of perforated wall can be defined as:

$$A_{perf} = \frac{\pi D_{perf}^{2}\;spf\;\Delta l}{4} \tag{5.22}$$

Friction factor was calculated from Asheim (1992) as a sum of friction factors at the wall (f_{wall}) and perforated section of the pipe (f_{perf}):

$$f_{tot} = f_{wall} + f_{perf} = 0.16Re^{0.19} + 4D_{h}\frac{\dot{m}_{influx}}{\dot{m}} \tag{5.23}$$

For the insulated section $D_h = D_o$; $f_{tot} = f_{wall}$; $Ac = 0$.

5.3 Heat Transfer in the Downhole Heat Exchanger

The condensed secondary working fluid is pumped in the DHE and moves vertically downward and reaching reservoir depth horizontally inside the insulated tubing. Afterwards, the flow changes direction to the opposite entering the Annulus1 (see Figure 5.2). The Annuluses 1 and 2 represent heat interaction boundaries of two independent loops: brine and working fluid. Heat is transferred by conduction-convection mechanism to the cold secondary *w.f.* through the annulus 1 pipe thickness.

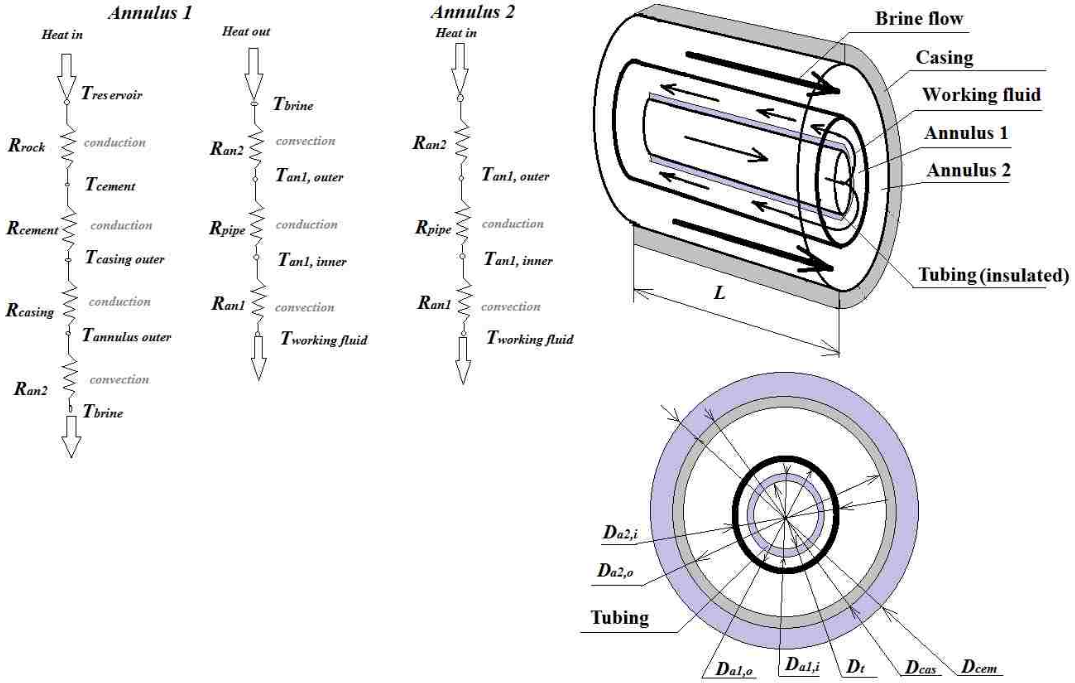

Figure 5.2: Heat exchanger cross sectional view and thermal resistances chart.

Assumptions:

- Steady-state conditions with constant reservoir temperature
- Perfectly insulated tubing
- Constant properties of the fluids within the intervals
- Fully developed flow conditions for brine and working liquid.

The horizontal offset was divided into several intervals and the thermodynamic and fluid properties were calculated from NIST fluid properties solver as imbedded function REFPROP. Heat transfer process was analyzed referring to (Feng, 2012).

Insulated tubing:

$$T_{tubing.} = T_{cond.out} + \Delta T_{w.f.pump.} \tag{5.24}$$

Annulus 1:

$$Cp_{an1}\dot{m}_{an1}\frac{dT_{an1}}{dx} = \frac{T_{an2} - T_{an1}}{R_{a2/a1}} \tag{5.25}$$

Annulus 2:

$$Cp_{an2}\dot{m}_{a2}\frac{dT_{a2}}{dx} = \frac{T_{res} - T_{an2}}{R_{res/a2}} - \frac{T_{an2} - T_{an1}}{R_{a1/a2}} \tag{5.26}$$

where, $C_{p,an1}, C_{p,an2}$ are specific heats of the liquid flowing through the annuluses 1 and 2 respectively; $\dot{m}_{a1}, \dot{m}_{a2}, \dot{m}_t$ - are mass flow rates through annuluses 1, 2, and tubing respectively; T_{an1}, T_{an2} , T_t – are fluid temperatures in the annuluses 1, 2, and tubing respectively; x – is the present value of the heat exchanger length. Minimum $x = 0$, and maximum $x = L$; $R_{res/a2}, R_{a2/a1}$ - are thermal resistances between reservoir and annulus 2, and annulus 2 and 1. Thermal resistances are defined according to (Incopera, 1990).

Boundary conditions:

$$x = 0; \quad T_{an1} = T_t; \quad T_{an2} = T_{res} \tag{5.27}$$

The working fluid temperature flowing in the Annulus 1 is obtained from:

$$T_{(j+1)w.f} = T_{(j)w.f.} + \Delta L \frac{U_{(i)}(T_{(j)} + T_{0(j)})_{w.f.}}{\dot{m}_{w.f.(j)}Cp_{w.f.(j)}} \tag{5.28}$$

The brine temperature flowing in the Annulus 2:

$$T_{(i+1)br.} = T_{(i)br.} - \Delta L \frac{U_{(i)}\left(T_{(i)} - T_{0(i)}\right)_{br.}}{\dot{m}_{br.(i)}Cp_{b(i)}} \tag{5.29}$$

The brine temperature is updated at each node according to calculated influx:

$$T_{(new)br.} = T_{(old)br.} + \frac{\dot{m}_{b(i)}}{\dot{m}_{b(sum)}} T_{(R)br.} \tag{5.30}$$

The main interest of the work is designing a compact and efficient heat exchanger. The diameters are already specified, so the length is the only value to play with:

$$L_{DHE} = \frac{(\dot{m}Cp)_{brine}(T_{in} - T_{out})_{brine}}{R_{an2/a1}\pi D_{an2,i}\,\Delta T_{lm}} \tag{5.31}$$

The main thermal resistances used in the simulation are shown in the Table 5.2. Assigning the DHE length, total brine mass flow rate, and input reservoir and *w.f.* temperatures the computer code calculates the leaving temperatures of the *w.f.* and brine. The w.f. leaving DHE has the closest temperature to the reservoir brine and the difference is a pinch point (PP) temperature. For this project a PP temperature was assumed 5°C.

Table 5.2: Thermal resistances description (Incopera, 1990)

Name and description	Mathematical equation
Thermal resistances between reservoir and Annulus 2	$R_{res/a2} = R_{an2,conv} + R_{cas,cond} + R_{cem,cond} + R_{res}$
Brine flow Annulus 2 convective resistance (outer pipe)	$R_{an2,conv} = \frac{1}{\pi D_{an2,o} h_{an2}}$
Cement thickness conduction	$R_{cem,cond} = \frac{ln(\frac{D_{cem}}{D_{cas}})}{2\pi k_{cem}}$
Metal casing conduction	$R_{cas,cond} = \frac{ln\left(\frac{D_{cas}}{D_{an2}}\right)}{2\pi k_{cas}}$
Reservoir heat transfer occurs through the convective and conduction components. As $\boldsymbol{D_{res}}$ is taken the thickness of the reservoir.	$R_{res} = \frac{1}{\frac{1}{R_{res,cond}} + \frac{1}{R_{res,conv}}}$ $R_{res,cond} = \frac{ln(\frac{D_{res}}{D_{cem}})}{2\pi k_{res}}$; $R_{res,conv} = \frac{1}{\pi D_{res} h_{res}}$
Thermal resistance between Annulus 2 and Annulus 1	$R_{an2/a1} = R_{an2,conv} + R_{pipe,cond} + R_{an1,conv}$
Brine flow Annulus 2 convective resistance (inner pipe)	$R_{an2,conv} = \frac{1}{\pi D_{an2,i}\, h_{an2}}$
Conduction resistance of the pipe 1	$R_{pipe1,cond} = \frac{ln(\frac{D_{an2,i}}{D_{an1,o}})}{2\pi k_{pipe}}$
W.f. flow Annulus 1 convective resistance	$R_{an1,conv} = \frac{1}{\pi D_{an1,o} h_{an1}}$

5.4 Power Generation Subsystem

The turbine work was calculated from the computed temperature of the *w.f.* leaving the DHE and corresponding mass flow rate for the particular DHE length. While the hot stream is travelling back to the surface, the pressure is reduced under the influence of gravity and frictional losses. The travel path was divided in to several intervals where the thermodynamic properties of working fluid were evaluated. There is an enthalpy gain at this interval is due to pressure drop at constant temperature.

Heat gained from the DHE is spent on energy production in the turbine stage, driving both brine and *w.f.* pumps, and rejected to the ambient air including fan power:

$$\left(\dot{Q}\right)_{DHE} = \left(\dot{W}\right)_{Turb.} + \left(\dot{Q}\right)_{HR} + \left(\dot{W}\right)_{w.f.pump.} + \left(\dot{W}\right)_{br.pump.} \tag{5.32}$$

The turbine work portion includes net power produced with account for the energy losses in the turbine, generator and transport gear box.

$$\left(\dot{W}\right)_{Turb.} = \frac{\left(\dot{W}\right)_{NET.}}{\eta_{turb.}\eta_{gen.}\eta_{mech.}} \tag{5.33}$$

From the equations 5.38 and 5.39:

$$\left(\dot{W}\right)_{NET.} = \eta_{turb.}\eta_{gen.}\eta_{mech.}\left[\left(\dot{Q}\right)_{DHE} - \left(\dot{Q}\right)_{HR} - \left(\dot{W}\right)_{w.f.pump.}\right] - \left(\dot{W}\right)_{br.pump.} \tag{5.34}$$

Pump work for working fluid is obtained from:

$$\left(\dot{W}\right)_{w.f.pump.} = \frac{\Delta P_{wf.}\dot{m}_{wf}}{\rho_{wf.cold}} \tag{5.35}$$

The density $\rho_{wf.cold}$ in the equation 5.41 is marked as a cold stream because the *w.f.* pump is installed in the cold stream of the power cycle. Neglecting pressure drop in the condenser and the DHE due to their short length comparing with the vertical well the $\Delta P_{wf.}$ term has two components and calculated at each interval step:

$$\Delta P_{wf.} = \Delta P_{gravity} + \Delta P_{frict.} \tag{5.36}$$

5.5 Heat Rejection Subsystem

Heat rejection subsystem is assumed to be in steady state condition and the ambient temperature is constant and equal to 25℃.

$$(\dot{Q})_{Rej.} = \dot{m}_{wf}(h_{in} - h_{out})_{cond.} + \dot{W}_{condenser\ fan} \tag{5.37}$$

The two phase region occurs in the condenser stage, therefore, rejected amount of heat is calculated with condenser analysis shown below and at constant averaged ambient temperature. The rejected heat is changing with flow rates and weather conditions.

5.6 Analysis

5.6.1 Input Data, Solution Algorithm and Validation

Simulation was performed using the Matlab Simulink software. The calculation algorithm is presented in the Figure 5.3. The geometric values of DHE design and horizontal well are presented in the Table 5.3.

Table 5.3: Horizontal well data for 9 5/8 inch OD

Name	Production side 100m (304.8 ft)
Perforations	1 inch perforations with 20 shots per foot. Perforation length – 100m (304.8ft)
Gravel Pack	20/40 size sand with 135D permeability
Screen pipe	4.88 inch ID screen pipe
	Circular pipe 8.031 inch ID with interval 100m (304.8ft)
	Injection side 100m (304.8 ft)
	1 inch perforations with 12 shots per foot

Firstly, the code reads input data and the user defines input total brine and *w.f.* mass flow rates. The code calculates pressure drops at the each node and corresponding influxes (outflows). The check point is used to verify how well the assumed flow rates at the each node correspond to the assumed values. If necessary the algorithm starts again until the error would not reach less than 1%. The next step is to evaluate heat transfer problem. For the assumed DHE length and w.f. mass flow rate the thermal resistances are computed and Pinch Point temperature difference (PP) is defined. If necessary, a new iteration is performed until the PP temperature will not reach 5°C.

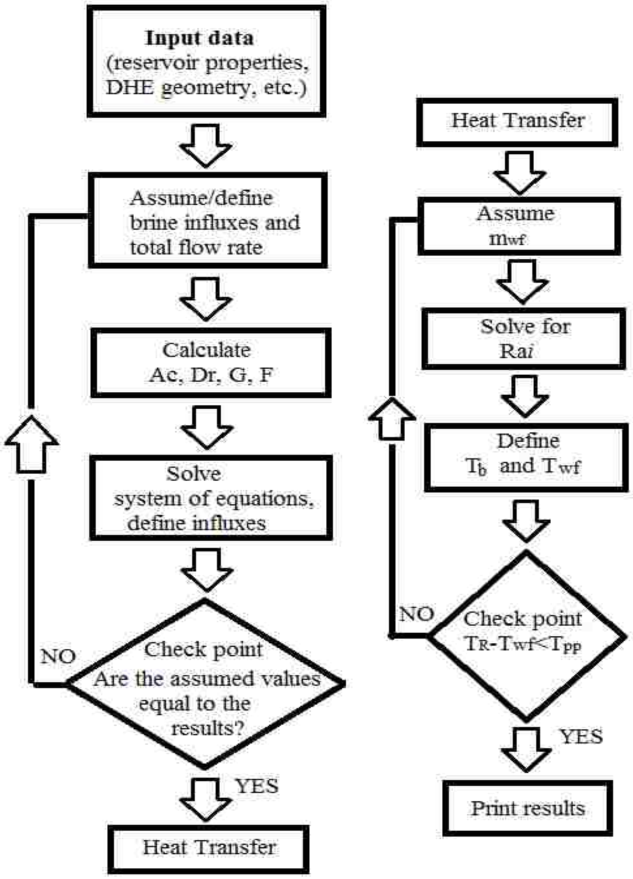

Figure 5.3: Simulation algorithm.

The algorithm was tested with literature data. First, the horizontal well pressure performance was verified with Ouyang et al. (1997), who experimentally defined pressure distribution along a well. Figure 5.4 illustrates comparison of this project code simulation results with Ouyang et al. (1997) in terms of pressure development inside of the horizontal well.

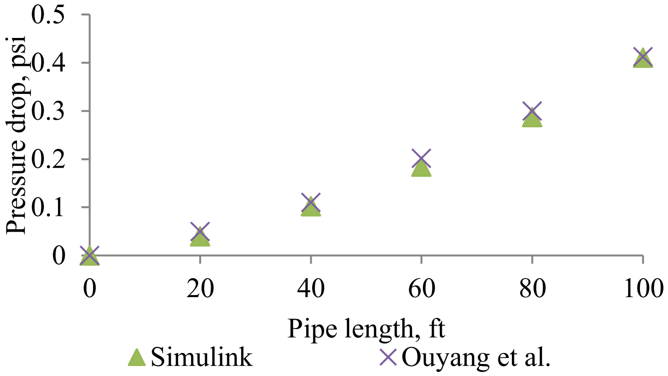

Figure 5.4: Verification with (Ouyang et al. 1997).

Then, heat transfer algorithm was tested with n-Butane working fluid and verified with (Feng, 2012). Figure 5.5 shows good match of this project code simulation with (Feng, 2012) results.

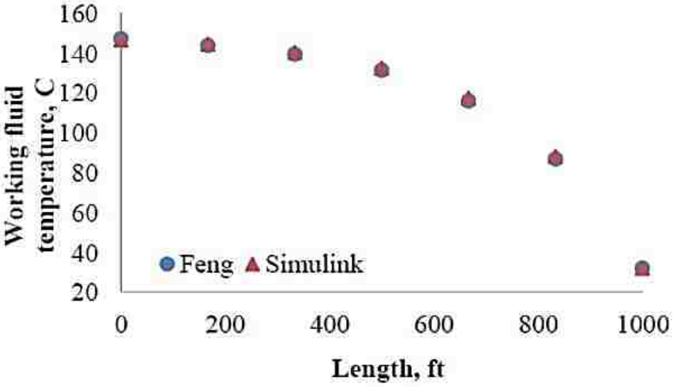

Figure 5.5: Verification with (Feng, 2010).

5.6.2 Case 1: Unequal Influx along the Well

The Heel-Toe effect is a result of the friction pressure drop causing a variable drawdown along the well (Ellis et al., 2009). The result of this effect is unequal influx into the horizontal well, which is greater at the toe, or in our case, where the pump is located. The production side was simulated in order to understand the influx distribution along the well. Figure 5.6 illustrates the results for various well lengths with constant pump drawdown pressure. More uniform influx distribution along the well has the shortest pipe of 150m (457ft).

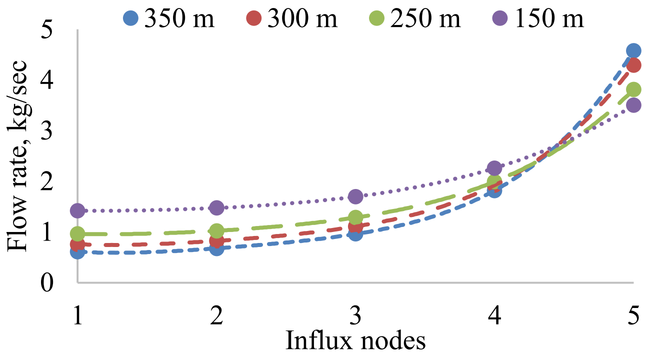

Figure 5.6: Influx chart for 615 psi drawdown.

As it is seen the closest influx to the pump experiences the maximum value. Moving to the heel region the influx is reduced by the impact from the friction pressure drop in the well. Decreasing the production length makes influxes more unevenly distributed. As was expected the frictional and reservoir pressure drops are the most valuable losses in the system (Figure 5.7). Corresponding flow rate is 4842 Bbl/day.

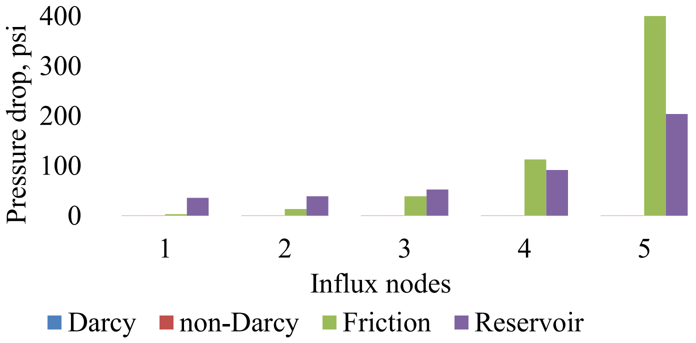

Figure 5.7: Perforated well pressure losses at 615 psi drawdown

5.6.3 Case 2: Equal Influx along the Well

The non-uniform influx in the production zone is caused by the high frictional pressure drops from the DHE installed into the horizontal well section. The influx maximum then is located at the end of the perforated zone, which may cause the gravel pack destruction, DHE erosion and limit the useful length of the horizontal section and shorten productive well life (Ratterman, 2013). Moreover, the non-uniform influx affects negatively the temperature profile of the DHE. The last but not the least reason to avoid the non-uniform influx is the increase in length between the production and injection sections, which affects the drilling cost of the deviated section and installation cost of power unit.

To avoid these complications in the oil industry the equalizer uniform inflow control system is used with integrated velocity flow regulator, or inflow control device (ICD) (Baker Hughes catalog, 2009). The ICD incorporates up to three helical flow channels that can be modified for a variety of downhole flow conditions. The helical channels spin the flow before it enters the wellbore, imposing pressure distribution along the entire lateral length and controlling production rate as a function of both the average drawdown pressure and the average productivity of the well. In reservoirs that require sand control at some point during their productive life, the ICD reduces annular fluid flow velocity and optimizes the inflow velocity into each screen joint.

Figure 5.8 Shows, the brine and *w.f.* temperature distribution along the production side. The node #1 is the closest to the pump location and represents brine temperature leaving the DHE and cold *w.f.* starting point to flow in the Annulus 1.

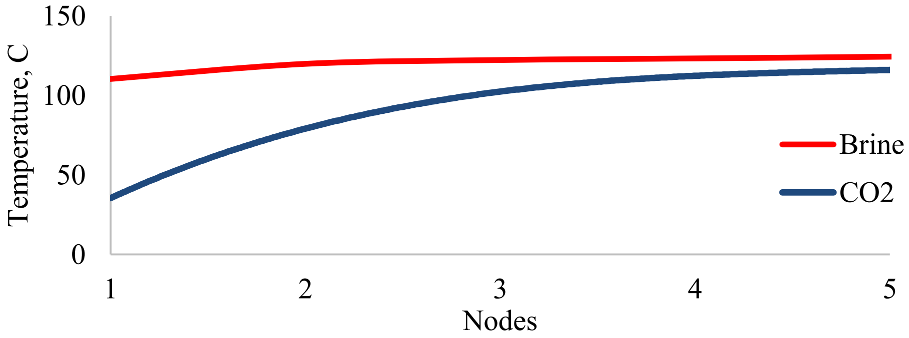

Figure 5.8: CO_2 and brine temperature changes along the DHE length.
Brine temperature leaving the DHE is 110.6C; Length of DHE is 100m.

For different lengths of production side the plot in the Figure 5.9 illustrates relationship between brine and working fluid flow rate changes. The brine temperature leaving the DHE was kept constant and equal to 120.1°C, and reservoir permeability of 12 mD was assumed for reservoir pressure drop calculations (Reference reservoir data). As it is seen increase in the length gives more linear relationship of two flow rates.

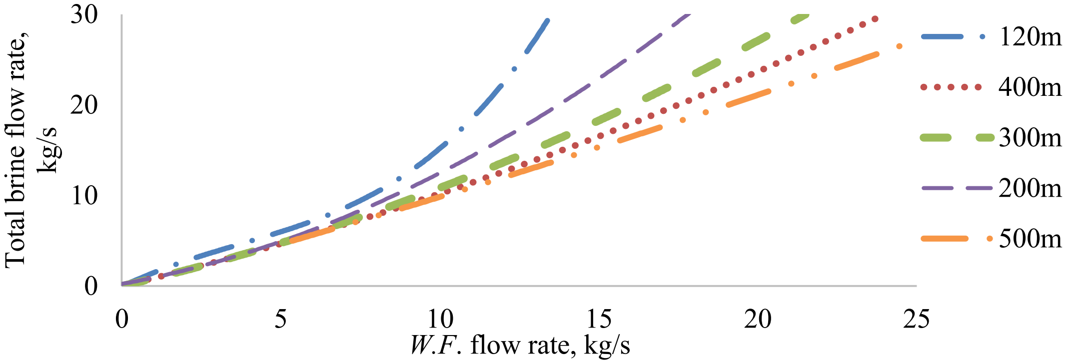

Figure 5.9: Brine and *w.f.* flow rates change for different well lengths.

The net power production of the whole system is proportional to *w.f.* mass flow rate and w.f. temperature leaving the DHE. Raising the w.f. flow rate while keeping maximum possible w.f. temperature leaving the DHE requires expanding the heat transfer area. This can be reached only by adjusting the DHE length in our case. However, brine flowing through long DHE length experiences frictional losses, which affects the net power production. As is seen from the Figures 5.10, and 5.11 the maximum value of net power reaches 153 kW only at 10 kg/s brine flow rate and 8.4 kg/s w.f. flow rate for the reference reservoir case.

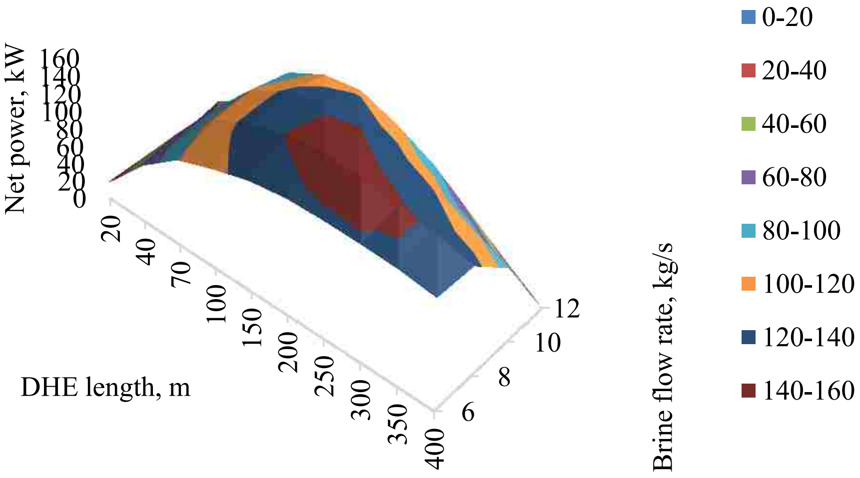

Figure 5.10: Net power development for various DHE lengths.

As it is seen from the Figure 5.11 there is an optimal flow rate interval for each DHE length. The shorter the well, then the maximum net power value is shifted to the right and has wider flow rate interval with small power change. Figure 5.11 has the 200m producer as the minimum length. Further reduction leads to drastic decrease in power due to smaller heat exchange area.

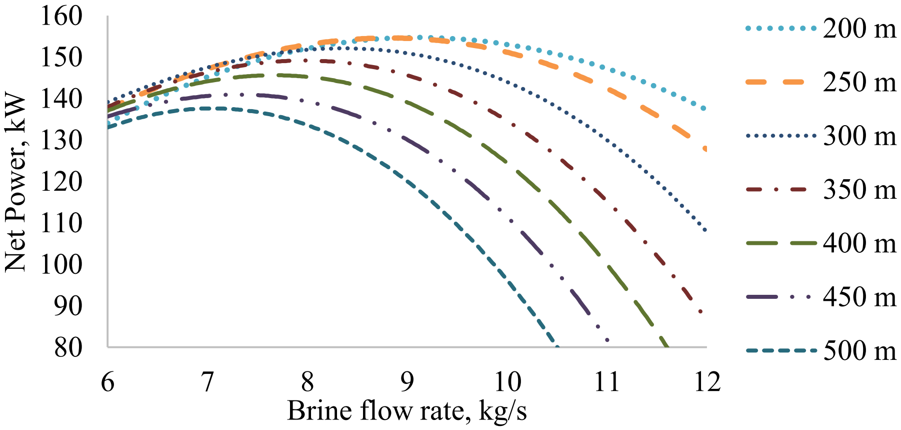

Figure 5.11: Net power development.

Figure 5.12 illustrates the optimization of the producer length. As it is seen, the 8 kg/s brine flow rate is the most productive case at 200 m DHE length.

flow rate is the most productive case at 200 m DHE length.

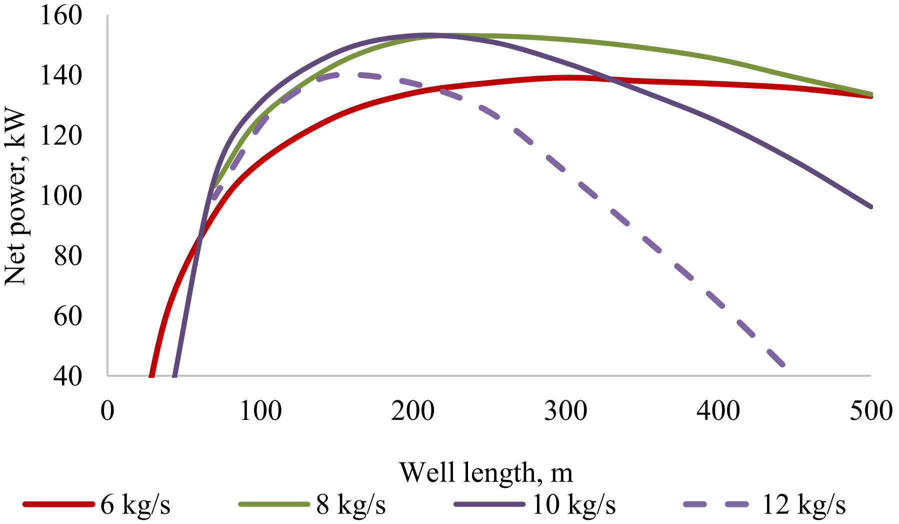

Figure 5.12: Net power vs DHE length. Partially perforated case.

5.6.4 Case 3: Partially Perforated Well

The well length can be perforated fully or partially as shown in the Figure 5.13. In both cases the 8 kg/s brine flow rate is the most power productive rate..

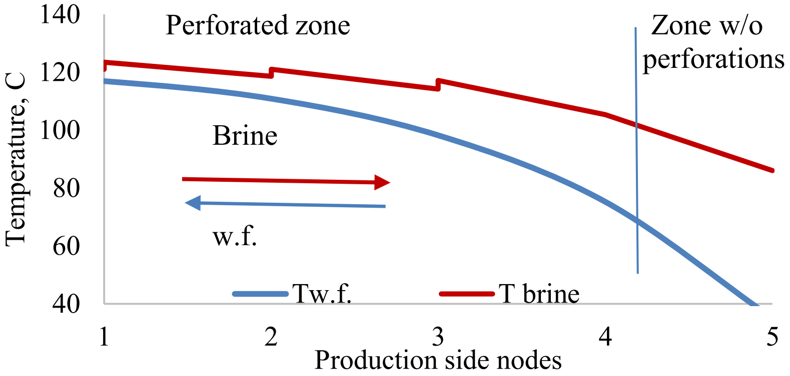

Figure 5.13: Equal influx temperature development.
In this case the well has only 4/5 length perforated.

The DHE is located along the production line and have a uniform brine influx. If no perforation zone is at the beginning of the well, an additional turbulence zone is created, which requires additional power to drive (Figure 5.14 a). To avoid this the perforated interval is better to make at the beginning of the DHE length (Figure 5.14 b).

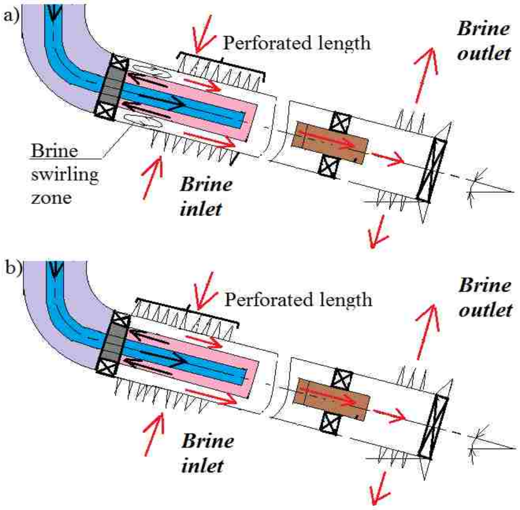

Figure 5.14: Two cases of partially perforation of production side.
a) Perforations shifted to the end of DHE
b) Perforations shifted to the beginning of DHE

In the case of partially perforated producer (Figure 5.14 b) the brine temperature drops at the outlet of the DHE more than in the case of a fully perforated production side with the same well length (see Figure 5.15). The fully perforated well delivers maximum net power due to higher volume of hot brine entering to the system. The simulated well length is 300m, brine/*w.f.* mass flow rates are: 12kg/s and 11.3 kg/s respectively.

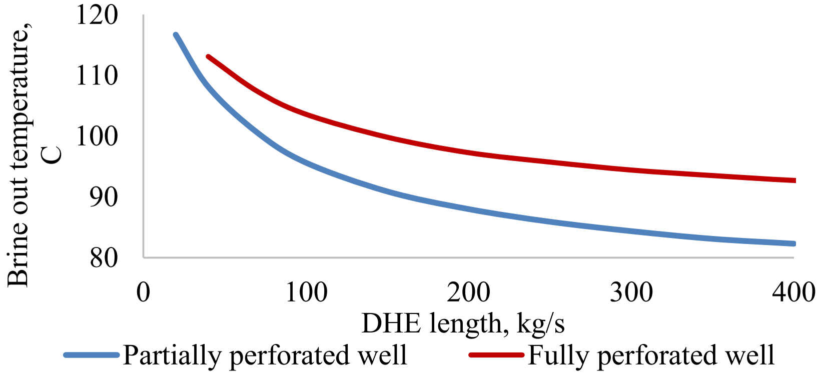

Figure 5.15: Brine temperature leaving the DHE at 8 kg/s brine flow rate.

Net power drops due to lower temperature of the *w.f.* leaving the DHE in case of partially perforated well (see Figure 5.16). The excessive brine temperature drop should be avoided because it cools the reservoir faster than in the case of fully perforated case.

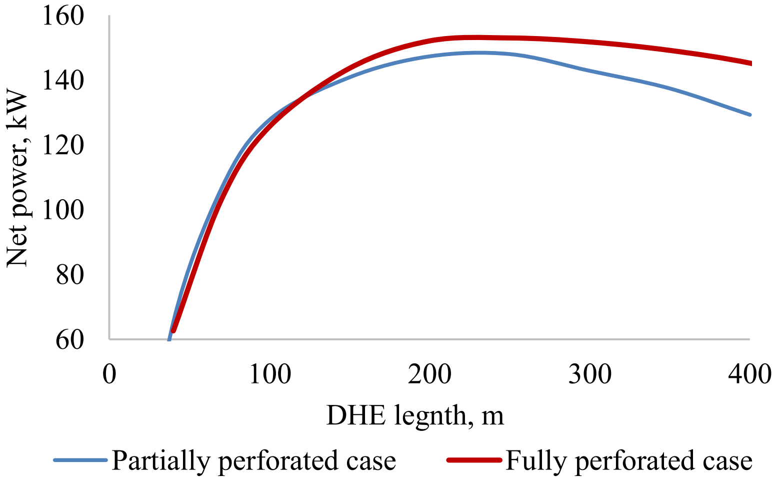

Figure 5.16: Net power development vs DHE length with different perforated cases.

5.6.5 Case 4: Permeability Change

Small values of permeability increase the pressure drop in the reservoir, while losses inside the well remain unchanged. With the same simulation conditions the brine pump has lowest load at the highest permeability, which affects the net power production as indicated in the Figure 5.17.

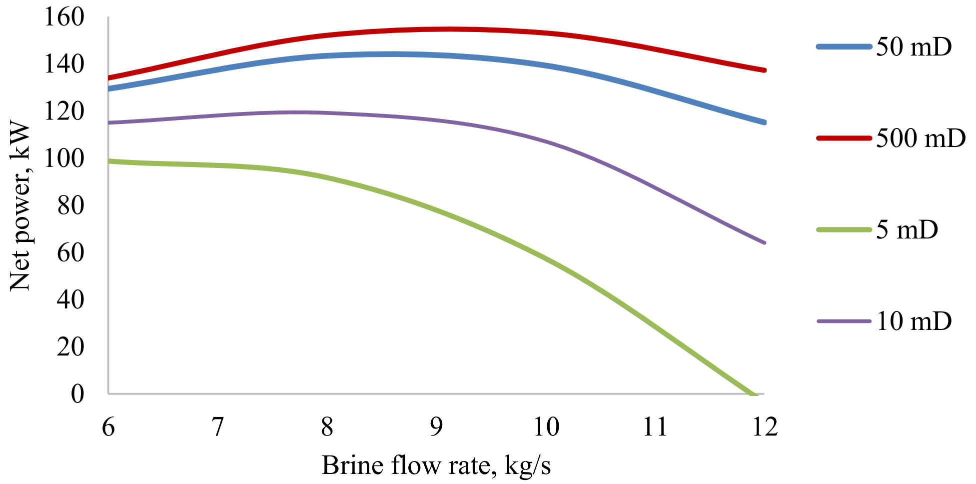

Figure 5.17: Net power change with brine flow rate for changing reservoir permeability.

5.7 Injection Side Pressure distribution

The injection side does not have the DHE inside the well, therefore, the frictional pressure drop is small, and injection length can be short. Figure 5.18 shows the pressure distribution in the injector side at 10 kg/sec total brine flow rate.

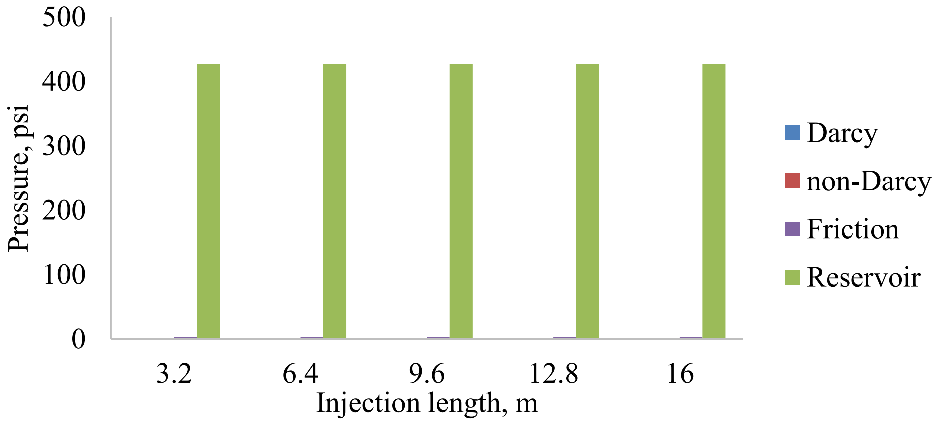

Figure 5.18: Injector side pressure distribution at 419 psi pump head.

According to the pressure balance, 16 meters of injector is enough to run the brine circulation. However, from the practical point of view, longer injection side will reduce the pump head.

5.8 Brine Pump Placement in the Horizontal Well and Effect from Inclination Angle

To determine the brine pump placement let us analyze the pressure distribution in the horizontal well. The production and injection sides mathematically are described by the equations 5.38 and 5.39.

$$\Delta P_{prod.} = \Delta P_{res.prod.} + \Delta P_{\substack{prod.\\compl.}} + \Delta P_{ins.} + \Delta P_{\substack{inj.\\compl.}} \tag{5.38}$$

$$\Delta P_{inj.} = \Delta P_{ins.} + \Delta P_{\substack{inj.\\compl.}} + \Delta P_{res.inj.} \tag{5.39}$$

where $\Delta P_{res.}$ is reservoir pressure drop, while brine is flowing from the injector to the producer; $\Delta P_{\substack{prod.\\compl.}}, \Delta P_{\substack{inj.\\compl.}}$ are pressure drops at both sides of completions (including perforations and gravel pack pressure losses); $\Delta P_{ins.}$ frictional pressure losses at the insulation section of the well.

The order of magnitude of the pressure drops is clear from the Figure 5.19 for 615 psi drawdown and head pressures. The injection side is mostly contain reservoir pressure drop. The production side shares the drawdown between reservoir and friction losses. The circular section of the well has the least significant value, which means the designer can install the brine pump closer to producer or injector depending on easiest way of installation process.

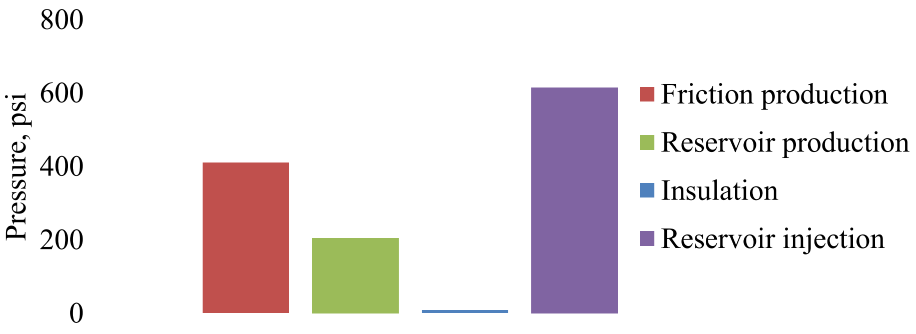

Figure 5.19: Order of magnitude of the main pressure resistances.

The well inclination angle adds additional gravity term to the pressure distribution equations. If the producer is on top and the injector is on the bottom, the gravity term is positive and helps compensate friction inside the DHE. However, the discharge of the cooled brine happens at a higher pressure than at the inlet, which is equal to the gravity. So, the brine pump would need additional head to be able to push brine into the reservoir on the injector side. The other case is when the producer is below the injector. In this case the brine flow inside the DHE would experiencing additional negative gravity term, however, the discharge would happen at the lower pressure than inlet. In both cases the brine pump would have the gravity terms cancelled when calculating the total pressure head.

As soon as the net power development is the main concern of this project the producer is better to install at the higher elevation than injector. The reason for doing that is higher reservoir temperature at the bottom of the reservoir. Then the discharged cold brine would meet hotter environment and the travel time to the producer against gravity would be longer. One more comment is taken from Feng (2012). The cold brine plume, which would occur at the injector during the operating period is heavier than the reservoir brine. Placing injector on top would provoke sliding this plume toward the producer along the insulation length. For these reasons the negative inclination angle was assumed from the producer to the injector.

5.9 Effect from the Ambient Temperature Fluctuations

The power generation subsystem is working at a steady state condition if there is no any change in temperatures of cold and hot sides of the heat flow. Heat gained in heat extraction loop depends on reservoir temperature. Constant reservoir temperature can be managed by increasing the insulation length between producer and injector. The most severe consequences come from the ambient temperature fluctuations that make PC more susceptible to the seasonal and daily changes in weather conditions. The previous discussion assumed a reasonably stable, ambient temperature, which corresponds to the yearly averaged value at the particular geographic location. This statement is not true.

As the ambient temperature increases, especially during summer time, the performance of a power unit significantly reduces (Sohel et al., 2011). The condenser heat load is a function of several factors: *w.f.* inlet condition (temperature and pressure), ambient heat sink temperature, *w.f.* mass flow rate and geometric parameters of the condenser design (area of cooling, fins, etc.). The power unit is usually built to run optimally for a given set of design conditions that takes into account the reservoir and ambient temperature changes. When the ambient air temperature varies, the plant runs under the off-design condition (Varney, J. et al., 2012). To model these off-design condition the ambient air temperature is a variable but other unit's parameters were kept with the following assumptions:

- The working fluid pump and brine pump power consumption is independent of ambient temperature fluctuations. Therefore, the mass flow rates stay constant.
- Condenser area is constant.
- In case of ambient air temperature is greater than the design ambient air temperature (25C), the turbine back-pressure is increased to ensure that the working fluid is in a liquid stage. Node#1 is kept at constant entropy for all pressures above the design pressure (see Figure 4.19). This requirement is explained by the necessity to have liquid stage at the *w.f.* pump.
- If the actual ambient temperature is lower than the design ambient temperature, then the turbine backpressure is dropped according to saturated line of the CO_2 fluid.

The air temperature change causes condenser *w.f.* temperature-pressure variations. As the temperature drops, then pressure at the condenser drops, and therefore, the outlet of the turbine stage changes as well. The bottom line of the T-S plot is dropped to the lower temperature design temperature and therefore the liquid saturation pressure is dropped. The expander produces more energy and, consequently, more energy is required for rejection through the condenser. At the same time the condenser area is constant as well as *w.f.* flow rate. So, the only choice to increase heat rejection is increasing the fan speed, which requires some additional energy.

$$\dot{Q}_{Rej.} = \left(\frac{1}{\frac{1}{h_{wf}} + \frac{1}{h_{air}}}\right) \frac{L_{tubes}\pi D_{tubes}\eta_{cond.}}{\dot{m}_{air}\Delta P_{cond.}} (\Delta T_{lm.cond})\dot{W}_{fan} \qquad (2.7)$$

Increase in air temperature provoke some shift in T-S diagram that reduces the useful work area. Figure 5.20 shows the condenser (blue line) and DHE (red line) pressures change with ambient temperature growth. As it is seen the slope of both lines increases drastically at high ambient temperature values.

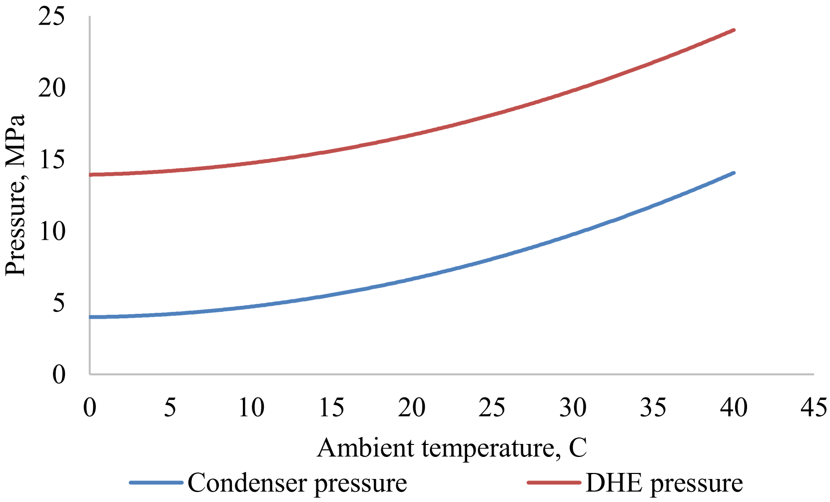

Figure 5.20: Condenser and DHE pressure variations caused by air temperature change.

The ambient temperature progress affects the *w.f.* temperature development in the DHE. Hotter *w.f.* is entering the heat exchanger as well as leaving the DHE. Figure 5.21 illustrates the point. Higher temperature of the *w.f.* has higher enthalpy, however, high ambient temperature reduces the enthalpy difference in the turbine stage and the net power as well.

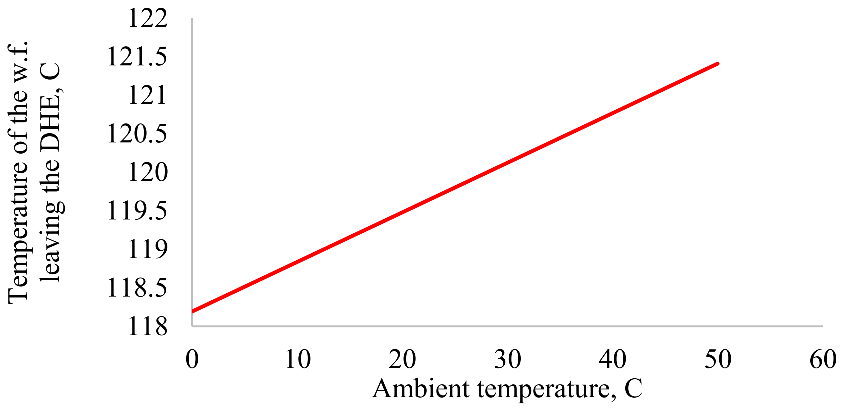

Figure 5.21: *W.f.* temperature development at the exit of the DHE.

With increasing the ambient air temperature the gained heat from the reservoir is reduced, so does the heat rejection. Efficiency drops drastically after ambient temperature reaches *w.f.*'s critical point (Figure 5.22).

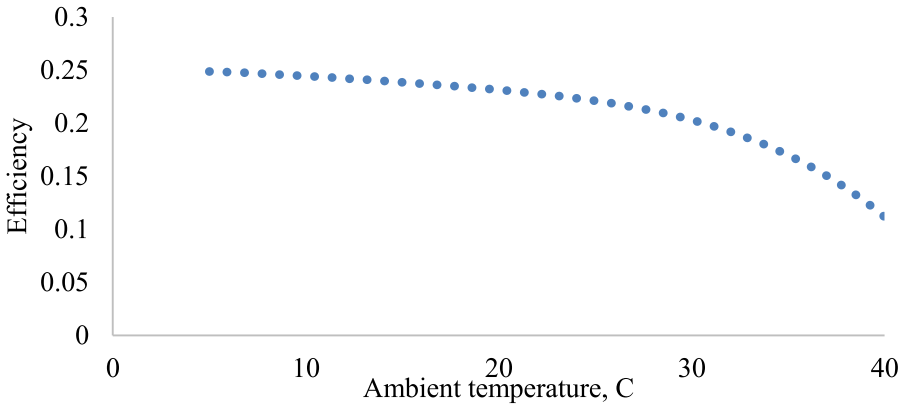

Figure 5.22: Efficiency change with ambient temperature.

The net power increases with ambient temperature reduction. There is more heat gained from the reservoir (Figure 5.23).

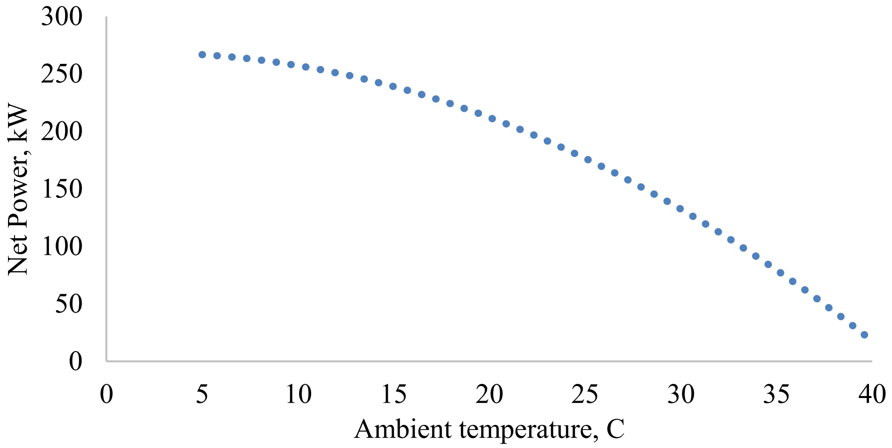

Figure 5.23: Net power change with ambient temperature.

At the same time the cooled brine temperature drops with ambient temperature reduction (Figure 5.24).

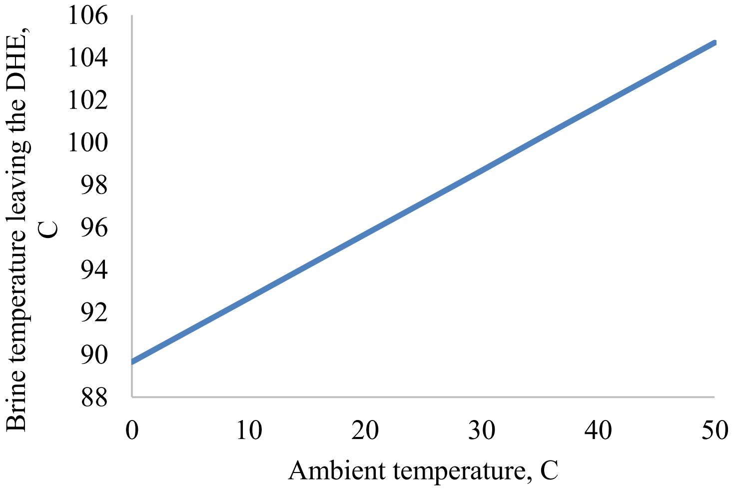

Figure 5.24: Temperature change of the brine leaving the DHE.

Figure 5.25 shows simulation results of the system using different working fluids with reference reservoir data. As it is seen the turbine power production increases with turbine inlet temperature, or rising reservoir temperature. The maximum power value production belongs to carbon dioxide *w.f.* for all temperature range.

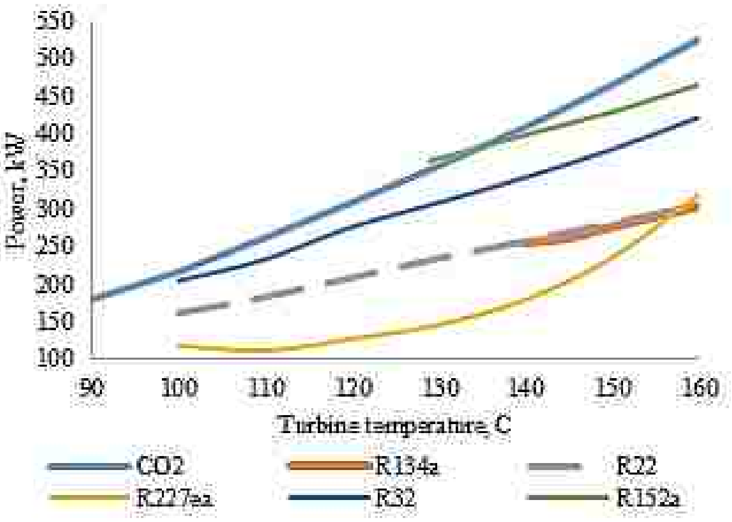

Figure 5.25: Different w.f. application to the reference reservoir data.

5.10 Conclusions

- The design of DHE is affecting the power cycle performance. The maximum net power value was obtained with well located in the reservoir with the highest permeability, reservoir temperature, and lowest possible ambient temperature.
- The friction losses in the DHE are affecting power spent on brine pump. Thus, there is an optimal DHE length for the particular *w.f.* and brine mass flow rates and temperatures of the reservoir. Using the DHE with higher length increases pressure losses in the horizontal well and, therefore, increases brine pump power requirement and reduces net power production. The DHE length reduction as well as perforated length leads to reduction of net power due to small heat transfer area for the chosen mass flow rates.
- The scheme using a tool such as the Baker-Hughes ICD in the completion is more preferable due to equalizing the influx into the well. This rearranges the heat transfer in such way that it is possible to increase the *w.f.* mass flow rate having the same total brine mass flow rate.
- The reduction of the perforated length is reducing the brine temperature leaving the horizontal well.

CHAPTER 6: THERMAL BREAKTHROUGH TIME

"Essentially, all models are wrong, but some are useful"
George E. P. Box

The purpose of this chapter is to analyze fluid flow residence time from the injection to the production sides. If cooled brine enters the production side during an operational lifetime it will negatively affect the energy production. Thus, it is primary interest to make sure that the breakthrough time of the system is less than the typically assumed thirty years of overall operational period.

6.1 Literature Review

The vertical extraction–injection well pairs have been successfully studied in several projects, such as: contaminated groundwater remediation, geothermal and heat pump applications, and tracer tests (Grove and Beetem, 1971; Welty and Gelhar, 1994). In all these cases, the recirculation zones are created in between the wells. Prediction of the fluid residence time (FRT), which is the time to travel from the injection to the extraction well, have great influence in the well placement location.

Generally, two methods are used to evaluate FRT in the recirculation zone (Luo et al., 2004). The average FRT can be directly provided with the known zone volume and the recirculation flow rate. However, the exact reservoir volume is hard to predict. The other commonly used method is streamline tracing, when numerous particles are released at the injection-well boundary and move with the local seepage velocity until they reach the extraction well. The ensemble of all particle travel times yields the breakthrough curve at the extraction well (Zheng and Bennett, 2002). Muskat (1936) determined the shape and position of a tracer front and the first breakthrough time for injected water reaching an extraction well. The regional flow was ignored. All the approaches were derived from potential flow theory.

6.2 Potential Flow Theory

The potential flow model was applied to solve pressure distribution and determine velocity streamlines between two horizontal wells placed in series in the aqueous reservoir. Assumptions are: steady-state, continuous, incompressible, inviscid, irrotational, two-dimensional flow which occurs within homogeneous, isotropic layers of a confined aquifer. Potential flow describes the velocity field as the gradient of a scalar function $\nabla\Phi$:

$$V = -\frac{K}{\mu}\nabla\Phi \tag{6.1}$$

For the incompressible flow case:

$$\nabla * V = 0 \tag{6.2}$$

then:

$$\nabla * \nabla\Phi = \nabla^2\Phi = 0 \tag{6.3}$$

which is a Laplace equation.

The solution of equation 6.3 was derived in several literature sources and for different cases: source/sink, well doublet, etc. (Strack, 1989). First, let us solve the equation 6.3 for a single sink and source pair in an infinite medium. From the continuity equation the same amount of flow must pass through the sphere or a radius *r*. Then, the first integral of equation 6.3 is equal to:

$$q = 2\pi r\frac{d\Phi}{dr} \tag{6.4}$$

And the second integration yields:

$$\Phi = \frac{q}{2\pi}\ln\frac{r}{R} + \Phi_0 \tag{6.5}$$

where Φ_0 is a potential at the location R far from the source.

The obtained flow net for a source is illustrated in the Figure 6.1. The streamlines are radial lines emanating from the origin. Each line represents constant value of the stream function. Here, for example, 20 lines are chosen, so the amount of $\Delta\psi_i$ flows through each segment:

$$\Delta\psi_i = \frac{q}{2\pi}\theta = \frac{q}{20} \tag{6.6}$$

The concentric circles surrounding the origin are lines of constant potential. The streamlines cross equipotential lines at right angles (Strack, 1988)

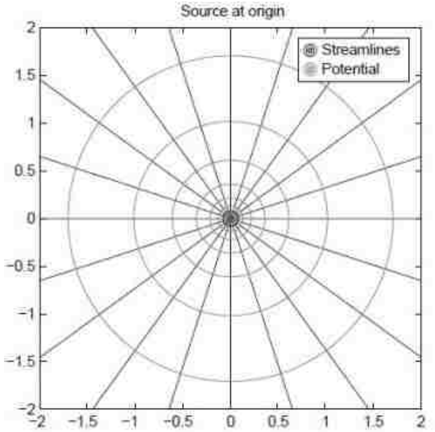

Figure 6.1: Source potentials and streamlines. (After Houghton et al., 2013)

6.2.1 Horizontal Well Streamlines and Equipotential Surfaces

For horizontal well one can derive the similar relation as equation 6.6. The percolation velocity ($V_{perc.}$) through the spherical surface of area $A_{sph.}$ in 3-D space is:

$$V_{perc.} = \frac{q}{A_{sph.}} = \frac{q}{4\pi r^2} \tag{6.7}$$

Following Lu (2012) the total flow rate from the uniform line source is spread along the well with length L:

$$d\Phi = -\frac{q}{4\pi LR}\Delta x \tag{6.8}$$

where

$$R = \sqrt{(x - x_0)^2 + (y - y_0)^2} \tag{6.9}$$

for 2D scheme.

Let us assume the origin location in the middle of the well $c = \frac{L}{2}$, then

$$\Phi = -\frac{q}{4\pi L}\int_{-c}^{c}\frac{dx}{R} \tag{6.10}$$

Then, taking integral receive:

$$\Phi = -\frac{q}{4\pi L} ln\left(\frac{a-c}{a+c}\right) \tag{6.11}$$

where $2a$ is the semi-major axis of pressure drainage elliptical shape.

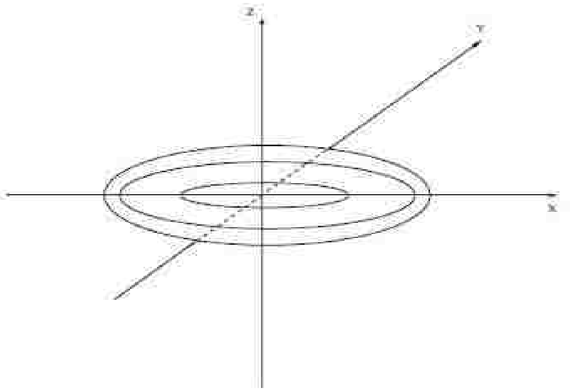

Figure 6.2: Elliptical drainage area of horizontal well (after Lu, 2012).

The streamlines start from each point of the horizontal well and cross the equipotential lines at the right angle. However, in this project one observes two horizontal wells, where the streamlines and equipotentials are combination of both wells at fully developed drainage/discharge area.

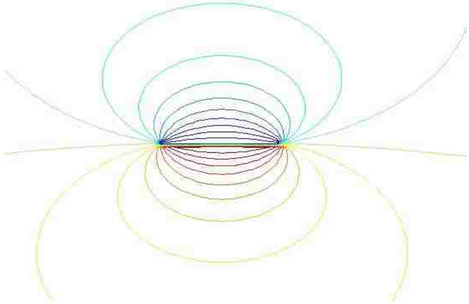

Figure 6.3: Potential flow application. Streamlines for a single sink and a source.

In this section of dissertation the primary interest is to track the flow path from each node of the horizontal well. Therefore, the sink/source equation for potential flow was used and the method of images (Strack, 1988) was applied to reconstruct the horizontal well as a line of sinks (for production side) and a line of sources (for injection side). The outflow of the each sink or source are equal and the total flow rate is equal to the sum of sinks or sources per unit length.

Potentials and streamlines were found from:

$$\Phi = -q_{x0}x + \frac{q}{2\pi}\ln\frac{\sqrt{(x+c_i)^2+y^2}}{\sqrt{(x-c_i)^2+y^2}} + \Phi_0 \tag{6.12}$$

where Q_{x0} is a distributed reservoir geofluid flow rate in case of flowing aquifer $\left[\frac{m^3}{\sec m}\right]$.

$$\psi = \frac{q}{2\pi}(\theta_1 - \theta_2) \tag{6.13}$$

where θ_1, and θ_2 are position angles and determined from (Strack O., 1988).

In this case the flow rate from the node is a multiplication of flow per unit length of the section (production or injection) to the well segment length Δx:

$$q = q_{well}\frac{\Delta x}{L_{well}} \tag{6.14}$$

If one extend the production and injection side by additional sinks and sources, the horizontal well pair will looks like in the Figure 6.4.

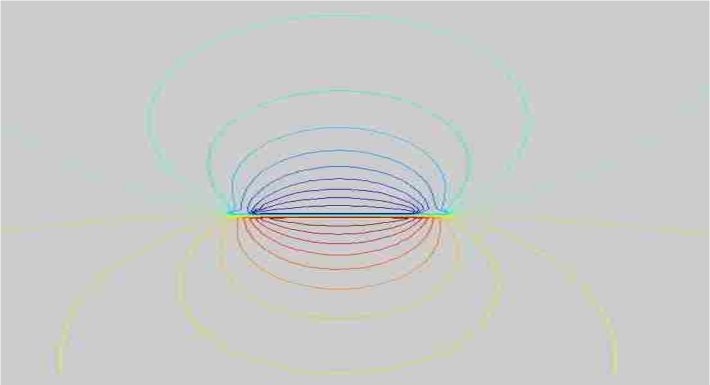

Figure 6.4: Streamlines for several sinks and sources represented horizontal well.

Here no reservoir flow is assumed. Note, that the closest pair nodes production/injection are connected by the streamlines, and so one by the distance from the center. The closest nodes have the shortest interval of geo-fluid to flow. The endpoints have the longest trajectory.

Assuming equal flow rates for both production and injection sides but different lengths the streamlines distribution is shown in the Figure 6.5. Production side has lengthier interval (left), than injection side (right) as shown in the figure below.

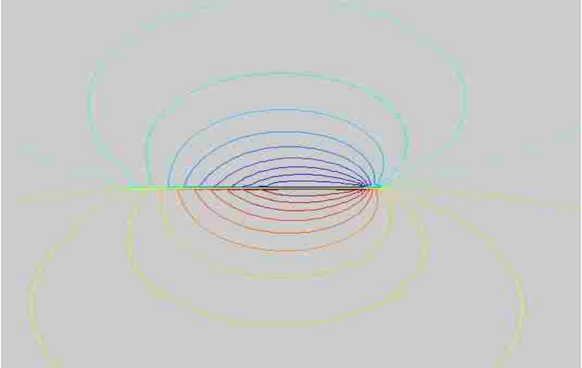

Figure 6.5: Streamlines for horizontal well with production.
Producer in the left is longer than injection side (right).

Adding reservoir flow into the observation one will receive the figure similar to the Reynold's oval (Figure 6.6).

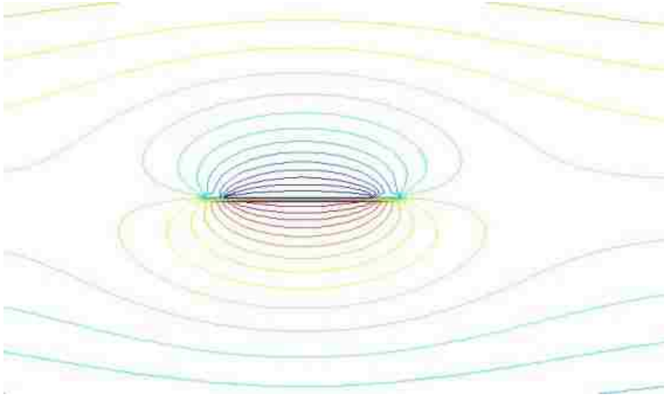

Figure 6.6: Horizontal well in the reservoir flow.
Reservoir streamlines have direction from the left to the right.

Knowing the streamline length, which is a half perimeter of flow path ellipse, starting from the particular pair of nodes we can define the breakthrough time of the system.

6.2.2 Thermal Retardation Factor

Heat is absorbed from the matrix into the geo-fluid when the cooled brine percolates through a hot reservoir rock matrix. Therefore, the velocity front and thermal front have some retardation, which is a function of reservoir properties (porosity), and rock-fluid properties (specific heat, density). Let us derive this parameter starting with energy balance equation (Shook, 2001):

$$\left[\phi\rho_{br.}.C_{p\,br.} + (1-\phi)\rho_{r.}.C_{p\,r.}\right]\frac{\partial T}{\partial t} + \rho_{br.}.C_{p\,br.}.V_{br.}\frac{\partial T}{\partial x} - k_{eff.}\frac{\partial^2 T}{\partial x^2} = 0 \qquad (6.15)$$

Rearranging will receive:

$$\frac{\partial T}{\partial t} = -\frac{\rho_{br.}.C_{p\,br.}.V_{br.}}{\phi\rho_{br.}.C_{p\,br.} + (1-\phi)\rho_{r.}.C_{p\,r.}}\frac{\partial T}{\partial x} + \frac{k_{eff.}}{\phi\rho_{br.}.C_{p\,br.} + (1-\phi)\rho_{r.}.C_{p\,r.}}\frac{\partial^2 T}{\partial x^2} \qquad (6.16)$$

Then,

$$\frac{\partial T}{\partial t}\frac{\partial x}{\partial x} = \frac{\partial T}{\partial x}\frac{\partial x}{\partial t} = -\frac{\rho_{br.}.Cp_{br.}.V_{br.}}{\phi\rho_{br.}.C_{p\,br.} + (1-\phi)\rho_{r.}.Cp_{rock}}\frac{\partial T}{\partial x} + \frac{k_{eff.}}{\phi\rho_{br.}.Cp_{br.} + (1-\phi)\rho_{r.}.Cp_{rock}}\frac{\partial^2 T}{\partial x^2}$$

$$(6.17)$$

From here:

$$\frac{\partial x}{\partial t} = V_{therm.} = \frac{\rho_{br.}.Cp_{br.}.V_{br.}}{\phi\rho_{br.}.Cp_{br.} + (1-\phi)\rho_{r.}.Cp_{rock.}} \qquad (6.18)$$

$$V_{comp.} = -\frac{V_{br.}}{\varphi} \qquad (6.19)$$

$$R_t = \frac{V_{br.}}{V_{therm.}} = \frac{\phi\rho_{br.}.Cp_{br.} + (1-\phi)\rho_{rock.}.Cp_{rock.}}{\phi\rho_{br.}.Cp_{br.}} = 1 + \frac{(1-\phi)\rho_{rock.}.Cp_{rock.}}{\phi\rho_{br.}.Cp_{br.}} \qquad (6.20)$$

Thus, the thermal breakthrough time is delayed by a retardation factor:

$$t_{th} = t_{br.}.R_t \qquad (6.21)$$

The thermal front distance is left behind of fluid flow front at time t:

$$x_{th} = \frac{x_{br.}}{R_t} \qquad (6.22)$$

6.3 Thermal Breakthrough Time

The trajectory path of cold fluid flow $x_{comp.}$ is matching with the streamlines. If a_i and b_i are ellipse semi major and semi minor axes at the *i-th* nodes of each well respectively (Figure 6.7). Thus, the flow occurs from each corresponding node starting from the closest ones.

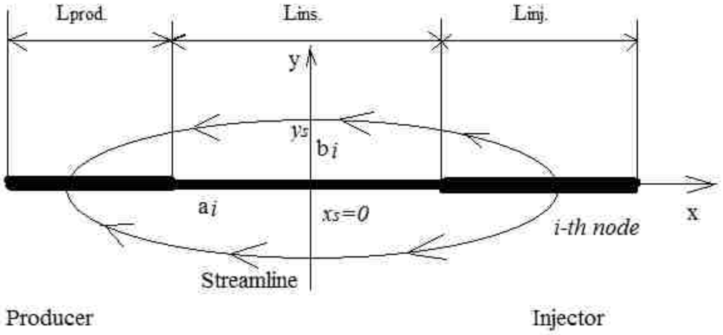

Figure 6.7: Single streamline flow scheme from injector's i-th node to the producer's i-th node.

The cold stream is driven by elliptical path flow which is a half perimeter of ellipse with a_i and b_i are ellipse semi major and semi minor axes, and equal to $x_{br.}$. The location of a_i is defined by the wells placement, but b_i is unknown for now and depends on both: flow rate of the wells, as well as the reservoir flow rate.

The maximum value of b_i corresponds to the stagnation point. Choosing the origin of the system coordinates at the half way between the i-nodes let us find the y_s-coordinate of the stagnation point. Let us take a derivative from equation 6.12:

$$-\frac{\partial \Phi}{\partial x} = q_{x0} - \frac{q}{2\pi}\left(\frac{x_s + c_i}{(x_s + c_i)^2 + {y_s}^2} - \frac{x_s - c_i}{(x_s - c_i)^2 + {y_s}^2}\right) \tag{6.23}$$

From this Eqn. with $x_s = 0$, or at the origin the y_s is equal to:

$$y_s = b_i = \pm\sqrt{\frac{qc_i}{\pi q_{x0}} - {c_i}^2} \tag{6.24}$$

From the obtained formula one can see that the reservoir flow reduces the semi minor axis.

The simplified equation for ellipse perimeter is found from (Haynes, 2014):

$$P_{ellipse} \approx 2\pi\sqrt{\frac{a^2+b^2}{2}} = 2x_{br.} \tag{6.25}$$

Substituting the equation 6.25 into 6.26, and simplifying it with $a = 2c_i$ will have:

$$\frac{P_{ellipse}}{2} = x_{br.} = \frac{\pi}{\sqrt{2}}\sqrt{\frac{qc_i}{\pi q_{x0}} + 3{c_i}^2} \tag{6.27}$$

Then,

$$x_{th} = \frac{\pi}{R_t\sqrt{2}}\sqrt{\frac{qc_i}{\pi q_{x0}} + 3{c_i}^2} \tag{6.28}$$

Combining equations:

$$t_{th} = t_{br.}R_t = \frac{x_{br.}}{V_{br.}}R_t \tag{6.29a}$$

$$t_{th} = \frac{R_t\frac{\pi}{\sqrt{2}}\sqrt{\frac{qc_i}{\pi q_{x0}} + 3{c_i}^2}}{\frac{q_{x0}}{\phi} - \frac{q}{2\pi\phi}\left(\frac{x+c_i}{(x+c_i)^2+y^2} - \frac{x-c_i}{(x-c_i)^2+y^2}\right)} \tag{6.29b}$$

The brine velocity as a constant parameter along the streamline by definition, so from each small segment of the well Δx in the injector the $q\frac{\Delta x}{L}$ portion of flow rate is pumped to the reservoir through the $\pi D\Delta x$ surface area of the well. So:

$$V_{br.} = \frac{q}{\pi D} \tag{6.29c}$$

$$t_{th} = \frac{R_t\frac{\pi}{\sqrt{2}}\sqrt{\frac{qc_i}{\pi q_{x0}} + 3{c_i}^2}}{\frac{q}{\pi D}} \tag{6.29d}$$

From the equation 6.29 is clear, that the thermal breakthrough time (TBT) for two horizontal wells flow is a function of reservoir parameters: porosity, permeability; flow rates of the reservoir and well discharge; and retardation factor, which is a function of geo-fluid and reservoir rock thermal characteristics.

- Special case example

Let us track the TBT for the shortest interval – straight line distance between the wells. Then, the equation 6.29d reduces to:

$$t_{th} = \frac{R_t 2c_i}{\frac{q_{x0}}{\phi} - \frac{q}{2\pi\phi}\left(\frac{1}{x+c_i} - \frac{1}{x-c_i}\right)} \qquad (6.30a)$$

$$t_{th} = \frac{R_t 2c_i}{\frac{q}{2\pi\phi}\left(\frac{c_i}{x^2-{c_i}^2}\right) + \frac{q_{x0}}{\phi}} \qquad (6.30b)$$

which can be further simplified according to (Luo & Kitanidis, 2004)

$$t_{th} = \frac{4\pi\phi R_t {c_i}^2}{3q} \qquad (6.31)$$

The equation 6.31 is the exact formulation of the residence time by (Shook, 2001). For the input data shown in the Table 6.1 some results were obtained and illustrated in the Figures 6.8, 6.9, and 6.10.

Table 6.1: Input data

Parameter	Dimensions	Value
$\boldsymbol{q}$	$\frac{m^3}{sec}$	0.009434
$\boldsymbol{q_{x0}}$	$\frac{m^3}{sec}$	0.00001
$\boldsymbol{c_i}$	m	900
$\boldsymbol{\rho_{r.}}$	$\frac{kg}{m^3}$	2300
$\boldsymbol{C_{p\,r.}}$	$\frac{J}{kg\,K}$	920
$\boldsymbol{\rho_{br.}}$	$\frac{kg}{m^3}$	988
$\boldsymbol{C_{p\,br.}}$	$\frac{J}{kg\,K}$	4080
$\boldsymbol{D}$	m	0.43
$\boldsymbol{L}$	m	250
$\boldsymbol{\phi}$	-	0.1

Retardation factor is 5.72 and TBT for the first cold front arrival is 22.17 years for the input data presented in the Table 6.1.

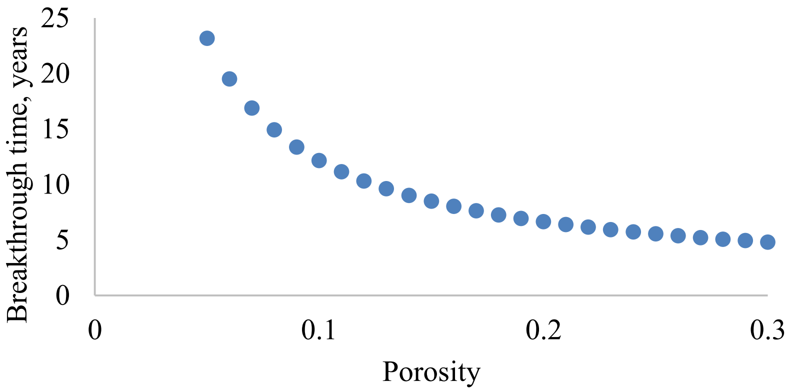

Figure 6.8: Breakthrough time with changing porosity.

The breakthrough time value is increasing with reduction of porosity. Smaller pore size requires more time fluid to travel with the same flow rate. Porosity is affecting the retardation factor as well.

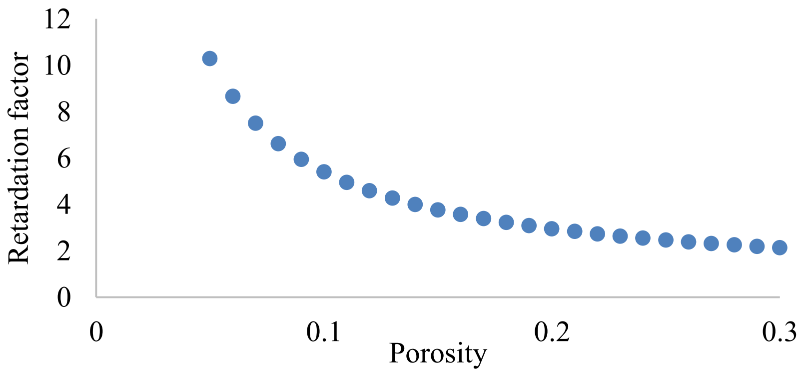

Figure 6.9: Retardation factor calculated by Eqn. (6.20).

Increasing the insulation length increases TBT, as shown in the Figure 6.10. For reference reservoir data and 30 years of operation would require about 800 m of insulation length to avoid cold brine production.

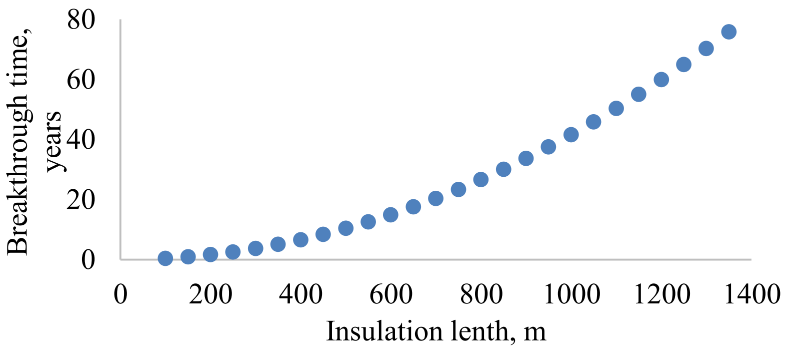

Figure 6.10: Breakthrough time for different insulation length.

6.3.1 Influence of Cold Influx on the Net Power Production

The *w.f.* temperature will not drop dramatically when the cold front will invade the production side. As was discussed before, the influx to the production side is spread along the well. So, the following simulation was performed to see the net power drop relative to percent invasion of cold front along the DHE According to Figure 6.11 the net power drop was simulated for 200m DHE case with 98.67C cooled brine invasion, brine flow rate 10kg/s. The 55 kW maximum net power drop occurs if the cold area occupies the whole DHE length, and only 6kW drop occurs at 10% invasion.

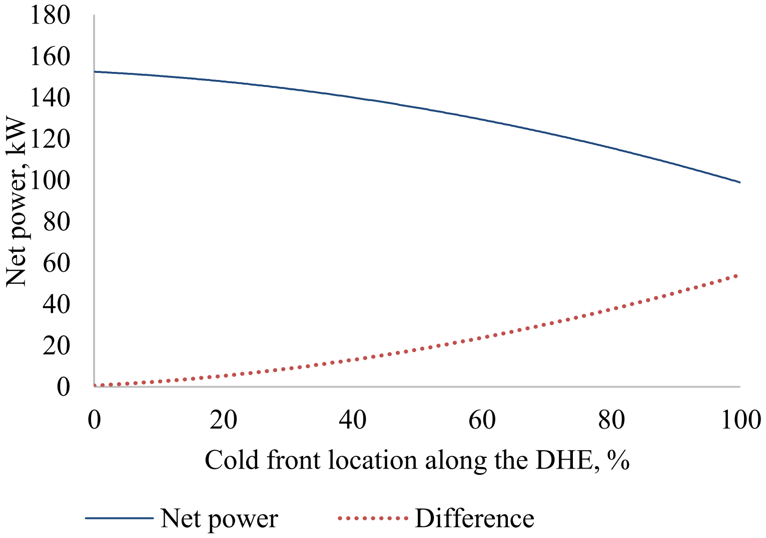

Figure 6.11: Net power drop with respect to cold front movement along the DHE length.

6.4 Conclusions

- The retardation factor plays a major role in thermal breakthrough time determination. Additional factors influencing the TBT are reservoir and well flow rates, and insulation length separating producer and injector. Choosing the reservoir with high porosity would reduce TBT, and thus, this case would require higher length of insulation comparing with lower porous reservoir at the same flow rate.
- When the cold front reaches the production side of the well, the net power will not drop immediately, due to length of the production side and distributed influxes along the well.

CHAPTER 7: THERMO-ECONOMIC ANALYSIS

“There ain't no such thing as a free lunch”
Robert A. Heinlein

7.1 Levelized Cost of Electricity

The Levelized Cost of Electricity (LCOE) is a figure of merit used for energy production assessments. To compute the LCOE one needs to define the total capital cost of the project and net power produced for the operation period. The total capital cost of a geothermal system is a function of several terms: Leasing and Acquisition (LA); Royalty (*R*); Site Construction and Security (*SCS*); Drilling and Completion ($D\&C$); and Power Cycle (*PC*) installation cost (Barbier, 2000). This project is based on the assumption of power production is for the local usage in an existing manufacturing facility or local community. This fact excludes us from the royalty cost determination and makes the project less expensive.

The $D\&C$ cost is the largest term of the project. It depends on a target depth, rate of penetration, and mission of the well. The geothermal well’s $D\&C$ costs are higher than conventional oil and gas wells due to the larger diameter of the wells, higher temperature of the resource, and harsh environment of the geo-fluid causing corrosion and erosion of the well completion parts (Lukawski et al., 2014). There are two main types of $D\&C$ cost determination: detailed calculation including all aspects of drilling operation (Kaiser, 2016; Kipsang, 2014; Randebergi et al., 2012) and generalized statistical approach based on regression analysis. Lukawski et al. (2014) developed a graphical and mathematical relationship between the geothermal well measured depth and $D\&C$ cost, which is simple and easy to implement. Also, the LA and *SCS* are included into the statistical approach defining the averaged drilling costs.

$$DC = 1.72 \times 10^{-7} \times MD^2 + 2.3 \times 10^{-3} \times MD - 0.62 \quad (7.1)$$

The power cycle equipment is separated into two groups: petroleum industry available parts and unique parts including the turbine-generator assembly and a condenser. The first group includes DHE, packers, casings, and ESPs. The DHE is a coaxial pipe designed from the casings and tubings available in the petroleum industry. Three retrievable packers are included into the design scheme as well as two ESPs. The cost of these units are much smaller than $D\&C$ and partially included into the Capital cost (CC) adding 15% of contingency (Randebergi, et al., 2012).

The condenser cost ($CC_{Cond.}$) in dollars is defined from (Smith, 2005) and (Walrawen et al., 2015). The calculation includes a correction factor of 620 taken from Chemical Engineering (CE)-index in July 2013 for air cooled condensers (http://www.che.com/pci/):

$$CC_{Cond.} = 1.67 \times 10^5 \left(\frac{A_c}{200}\right)^{0.89} 1.35 \left(\frac{650.9}{620}\right) \tag{7.2}$$

where A_c is area of the condenser.

The turbine cost ($C_{turb.}$) depends on turbine power produced and is defined from (Walrawen et al., 2015)

$$C_{turb.} = -1.66 \times 10^4 + 716 \times W_t^{0.8} \times 1.35 \tag{7.3}$$

The sum of $CC_{Cond.}$ and $C_{turb.}$ is a PC cost. The obtained cost of power cycle parts is corrected for non-standard material ($f_{M.} = 1.7$) for stainless steel; high working pressure conditions ($f_{P.} = 1.5$), and installation expenses ($f_{I.} = 0.6$) (Smith, 2005):

$$PC = C(f_{M.}f_{P.} + f_{I.}) \tag{7.4}$$

where

$$C = CC_{cond.} + C_{turb.} \tag{7.5}$$

The total cost of the power unit is a sum of $D\&C$ and PC:

$$C_{tot.} = D\&C + PC \tag{7.6}$$

The procedure of calculating taxes is complicated, especially if the well is going to be drilled by another company. Assuming the fact that this type of power plant would be built for the internal company needs, and no power would be sold to the consumer the LCOE can be simply obtained from the known capital cost of the power unit divided by the total amount of electricity produced during 30 years (Walrawen et al., 2015):

$$LCOE = \frac{C_{tot.} + \sum_{t=1}^{t=30} C_{O\&M}(1+i)^{-t}}{\sum_{t=1}^{t=30}(E(1+i)^{-t})} \tag{7.7}$$

where i – is a discount rate; t- is a year of operation (30 years total), $C_{O\&M}$ – is operation and maintenance cost, which is 25% of the total cost (Smith, R., 2005):

$$C_{O\&M} = 0.025C_{tot.} \tag{7.8}$$

$$E = W_{net}N \tag{7.9}$$

where *N* is a number of full load hours per year, assumed of 95% (Walrawen et al., 2015).

7.2 Reference Reservoir Analysis

The example of D&C cost calculation is shown in the Table 7.1. The 15% contingency was assumed for any unexpected outgoings. The constant net power production of 156 kW was assumed for a single lateral well. Total well cost is about $17.5 mln, which is higher than in Kaiser (2016). The reason for this is a generalized trend of the curve in the equation 7.1.

Table 7.1: D&C cost calculation results for reference reservoir

Well measured depth, m	Drilling and completion cost, mln $	15% contingency, mln $	Total well cost, (DC), mln $
5,000	15.18	2.277	17.457

Kaizer (2016) analyzed LCOE by computing all costs for the particular drilling operation and assumed 200 kW net power, which is 25% higher than in the assumed system. The *PC* cost calculation results are presented in the Table 7.2.

Table 7.2: PC cost calculation example

w.f. mass flow rate, kg/s	Heat rejection, MW	Condenser area, m^2	Condenser cost, mnl $	Turbine cost, mln $	Power cycle cost corrected, mln $
10	1.85	21.51	0.032	0.081	0.356

Three cases were simulated for LCOE. As it is seen from the Figure 7.1 the LCOE increases with depth of the reservoir, and with discount rate reduction. The purple line represents a single lateral well with 10% discount rate. The red and green lines are constructed for four lateral wells (Figure 7.2).

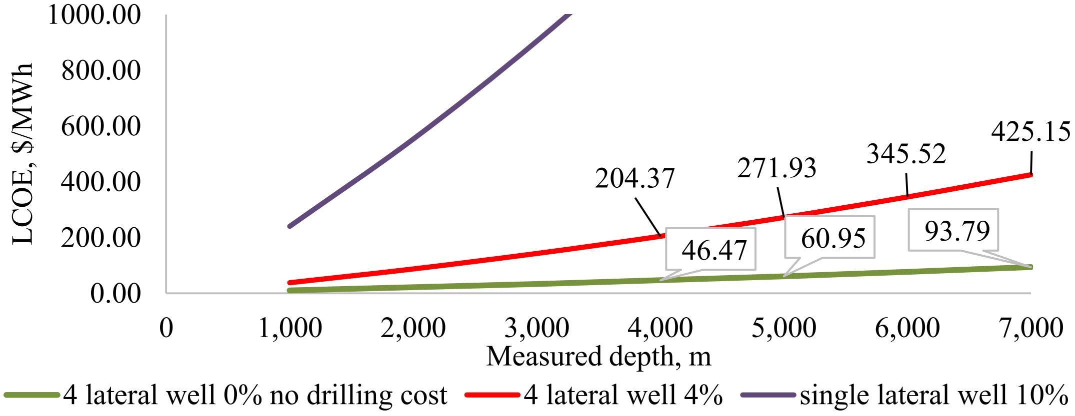

Figure 7.1: Levelized cost of electric power for the reservoir prototype case.

The discount rate for the red line is 4%. The green line assumes no drilling cost, but only recompletion of an existing well for the power production case. If the D&C cost is ignored and only recompletion cost is assumed as 20% of D&C cost, the $46.47/MWh can be reached for 4,000m target depth reservoir with temperature of 126°C. (Figure 7.3) Note the DOE proposed LCOE for 2020 is $48/MWh (By an MIT-led, A. A., 2006).

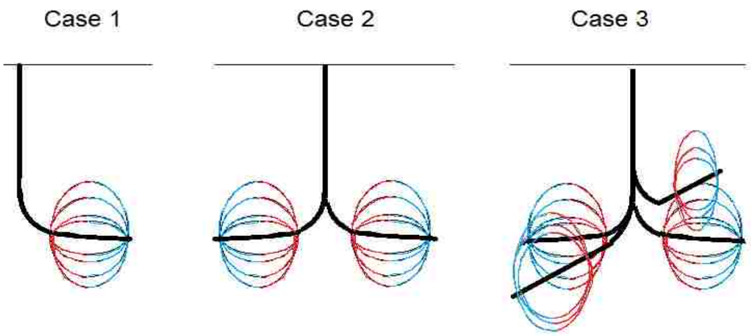

Figure 7.2: Possible lateral cases for power unit.
Case 1 is a single lateral well; case 2 is a dual lateral well; case 3 is four lateral well.

Increasing the net power (applying the system to the reservoirs with higher temperatures) plays crucial role in LCOE determination. For 220℃ reservoir temperature case the red curve dropped the LCOE to less than $100/MWh even for 7,000m depth (Figure 7.3). The green line, representing recompletion case shows $21.84/MWh at 7,000 m TD, which is half than DOE requirements (Figure 7.4). In case of drilling and completion costs included in to the account (red line) the increase in reservoir temperature gave optimistic shift toward satisfactory LCOE values ($47.59/MWh at the 4 km TD). All simulations were done for carbon dioxide working fluid.

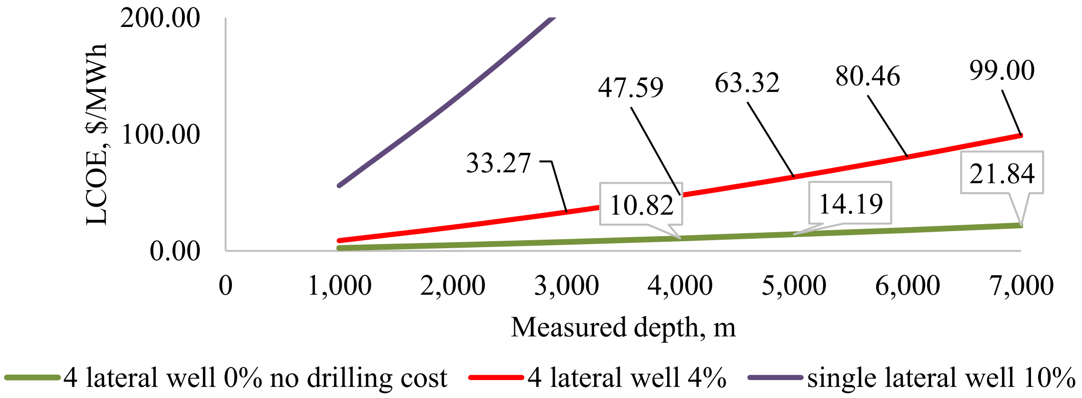

Figure 7.3: Levelized cost of electric power for the 220℃ reservoir case.

It is worth to note that not every petroleum well can be converted to the energy production unit for several reasons:

Technical challenges:

1. The well should have a horizontal section and a casing program should satisfy to the PC installation requirements. This includes inclination angles, perforated intervals, and casing diameters.
2. The horizontal section should have enough diameter to install DHE in it. Very often the oil and gas wells have small diameters at the TD (less than 5 inches).
3. The residual oil and gas content in the produced brine can cause several complications in reservoir circulation management. The temperature reduction in the DHE can provoke

heavy fractions solidification and precipitation on the DHE part, which will eventually cause clogging problems.

Risk assessment and cost:

1. Before the petroleum well is drilled the casing design and equipment should pass several standards and be certified. Adding energy production case to the well will eventually increase the cost of the well and add more standards, which will complicate the project.
2. The petroleum well served many years in production is not the same as new drilled well in terms of reliability and safety. It may require even more financial investment to transfer to the energy production unit. A detailed analysis may be a good topic for future exploration.

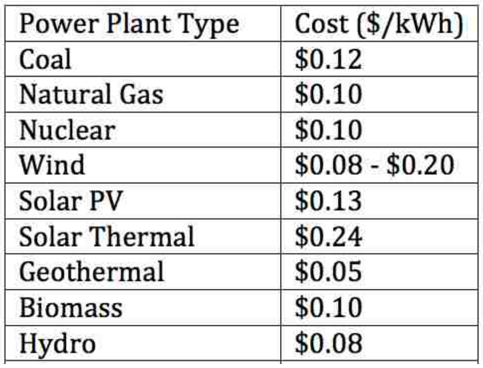

Power Plant Type	Cost ($/kWh)
Coal	$0.12
Natural Gas	$0.10
Nuclear	$0.10
Wind	$0.08 - $0.20
Solar PV	$0.13
Solar Thermal	$0.24
Geothermal	$0.05
Biomass	$0.10
Hydro	$0.08

Figure 7.4: DOE LCOE requirements for different types of resources (MIT, 2006).

7.3 Conclusions

In general the economic assessment showed satisfactory results with DOE requirements for several cases. It is possible to reach competitive LCOE values even with modest net power production from a well working on ZMW method. A novel idea of the recompletion existing petroleum wells to the power production unit is facing several challenges and makes questionable this direction of development.

CHAPTER 8: CONCLUSIONS AND SUGGESTIONS FOR FUTURE DEVELOPMENT

8.1 Main Achievements of the Project

- The ZMW method was presented and analyzed in this project. In general the analysis proved sustainable and workable design in terms of economy and power production features. High temperature of the reservoir and high permeability of the rock, and high reservoir volume are the main factors to use while choosing the right reservoir.
- The best working fluid from the power production concern was determined. CO_2 is more preferable for low reservoir temperatures for non-toxic and non-flammable characteristics, high pressure, high temperature stability, low cost and availability. Carbon dioxide works well for all range of the reservoir temperatures from 120 to 220°C. However, if the chosen reservoir temperature is close to 220°C the preference would be given to the pure hydrocarbons. In this case the N-pentane fluid is the best power productive fluid to apply for this design.
- The area of DHE is the main heat transfer parameter in the system that can be changed. While the diameters are fixed by the casing design, the length is the only variable to adjust. Increasing the DHE well increases pressure losses in the brine circulation loop and adds more power requirements for the brine pump. Decreasing the DHE length reduces the net power production due to lack of heat transfer area. The optimal length of 250 m was determined for reservoir prototype case. Changing the *w.f.* candidate would affect the optimal DHE length.
- Net power production is defined by seasonal and daily ambient air temperature fluctuations, as well as by the reservoir temperature drop. While the first variable is unstable, the reservoir temperature drop can be fixed by defining an optimal insulation interval between the producer and injector. The analysis is based on thermal breakthrough time determination, which is a function of flow rates and reservoir properties.

- The economic analysis shows a great potential for this system in case of high reservoir temperature. The LCOE is a function of reservoir depth and net power production. The maximum installation cost portion belongs to the well drilling costs.

8.2 Future Research Directions

- For the future development the author would suggest reduction of the influence from the ambient temperature fluctuations. This seems possible by using phase change materials (PCM), which become popular in heat storage projects. In this way, heat rejected by the condenser is absorbed by PCM, which changes phase from a solid to a liquid form. Installation of PCM bank inside the well at the turbine location can eliminate the use of traditional condenser and reduce to the minimum the surface footprint (Figure 8.1). From the other side, the system will gain additional weight from the PCM.

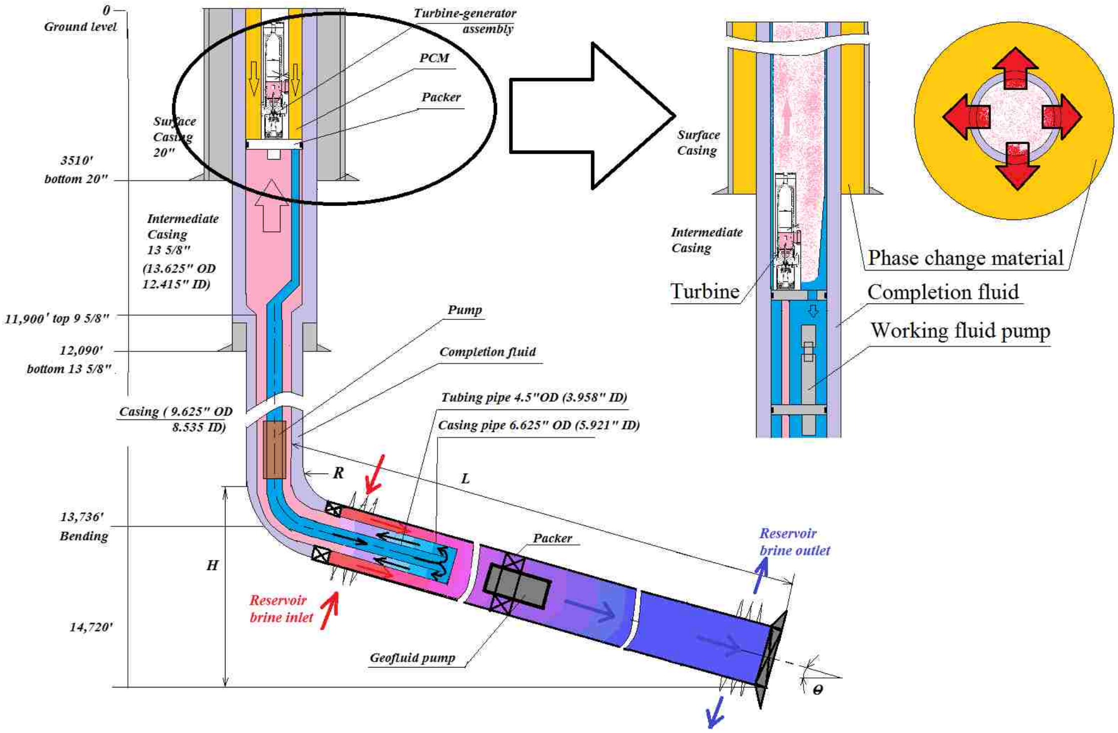

Figure 8.1: System with PCM cooling part instead of condenser.

- The U-tube design of the DHE is another possible improvement of the system. Figure 8.2 shows the cross sectional view of the dual U-tube heat exchanger inside the casing. This may reduce the frictional pressure drop in the horizontal well, thereby drop the brine pump requirements. However, running this type of heat exchanger may be complicated by brine pump installation. More detailed discussion about system installation procedure is presented in the Appendixes C and D.

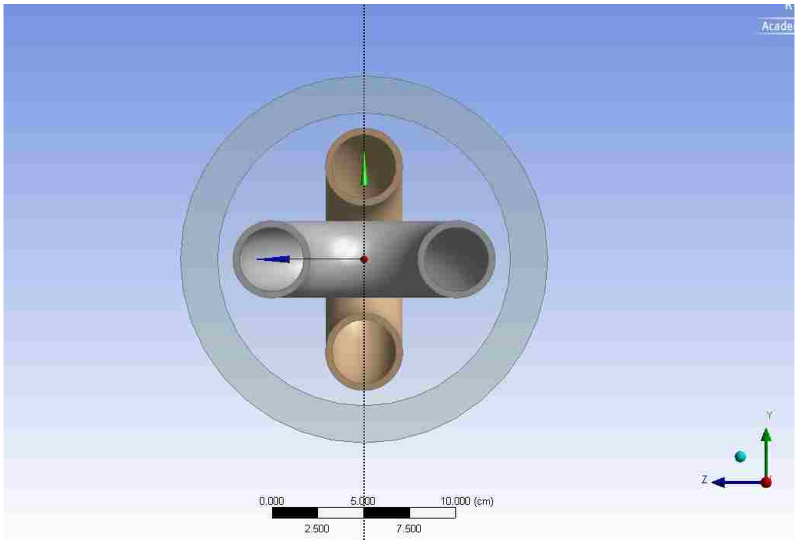

Figure 8.2: Dual U-tube DHE as an alternative design solution.

- According to the system description the power cable is running from the surface to the brine pumps along the entire well, which is expensive and time consuming operation. Additionally, the electric cable materials does not work well in the CO_2 environment. To avoid this it is possible to connect the positive power source directly to the central tubing (*w.f.* hot stream path) and use the negative polarity connected the cemented casing. The packers can be used as power distribution devices. Definitely this proposal requires complications in the packers design. Nevertheless, if the goal is achieved, the system would be more compact, more safe, and reliable.

- The system including the brine pumps, ICD and sand protection, DHE, cable, *w.f.* pump, tubings and casings is expected to have sufficient weight. This may be an issue when running the system into the well and require specially designed rig. To reduce the weight it is possible to move the turbine assembly to the top of the christmas tree, and the *w.f.* pump on the surface facility. Firstly, this scheme will ease the access to the mentioned devices and, thus, eliminate costly workover operations in case of turbine failure. The design becomes cheaper due to installation cost and elimination of supporting packers inside the well. Additionally, there is no need to have a space for the *w.f.* pump and turbine assembly installation. So, it is possible to run the production casing with a constant diameter along the well.

  From the other side, removing the *w.f.* pump to the surface will loose net power production. Carbon dioxide fluid has less density on the surface than on the bottom of the well, and, thus, would require more pumping power. Turbine on top installation would require more security issues to avoid vandalism accidents. Additionally, some improvement on the christmas tree design should be done to sustain possible vibrational load coming from the turbine-generator assembly.

- One more comment about the brine flow organization inside the horizontal offset of the well. Much more simplified design seems possible if the producer and injector are switched from the previously discussed scheme (Figure 8.3). Now the brine intake happens at the end of the horizontal offset. It is possible to install traditional gravel packed completion at the inlet. The system is simplified by having only brine pump assembly and a DHE inside the casing, and, thus, can have larger diameter heat exchanger. This has more power extraction potential from the reservoir. However, there is a dark side of this scheme, which lies in the flow organization through the DHE. The brine stream exit is located at the DHE region. So, there is no additional hot flux income to the heat exchanger as was discussed previously. This fact may negatively impact the DHE performance and would require brine flow rate increase, which is additional load on the brine pump.

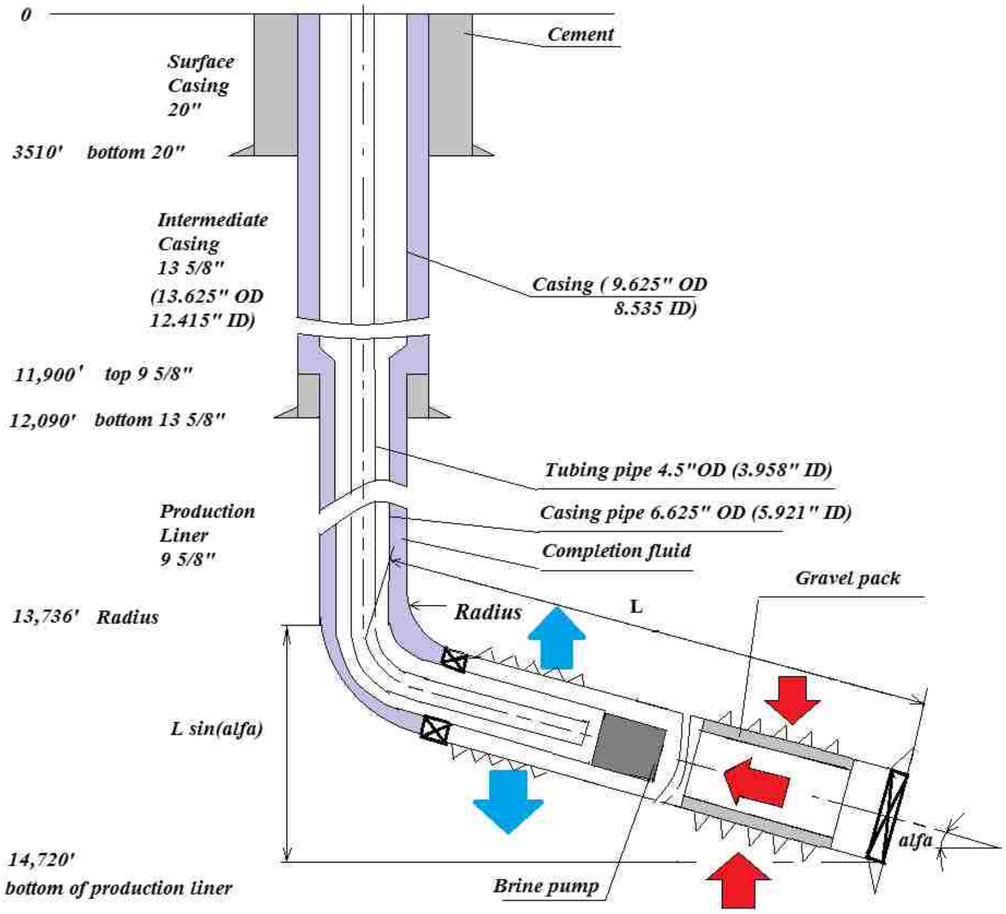

Figure 8.3: The alternative design scheme.

REFERENCES

Akhmadullin, I., & Tyagi, M. (2014). Design and Analysis of Electric Power Production Unit for Low Enthalpy Geothermal Reservoir Applications. *World Academy of Science, Engineering and Technology, International Journal of Environmental, Chemical, Ecological, Geological and Geophysical Engineering*, *8*(6), 443-449.

Angelino, G., Gaia, M., & Macchi, E. (1984). A review of Italian activity in the field of organic Rankine cycles. *VDI-Berichte*, (539), 465-482.

Anklam, E. G., & Wiggins, M. L. (2005, January). Horizontal-Well Productivity and Wellbore-Pressure Behavior Incorporating Wellbore Hydraulics. In *SPE Production Operations Symposium*. Society of Petroleum Engineers.

Ansari, E. (2016). *Mathematical Scaling and Statistical Modeling of Geopressured Geothermal Reservoirs* (Doctoral dissertation, Louisiana State University).

Asheim, H., Kolnes, J., & Oudeman, P. (1992). A flow resistance correlation for completed wellbore. *Journal of Petroleum Science and Engineering*, *8*(2), 97-104.

Augustine, J. R., Mathis, S. P., Nguyen, H. T., Gann, C. L., & Gill, J. (2006, January). World's First Gravel Packed Uniform Inflow Control Completion. In *SPE Annual Technical Conference and Exhibition*. Society of Petroleum Engineers.

Barbier, E. (2002). Geothermal energy technology and current status: an overview. *Renewable and Sustainable Energy Reviews*, *6*(1), 3-65.

Bassett L., (2004). Case History Using ESP's to De-Water Horizontal Wells, SPE 133464.

Brill, J.P. and Beggs, H.D., (1986). "Two-Phase Flow in Pipes," SPE 5th Edition, copyright by J.P. Brill and H.D. Beggs.

Bejan, A. (1982). Second-law analysis in heat transfer and thermal design. *Advances in heat transfer*, *15*(1), 1-58.

Bergman, T. L., Incropera, F. P., & Lavine, A. S. (2011). *Fundamentals of heat and mass transfer*. John Wiley & Sons.

Bianchi, M., & De Pascale, A. (2011). Bottoming cycles for electric energy generation: parametric investigation of available and innovative solutions for the exploitation of low and medium temperature heat sources. *Applied Energy*, *88*(5), 1500-1509.

Boyko, L. D., & Kruzhilin, G. N. (1967). Heat transfer and hydraulic resistance during condensation of steam in a horizontal tube and in a bundle of tubes. *International Journal of Heat and Mass Transfer*, *10*(3), 361-373.

Bridger, D. W., & Allen, D. M. (2005). Designing aquifer thermal energy storage systems. *ASHRAE JOURNAL*, *47*(9), S32.

Bringedal, C., Berre, I., & Radu, F. A. (2014). An approach for investigation of geochemical rock-fluid interactions. *Modeling of heat transfer in porous media in the context of geothermal energy extraction*. In *Proceedings of the Thirty-Ninth Workshop on Geothermal Reservoir Engineering Stanford University, Stanford, California,* SGP-TR-202.

Bronicki, L. Y., & Schochet, D. N. (2005, January). Bottoming organic cycle for gas turbines. In *ASME Turbo Expo 2005: Power for Land, Sea, and Air* (pp. 79-86). American Society of Mechanical Engineers.

Brown, K. E. (1984). The technology of artificial lift methods, Volume 4-Production optimization of oil and gas wells by nodal systems analysis.

Brown, D. W. (2000, January). A hot dry rock geothermal energy concept utilizing supercritical CO_2 instead of water. In *Proceedings of the twenty-fifth workshop on geothermal reservoir engineering, Stanford University* (pp. 233-238).

Cengel, Y. A. (2010). *Fluid mechanics*. Tata McGraw-Hill Education.

Centrilift, B. H. (2008). Submersible Pump Handbook. Baker Hughes.

CHEMICAL ENGINEERING WWW.CHEMENGONLINE.COM JANUARY 2015

Chen, Y., Lundqvist, P., Johansson, A., & Platell, P. (2006). A comparative study of the carbon dioxide transcritical power cycle compared with an organic Rankine cycle with R123 as working fluid in waste heat recovery.*Applied Thermal Engineering*, *26*(17), 2142-2147.

Chisholm, D. (1967). A theoretical basis for the Lockhart-Martinelli correlation for two-phase flow. *International Journal of Heat and Mass Transfer*, *10*(12), 1767-1778.

Church, E. F. (1950). *Steam turbines*. McGraw-Hill.

Coltharp, E. D. (1984). Subsurface electrical centrifugal pumps. *Journal of petroleum technology*, *36*(04), 645-652.

Davis, A. P., & Michaelides, E. E. (2009). Geothermal power production from abandoned oil wells. *Energy*, *34*(7), 866-872.

DiPippo, R. (2004). Second law assessment of binary plants generating power from low-temperature geothermal fluids. *Geothermics*, *33*(5), 565-586.

DiPippo, R. (2012). *Geothermal power plants: principles, applications, case studies and environmental impact*. Butterworth-Heinemann.

Durham Jr, C. O. (1978). *Analysis of Cameron Parish geopressured aquifer. Final report* (No. NVO-1561-1). Magma Gulf Co., Baton Rouge, LA (USA).

Ellis, T., Erkal, A., Goh, G., Jokela, T., Kvernstuen, S., Leung, E. ... & Raffn, A. G. (2009). Inflow Control Devices—Raising Profiles. *Oilfield Review*, *21*, 30-37.

El-Sayed, A. A., Khalaf, F., & Ghzaly, S. M. (1991, January). Casing design considerations for horizontal wells. In *Middle East Oil Show*. Society of Petroleum Engineers.

Feng, Y. (2012). *Numerical study of downhole heat exchanger concept in geothermal energy extraction from saturated and fractured reservoirs* (Doctoral dissertation, Louisiana State University).

Feng, Y., Tyagi, M., & White, C. D. (2015). A downhole heat exchanger for horizontal wells in low-enthalpy geopressured geothermal brine reservoirs. *Geothermics*, *53*, 368-378.

Friedel, L. (1979, June). Improved friction pressure drop correlations for horizontal and vertical two-phase pipe flow. In *European two-phase flow group meeting, Paper E* (Vol. 2, p. 1979).

Fuchs, P. H. (1975). *Pressure drop and heat transfer during flow of evaporating liquid in horizontal tubes and bends* (Doctoral dissertation, Ph. D Thesis, NTH, Trondheim, Norway).

Giger, F. M. (1985, January). Horizontal wells production techniques in heterogeneous reservoirs. In *Middle East Oil Technical Conference and Exhibition*. Society of Petroleum Engineers.

Gray, T. A., & Nunn, J. A. (2010). Geothermal Resource Assessment of the Gueydan Salt Dome and the Adjacent Southeast Gueydan Field, Vermilion Parish, Louisiana.

Grove, D. B., & Beetem, W. A. (1971). Porosity and dispersion constant calculations for a fractured carbonate aquifer using the two well tracer method. *Water Resources Research*, *7*(1), 128-134.

Haynes, W. M. (Ed.). (2014). *CRC handbook of chemistry and physics*. CRC press.

Heberle, F., & Brüggemann, D. (2010). Exergy based fluid selection for a geothermal Organic Rankine Cycle for combined heat and power generation. *Applied Thermal Engineering*, *30*(11), 1326-1332.

Henriksen, K. H., Augustine, J. R., & Wood, E. T. (2005, January). Integration of new open hole zonal isolation technology contributes to improved reserve recovery and revision in industry best practices. In *SPE International Improved Oil Recovery Conference in Asia Pacific*. Society of Petroleum Engineers.

Herl, S., & Eudey, D. (2009). Electric submersible pumps fine-tuned for gassy wells. *Hart's E & P*, *82*(8), 53-56.

Houghton, E. L., Carpenter, P. W., Collicott, S., & Valentine, D. (2012).*Aerodynamics for engineering Students*. Elsevier.

Joshi, S. D. (1988). Augmentation of well productivity with slant and horizontal wells (includes associated papers 24547 and 25308). *Journal of Petroleum Technology*, *40*(06), 729-739.

Incropera, F. P., DeWitt, D. P., & Lavine, A. S. (1990).*Fundamentals of heat and mass transfer*. John Wiley & Sons.

Ismail, B. (2011). Advanced electrical power generation technology using renewable & clean low-enthalpy geothermal energy sources. *Recent Patents on Mechanical Engineering*, *4*(2), 168-179.

Invernizzi, C., Iora, P., & Silva, P. (2007). Bottoming micro-Rankine cycles for micro-gas turbines. *Applied thermal engineering*, *27*(1), 100-110.

Kaiser, M. J. (2016). Economic Analysis of a Zero-Mass Withdrawal Geothermal Energy System. *Journal of Sustainable Energy Engineering*, *3*(3), 191-220.

Kalra, C., Becquin, G., Jackson, J., Laursen, A. L., Chen, H., Myers, K. ... & Zia, J. (2012, January). High-Potential Working Fluids and Cycle Concepts for Next-Generation Binary Organic Rankine Cycle for Enhanced Geothermal Systems. In *37th Workshop on Geothermal Reservoir Engineering, Stanford, CA, Jan*.

Kipsang, C. (2014). Cost model for geothermal wells. UNU Geothermal Training Program, Iceland. Report.

Larkin, A., & Davies, K. (2009). Natural refrigerants: The Solution. *Greenpeace, http://www. Greenpeace.org/usa/assets/binaries/hfc-solutions-fact-sheet*.

Lockhart, R. W., & Martinelli, R. C. (1949). Proposed correlation of data for isothermal two-phase, two-component flow in pipes. *Chem. Eng. Prog*, *45*(1), 39-48.

Lukawski, M. Z., Anderson, B. J., Augustine, C., Capuano, L. E., Beckers, K. F., Livesay, B., & Tester, J. W. (2014). Cost analysis of oil, gas, and geothermal well drilling. *Journal of Petroleum Science and Engineering*, *118*, 1-14.

Lund, J. W. (2007). Characteristics, development and utilization of geothermal resources. *Oregon Inst. Tech*, *28*(2).

Luo, J., & Kitanidis, P. K. (2004). Fluid residence times within a recirculation zone created by an extraction–injection well pair. *Journal of Hydrology*, *295*(1), 149-162.

Luo, J., (1998). *A mathematical modelling of horizontal wells productivity and well test analysis* ((Master thesis, Virginia Polytechnic Institute and State University).

McCoy, R. L., Hartsock, J. H., & Dobson, R. J. (1980, January). Preliminary Results Of The Wells-Of-Opportunity Geopressured-Geothermal Testing Program. In *SPE Unconventional Gas Recovery Symposium*. Society of Petroleum Engineers.

Mikielewicz, J., Piwowarski, M., & Kosowski, K. (2009). Design analysis of turbines for co-generating micro-power plant working in accordance with organic Rankine's cycle. *Polish Maritime Research*, *16*(Special), 34-38.

Mines, G. L. (1982). *Preliminary report on the baseline thermal and hydraulic performance tests of a sieve tray direct contact heat exchanger* (No. EGG-GTH-6101). Idaho National Engineering Lab., Idaho Falls (USA).

By an MIT-led, A. A. (2006). Interdisciplinary Panel (Chaired by JW Tester).*The Future of Geothermal Energy, Impact of Enhanced Geothermal Systems (EGS) on the United States in the 21st Century*.

Moran, M. J., Shapiro, H. N., Boettner, D. D., & Bailey, M. B. (2010).*Fundamentals of engineering thermodynamics*. John Wiley & Sons.

Muskat, M., & Meres, M. W. (1936). The flow of heterogeneous fluids through porous media. *Journal of Applied Physics*, *7*(9), 346-363.

Nalla, G., Shook, G. M., Mines, G. L., & Bloomfield, K. K. (2005). Parametric sensitivity study of operating and design variables in wellbore heat exchangers. *Geothermics*, *34*(3), 330-346.

Neeraas, B. O. (1993). Condensation of Hydrocarbon Mixtures in Ciol-Wound LNG Heat Exchangers Tube-Side Heat Transfer and Pressure Drop. *Doktor, The Norwegian Institute of Technology, Trondheim, Norway*, 92-100.

Ouyang, L. B., Arbabi, S., & Aziz, K. (1997). *General single phase wellbore flow model* (No. DOE/BC/14862--T1). Stanford Univ., CA (United States). Dept. of Petroleum Engineering.

Phillips, O. M. (2009). *Geological fluid dynamics: sub-surface flow and reactions*. Cambridge University Press.

Plaksina, T. (2011). *Modeling effects of coupled convection and CO2 injection in stimulating geopressured geothermal reservoirs* (Doctoral dissertation, Lawrence University).

Papadopulos, S. S., Wallace Jr, R. H., Wesselman, J. B., & Taylor, R. E. (1975). Assessment of onshore geopressured-geothermal resources in the northern Gulf of Mexico basin. *US Geological Survey, Circular*, *726*, 125-140.

Quoilin, S., Van Den Broek, M., Declaye, S., Dewallef, P., & Lemort, V. (2013). Techno-economic survey of Organic Rankine Cycle (ORC) systems.*Renewable and Sustainable Energy Reviews*, *22*, 168-186.

Rahman, S. S., & Chilingarian, G. V. (1995). *Casing Design-Theory and Practice* (Vol. 42). Elsevier.

Randebergi, E., Fordi, E., Nygaardi, G., Erikssonii, M., Gressgardi, L. G., Hanseni, K., (2012). "Potentials for Cost Reduction for Geothermal Well Construction in View of Various Drilling Technologies and Automatization Opportunities". In 36th Workshop on Geothermal Reservoir Engineering, Stanford University. SGP-TR-194.

Ratterman, G. (2006). Uniform flow profiles improve horizontal wells. *Drilling contractor*.

Rouhani, S.Z., Axelson, E., 1970, Calculation of Void Volume Fraction in the Subcooled and Quality Boiling Regions, International Journal of Heat Mass Transfer, 13, 383-393.

Sarkar, J. (2015). Review and future trends of supercritical CO 2 Rankine cycle for low-grade heat conversion. *Renewable and Sustainable Energy Reviews*, *48*, 434-451.

Schuster, A., Karellas, S., Kakaras, E., & Spliethoff, H. (2009). Energetic and economic investigation of Organic Rankine Cycle applications. *Applied thermal engineering*, *29*(8), 1809-1817.

Shook, G. M. (2001). Predicting thermal breakthrough in heterogeneous media from tracer tests. *Geothermics*, *30*(6), 573-589.

Smith, R. (2005). *Chemical process design*. John Wiley & Sons, Inc.

Sohel, M. I., Sellier, M., Brackney, L. J., & Krumdieck, S. (2011). An iterative method for modelling the air-cooled organic Rankine cycle geothermal power plant. *International Journal of Energy Research*, *35*(5), 436-448.

Song, J., & Gu, C. W. (2015). Analysis of ORC (Organic Rankine Cycle) systems with pure hydrocarbons and mixtures of hydrocarbon and retardant for engine waste heat recovery. *Applied Thermal Engineering*, *89*, 693-702.

Stand, A. Designation and safety classification of refrigerants. *2010-07-27)[2014-11-09]. www. ashrae, org*.

Strack, O. D. (1989). *Groundwater mechanics*. Prentice Hall.

Thome, J. R., El Hajal, J., & Cavallini, A. (2003). Condensation in horizontal tubes, part 2: new heat transfer model based on flow regimes. *International Journal of Heat and Mass Transfer*, *46*(18), 3365-3387.

Van Den Brink, G. J., & Hoogendoorn, C. J. (1983). Ground water flow heat losses for seasonal heat storage in the soil. *Solar Energy*, *30*(4), 367-371.

Varney, J., & Bean, N. (2012). Air-Cooled Binary Rankine Cycle Performance With Varying Ambient Temperature. In *Geothermal Resources Council Annual Meeting (36th: 2012: Reno, Nevada, USA)*.

Walraven, D., Laenen, B., & D'haeseleer, W. (2015). Minimizing the levelized cost of electricity production from low-temperature geothermal heat sources with ORCs: Water or air cooled? *Applied Energy*, *142*, 144-153.

Wang, D., Ling, X., & Peng, H. (2013). Cost-effectiveness performance analysis of organic Rankine cycle for low grade heat utilization coupling with operation condition. *Applied Thermal Engineering*, *58*(1), 571-584.

Wang, Z., McClure, M. W., & Horne, R. N. (2009). A single-well EGS configuration using a thermosiphon. In *Workshop on Geothermal Reservoir Engineering, Stanford University, Stanford, CA*.

Welty, C., & Gelhar, L. W. (1994). Evaluation of longitudinal dispersivity from nonuniform flow tracer tests. *Journal of Hydrology*, *153*(1), 71-102.

Wendt, D., & Mines, G. (2011). Effect of Ambient Design Temperature on Air-Cooled Binary Plant Output. *Idaho: DoE Idaho National Laboratory*.

Zheng, C., & Bennett, G. D. (2002). *Applied contaminant transport modeling* (Vol. 2). New York: Wiley-Interscience.

APPENDIX A TURBINE DESIGN

A 1. Turbine Modelling

The usual axial turbine has four main parts. The rotor is the rotating part which carries the blades. The stator consists of a cylinder and shell where the rotor turns. The turbine has a frame and nozzles. The cylinder, shell, and frame are often combined. Other parts necessary for proper operation would include a control system, piping, a lubrication system, and a separate condenser which are not a part of this design.

Assumptions:

The blades of the turbine have frictionless surfaces, and energy conversion on the blade is complete. The fluid flow path matches with blades or nozzle geometry. There is no flow separation from the blades surface. The flow is uniform and steady; has the same properties at every blade of the stage.

A 2. Conversion of Steam Kinetic Energy into Blade Work

This maximum possible conversion of kinetic energy of the entering jet into blade work occur when a frictionless blade turns the steam through 180° and flow exits with zero absolute velocity. The absolute velocity of the jet stream entering the blade, V_1 is not equal to the blade speed, V_b though. Then one can design the nozzle in such way that velocity at the exit can provide maximum energy conversion.

$$V_1 = W_1 + V_b \tag{A.1}$$

$$V_2 = W_2 + V_b \tag{A.2}$$

Where indexes 1, and 2 denote inlet and outlet velocities.

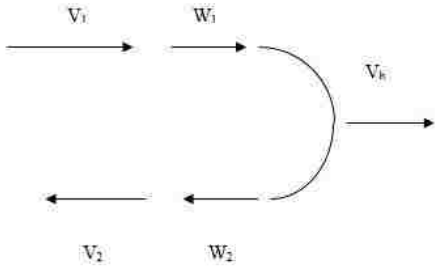

Figure A.0.1: Simplified blade flow scheme

With the assumption of frictionless blade and complete energy conversion in the turbine blade:

$$W_2 = -W_1 \; and \; V_2 = 0 \qquad (A.3)$$

From that will have:

$$V_1 = 2V_b \qquad (A.4)$$

The above derivation assumes zero angle between tangential flow direction V_1. In fact, due to geometry restrictions, this nozzle angle changes from 10 to 30 degrees. Small angle cause an excessively long nozzle that would increase friction and decrease efficiency. High angle cause flow direction change and again loss in efficiency. Therefore, an optimal value should be obtained. Then equation (A.4) with nozzle angle α correction becomes:

$$V_1 cos\alpha = 2V_b \qquad (A.4)$$

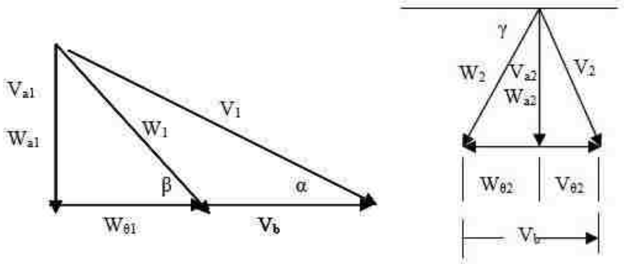

Figure A.0.2: Entry and exit triangles scheme.

Another design parameter is angle γ which is vary from 15 to 40 degrees depending on size of the turbine. The designer is interested in reducing γ to increase the blade efficiency. The Table 0.1 illustrates all formulas to find the velocity components.

Shaft torque value is derived from the Reynolds transport theorem for angular momentum applied to one entrance and one exit scheme. Assuming steady state flow and no contribution from the radial component of the velocity the equation reduces to:

$$T = \dot{m}r(V_{\theta 2} - V_{\theta 1}) \tag{A.5}$$

where $V_{\theta 2} - V_{\theta 1}$ is change in tangential velocity.

The shaft work then is:

$$\dot{W}_{shaft} = \dot{m}r\omega(V_{\theta 2} - V_{\theta 1}) = \dot{m}V_b(V_{\theta 2} - V_{\theta 1}) \tag{A.6}$$

Table 0.1: Entry and exit triangles velocity formulas

Entry triangle	Exit triangle
$\boldsymbol{V_{\theta 1} = V_1 cos\alpha}$	$W_2 = k_b W_1$
$\boldsymbol{V_{a1} = W_{a1} = V_1 sin\alpha}$	$V_{a2} = W_2 sin\gamma$
$\boldsymbol{W_{\theta 1} = V_{\theta 1} - V_b}$	$W_{\theta 2} = W_2 cos\gamma$
$\boldsymbol{W_1 = \sqrt{W_{a1}^2 + W_{\theta 1}^2}}$	$V_{\theta 2} = V_b + W_{\theta 2}$
$\boldsymbol{\beta = tan^{-1}\frac{W_{a1}}{W_{\theta 1}}}$	$V_2 = \sqrt{V_{a2}^2 + W_{\theta 2}^2}$

The velocity coefficient k_b is responsible for the total change of stream direction in the blade$\left[180^\circ - (\mu + \gamma)\right]$. It is determined empirically from (Church, E. F., 1954):

$$k_b = \sqrt{0.892 - 0.00006W_1} \tag{A.7}$$

The algorithm of calculating turbine efficiency is illustrated in the table below.

Table A.0.2: Turbine calculation algorithm according to (Church, 1954)

Assume nozzle angle	9 degrees
Entry triangle	Church suggests to increase V_1 by 10% to account for dick friction and fanning
Exit triangle	See table 0.1
Blade work per unit mass	$W_b = -V_b(V_{\theta 2} - V_{\theta 1})$
Actual energy per blade	$E_{act} = \frac{V_1^2}{2}$
Blade efficiency	$\eta_b = \frac{W_b}{E_{act}}$
Nozzle Velocity Coefficient	$k_n = 1.021 - 0.164x + 0.165x^2 - 0.0671x^3 + 0.0088x^4$ $x = V_{s1} / 1000$
Ideal (Isentropic) nozzle exit/blade entrance velocity	$V_{s1} = \frac{\boldsymbol{V_1}}{k_n}$
Nozzle efficiency	$\eta_n = \frac{V_1^2}{V_{s1}^2}$
Combined efficiency	$\eta_{nb} = \eta_b \eta_n$
Stage efficiency Assuming an average loss from disk friction and *fanning* of 4% and from *leakage* of 1.5 %.	$\eta_{st} = \eta_{nb}(1 - \frac{frict.}{fan.} + leak)$
Ideal available energy per blade	$\Delta h_b = \frac{V_{s1}^2}{2}$
Total isentropic drop in enthalpy	$(\Delta h_s)_{total} = h_{inlet} - h_{outlet}$
Reheat	*R=1.0465*
Trial number of stages	$n = \frac{(\Delta h_s)_{total} R}{\Delta h_s}$
Actual reheat	$R_n = 1 + (R+1)\left(1 - \frac{1}{n}\right)\left(\frac{1-\eta_s}{0.2}\right)$
Enthalpy drop per stage	$\Delta h_s = \frac{(\Delta h_s)_{total} R}{n}$
Heat leak. If the desired pressure after the turbine is not reached, a new trial Δh_s and corresponding q_r are found and additional iterations run as needed.	$q_r = \Delta h_s - \Delta h_s \eta_{st}$

Total internal work per *lb* steam	$w_i = n(\Delta h_s - q_r)$
Internal efficiency of turbine	$\eta_i = \frac{w_i}{(\Delta h_s)_{total}}$
Engine efficiency, Assuming radiation loss of about 0.2 %, and the combined mechanical and radiation losses of about 2 %.	$\eta e = 0.98\, \eta_i$
Ideal steam rate: mass of steam required to produce a single kilowatt of power.	$ISR = \frac{= 3413(Btu/kWh)}{(\Delta h_s)_{total}(Btu/lbm)}$
Brake steam rate Corrects the ideal steam rate for the inefficiencies of the turbine.	$BSR = \frac{ISR}{\eta e}$
Turbine mass flow rate, where W is desired power	$\dot{m} = \frac{BSR\ W}{3600}$

APPENDIX B CONDENSER DESIGN

B 1. Two Phase Pressure Drop Analysis

A total pressure drop consists of three components, namely frictional pressure drop (dp_{frict}), acceleration pressure drop (dp_{accel}):

$$dp = dp_{frict} + dp_{accel} \tag{B.1}$$

The hydrostatic pressure drop is omitted due to condensation takes place in a horizontally oriented device at the surface facility.

Acceleration pressure drop usually small comparing with other pressure drops and is defined as:

$$dp_{accel} = -G^2\left[\left(\frac{x^2}{\varepsilon\rho_g} + \frac{(1-x)^2}{(1-\varepsilon)\rho_l}\right)_{out} - \left(\frac{x^2}{\varepsilon\rho_g} + \frac{(1-x)^2}{(1-\varepsilon)\rho_l}\right)_{in}\right] \tag{B.4}$$

where *G* is mass flux per unit area; ρ_g, ρ_l are densities of gas and liquid stages of *w.f.*; ε is void fraction, *x* is vapor fraction.

Density of the gas-fluid mixture is defined by gas fraction density ρ_g, liquid fraction density ρ_l, and void fraction ε.

$$\rho = \varepsilon\rho_g + (1-\varepsilon)\rho_l \tag{B.2}$$

Void fraction is determined from (Rouhani & Axelsson, 1970):

$$\varepsilon = \frac{A_g}{A} = \frac{1}{1 + \left(\frac{1-x}{x}\right)\left(\frac{\rho_g}{\rho_l}\right)} \tag{B.3}$$

The fluid density changes with pressure, temperature, and phase, therefore, one should refer to the working fluid thermodynamic properties to define (ρ) at each calculation step.

Friction pressure drop for two-phase flow is a function of geometry, surface roughness, Reynolds number, friction factor and fluid properties. All mentioned values are functions of a void fraction term. To solve this problem some methods use flow pattern recognition, based on void fraction calculation. Numerous flow pattern maps have been proposed for predicting flow pattern in two-phase flow. For every fluid the mentioned map is unique. To simplify the solution let us define the pressure drop as a function of void fraction.

There are many experimental correlations for friction pressure drop determination (Lockhart and Martinelli, 1949), (Chrisholm, 1969), (Friedel, 1979), (Fuchs, 1975), (Beggs and Brill, 1986) etc. The first mentioned correlation does not account for mass flux effects and over predicts pressure drop comparing with others. (Friedel, 1979) correlation was developed from a 25,000 experimental data sets, but has huge uncertainty up to 50%. Chrisholm (1969) developed correlation based on Lockhart-Martinelli's work, adding parameters to account fluid properties and mass flux. Fuchs correlation was proved by experiments with R12 refrigerant flow and has only 10% discrepancy from the experimental data. (Neeraas et al., 1993) conducted experiments with hydrocarbons, and found a good agreement of Fuchs method with proposed corrected function. Fuchs correlation is based on two-phase enhancement factor which is a function of vapor fraction *x*, Froude number and density ratio:

$$\xi = \frac{\frac{dp}{dz} - \left(\frac{dp}{dz}\right)_l}{\left(\frac{dp}{dz}\right)_g - \left(\frac{dp}{dz}\right)_l} \qquad (\mathrm{B}.5a)$$

Additionally, Fuch presented an empirical correlation for ξ as a function of liquid quality *x*:

$$\begin{gathered} \xi = 6740.33172 * x^{11} - 36759.087741 * x^{10} + 85275.119778 * x^{9} - \\ 110168.145383 * x^{8} + 87170.939162 * x^{7} - 43797.819250 * x^{6} + \\ +14021.596088 * x^{5} - 2790.120307 * x^{4} + 324.432076 * x^{3} - \\ -18.611125 * x^{2} + 2.414768 * x - 0.000141 \qquad (\mathrm{B}.5b) \end{gathered}$$

Correction has been made by Neeraas experimenting with propane, methane and ethane:

$$(dp)_{frict} = \left(\left(\frac{dp}{dz}\right)_{Fuchs} * \left[1 - \left(1 - 0.3g\left\{\frac{\rho_l}{\rho_g}\right\}\right)\right] * b(x) \right) dz \qquad (B.6)$$

where the $g\left\{\frac{\rho_l}{\rho_g}\right\}$ term depends on flow pattern and defined according to the flow map for different regimes:

$$g\left\{\frac{\rho_l}{\rho_g}\right\} = \frac{1}{0.3} \qquad for\ \frac{\rho_l}{\rho_g} > 20 \qquad (B.7a)$$

$$g\left\{\frac{\rho_l}{\rho_g}\right\} = \left(\frac{\rho_l}{\rho_g}\right)^{0.4} \qquad for\ 6.5 \leq \frac{\rho_l}{\rho_g} \leq 20 \qquad (B.7b)$$

$$g\left\{\frac{\rho_l}{\rho_g}\right\} = 6.5^{0.4} \qquad for\ \frac{\rho_l}{\rho_g} < 6.5 \qquad (B.7c)$$

Vapor fraction correction:

$$b(x) = \frac{\sin(\pi x) + \sin(\pi x^3)}{1.69}, \quad for\ x \leq 0.725 \qquad (B.8a)$$

$$b(x) = 1 - \sin\left\{\frac{\pi}{2}\left(\frac{x - 0.725}{0.275}\right)^{5x^{\frac{7}{2}}}\right\}, \quad for\ x > 0.725 \qquad (B.8b)$$

To model the two phase pressure drop the vapor fraction was assigned. Then the densities were calculated for condensation temperature values. With these known parameters the pressure drops were computed by the help of formulas B.3, and B.4. The total pressure drop was defined using formula B.1

B 2. Condensation Heat Transfer Coefficient

To develop a discussion about heat transfer in the condensation process let us introduce first with assumptions. This discussion is related only to a single component fluids. The vapor phase is assumed to be saturated and only liquid phase is responsible for the heat transfer. With high flow rates inside of the tubing the liquid phase forms first at the inner walls of the tube. Interfacial shear creates turbulent flow in the liquid film. Therefore, convective heat transfer process is dominated over conduction.

Internal Condensation Heat Transfer

Different models exist for prediction of convective condensation for pure components. The attention was paid to the researchers published their work in heat transfer correlations for condensation of organic fluids. Among all of them the main interest was rewarded to the modified Boyko and Kruzhilin (1967) correlation (BKC) and Thome's correlation (2003). The last one is based on a database of results from experiments with hydrocarbons and pure refrigerants. Thome's formula has a minimum of empirically determined constants and dependents more on the liquid thermal conductivity. The modified Boyko and Kruzhilin correlation is interesting because the modification is made based on experiments with high-pressure hydrocarbons and more depended in mass fraction and density ratio. Neeraas (2003) found that BKC with some correction gives a good agreement to his experiments with propane. The modified heat transfer coefficient correlation is in the following matter:

$$h(x) = k_{\alpha} h_{lo} \sqrt{1 + x_l \left[\frac{\rho_l}{\rho_g} - 1\right]} \tag{B.9}$$

where k_{α} is a function of liquid fraction x_l:

$$k_{\alpha} = \frac{1}{1.15 - 0.275 x_l} \tag{B.10}$$

h_{lo} is the heat transfer coefficient if liquid would occupy all cross sectional area. This parameter can be found from known Nusselt number (N_u), diameter of the tubing, and thermal conductivity of the fluid at the given temperature.

External Forced Convection

External forced convection is developed from the model of a flow around cylindrical bodies (Incopera, 1990). The condenser was assumed to have several cylindrical tubes and external forced convection manages the heat transfer coefficient, which tends to increase with air velocity. With further increase of air flow across the tubes the boundary layer does not manage to follow the single tube's curvature and forms a separation at the rear side of the tubes. (Cengel, 2010) suggests the following correlation from Churchill and Bernstein for the fluids with $RePr \geq 0.2$:

$$Nu_{forced} = 0.3 + \frac{0.62\,Re^{1/2}Pr^{1/3}}{\left[1 + \frac{0.4}{Pr^{2/3}}\right]^{1/4}}\left[1 + \left(\frac{Re}{282000}\right)^{5/8}\right]^{4/5} \qquad (B.12)$$

The external heat transfer coefficient is determined from known outer diameter of the tubing (D_{tubing}) and air thermal conductivity (λ_{air}):

$$h_{air} = \frac{Nu_{forced}\,D_{tubing}}{\lambda_{air}} \qquad (B.14)$$

The air properties are evaluated at the film temperature defined as an arithmetic mean between the wall and ambient air temperature:

$$T_{film} = \frac{T_{wall} + T_{air}}{2} \qquad (B.15)$$

APPENDIX C SYSTEM SPECIFICATION

C 1. The Overall Well Design Scheme

The design scheme is shown in the Figure C.1. The main parts are explained in the Table C.1.

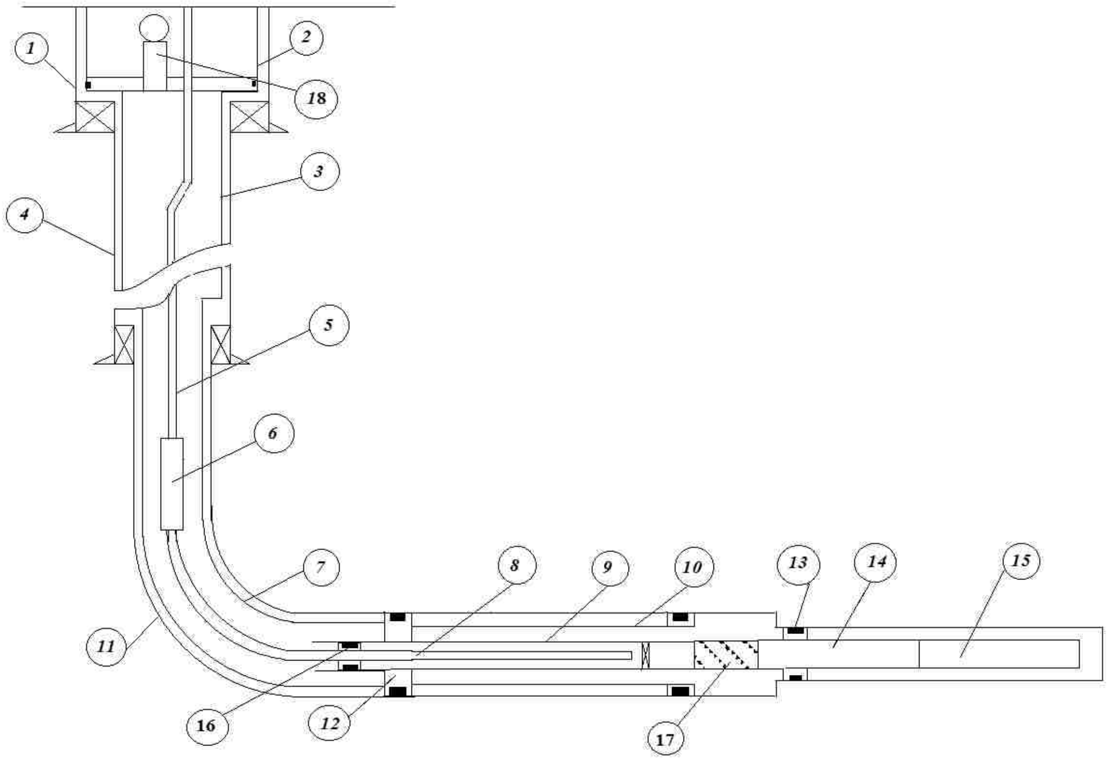

Figure C.0.1: Overall specification scheme (not to scale).
Only one brine pump assembly is shown.

Table C.0.1 Overall Well specification

#	Name	Data
1	Surface casing	20” OD
2	Production casing	16” OD
3	Intermediate casing	9 5/8” OD
4	Intermediate casing	13 5/8” OD
5	Production tubing	5” OD
6	*w.f.* ESP	Schlumberger ESP D5800N 67 stages
7	Production casing	7” OD

8	Production tubing	2” OD	
9	Tubing	4” OD	
10	Screen pipe	6.625” OD	
11	Casing	9 5/8” OD	
12	DHE Packer	9 5/8” OD	
13	ESP Packer	6.0” OD	
14	ESP	REDA ESP SN8500	
15	Casing	6 5/8” OD	
16	Dual string packer	6 5/8” OD	
17	Perforated tubing	6 5/8” OD	
18	Turbine-generator	Single stage axial turbine	
		Blades radius	2.5 inch
		Shaft revolutions	19,000 rpm
		Electric power produced	297.4 kW

C 2. Casing Design

The casing design was done for the chosen casing scheme with setting depths borrowed from the already drilled well Beulah Simon #2 (McCoy,1980). The following results contain burst/collapse calculations of all segments of the casing program. The casings selection is done by assuming the maximum allowable stresses and safety margins for the worst case scenarios (Rahman, 1995).

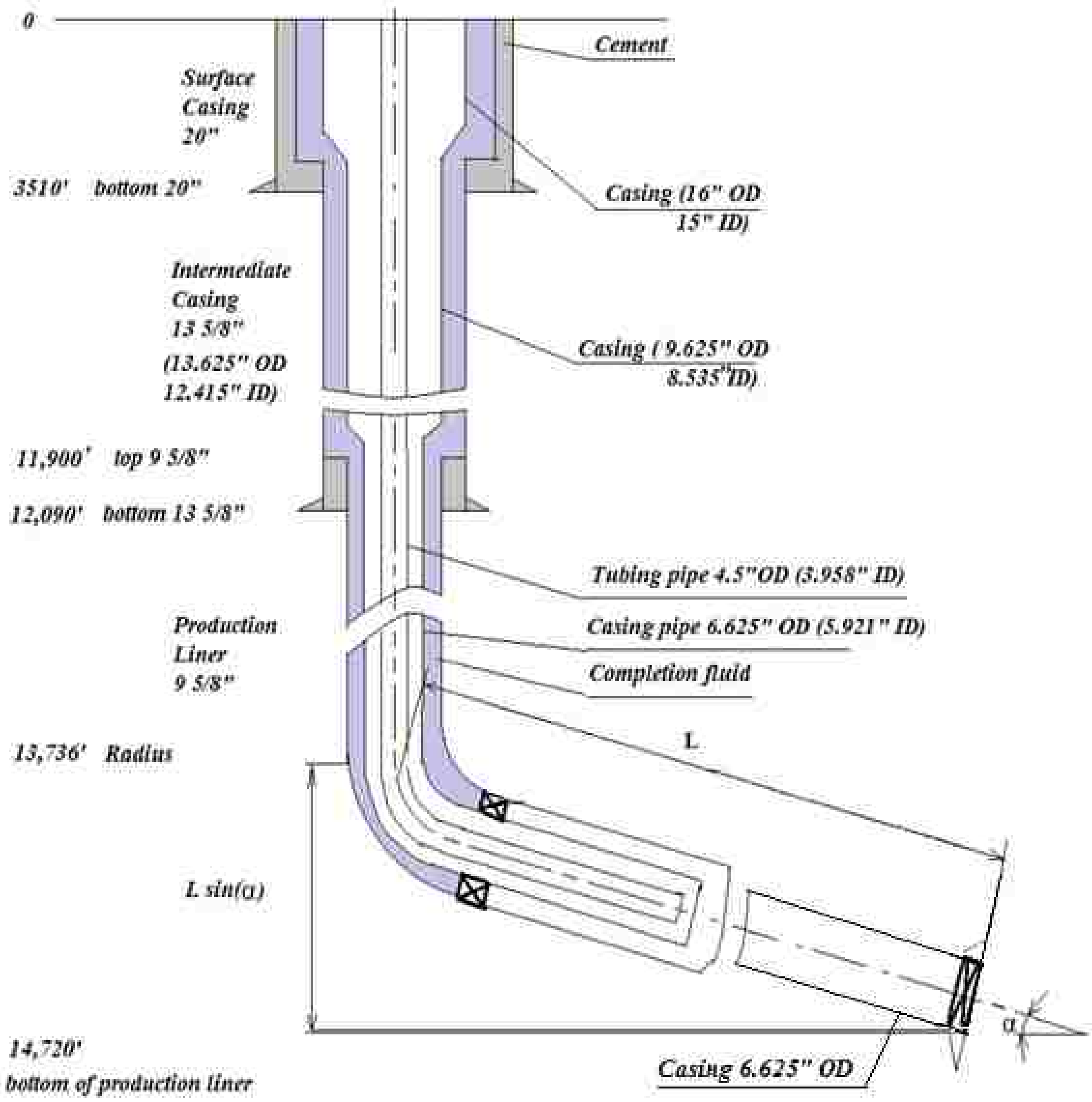

Figure C.0.2: Casing program.

Table C.0.2: Input data for surface casing calculations

Pore pressure gradient, psi/ft	0.465
Mud weight, ppg	17.8
Collapse Safety Factor	1.1
Burst Safety Factor	1.2
Pore pressure below 12,555 ft	$P = 5838.43+3.31*(D-12,555)$
Surface casing pipe 20” OD, inch	20
Fracture pressure gradient on the interval 0-3500, ppg	18

Table C.0.3: Surface casing design calculation results

#	Grade	Weight lb/ft	Collapse resistance	Burst resistance	Interval, ft	Body yield str. 1000lbs	ID inch	# of stands
1	J-55	106.6	770	2410	0-990	1685	19	33
2	K-55	133	1500	3060	990-2910	2125	18.73	64
3	K-55	169	2500	3910	2910-3510	2692	18.376	20

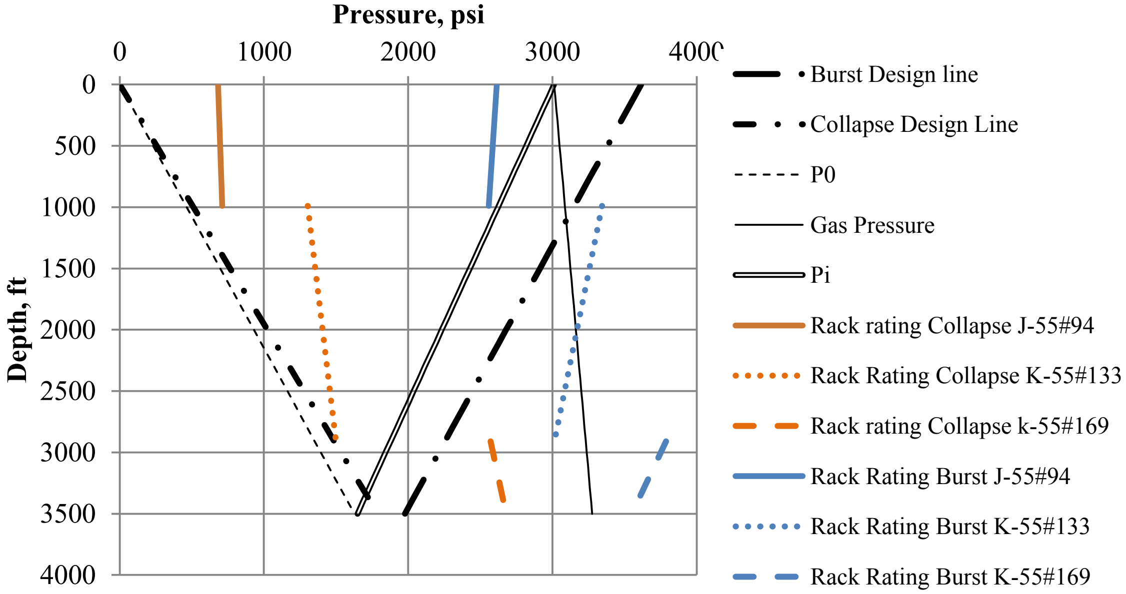

Figure C.0.3: Surface casing burst collapse design diagram.

Table C.0.4: Intermediate casing input data

Intermediate casing pipe, inch	13.375
Depth, ft	12100
Pore pressure gradient, psi/ft	0.465
Mud weight, ppg	17.8
Fracture pressure gradient at 12100’, ppg	18.4
Collapse SF, ppg	1.1
Burst SF	1.2
BOP pressure, psi	5000

Table C.0.5: Intermediate casing design calculations result

#	Grade	Weight Lb/ft	Collapse resistance	Burst resistance	Interval, ft	Body yield str. 1000lbs	ID inch	# of stands
1	HCP-110	68	2910	6910	0-2610	2139	12.415	87
2	V-150	72	2880	10090	2610-5610	3115	12.347	100
3	HCQ-125	80.7	4990	9490	5610-9750	2914	12.215	138
4	HCQ-125	86	6240	10220	9750-12090	3129	12.125	78

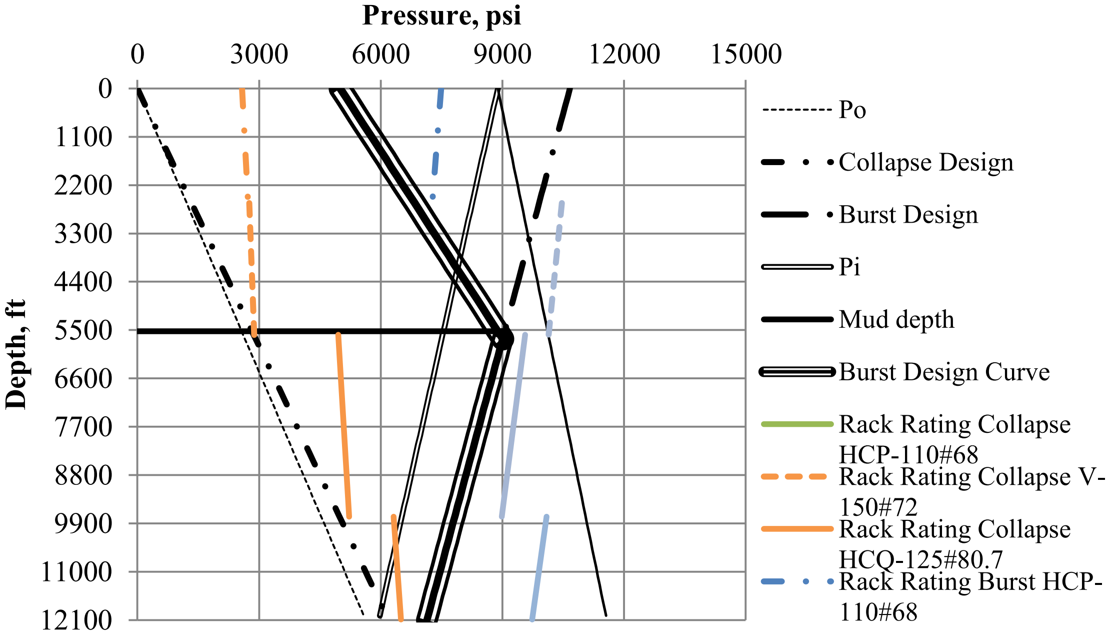

Figure C.0.4: Intermediate casing burst collapse design

Table C.0.6: Production casing design calculations result

Production Casing pipe, inch	9.625
Depth, ft	14720
Pore pressure gradient, psi/ft	0.465
Mud weight, ppg	17.8
Fracture pressure gradient, ppg	18.6
Collapse SF	1.1
Burst SF	1.2
Pore pressure below 12,100ft	*P=5838.43+3.31*(D-12,555)*

Top of pressured zone is at 12,555.77ft with pressure of 5838.43 psi (from P=0.465*D)

Pressure at target depth is 13,015 psi (drilling data from Dobson, 1980)

Table C.0.7: Production casing calculation results (assuming vertical well)

#	Grade	Weight lb/ft	Collapse resistance	Burst resistance	Interval, ft	Body yield str. 1000lbf	ID inch	# of stands
1	V-150	53.5	8960	14860	11,900-13,190	2332	8.535	43
2	T-95	75.6	14430	13770	13,190 - 14720	2100	8.031	51

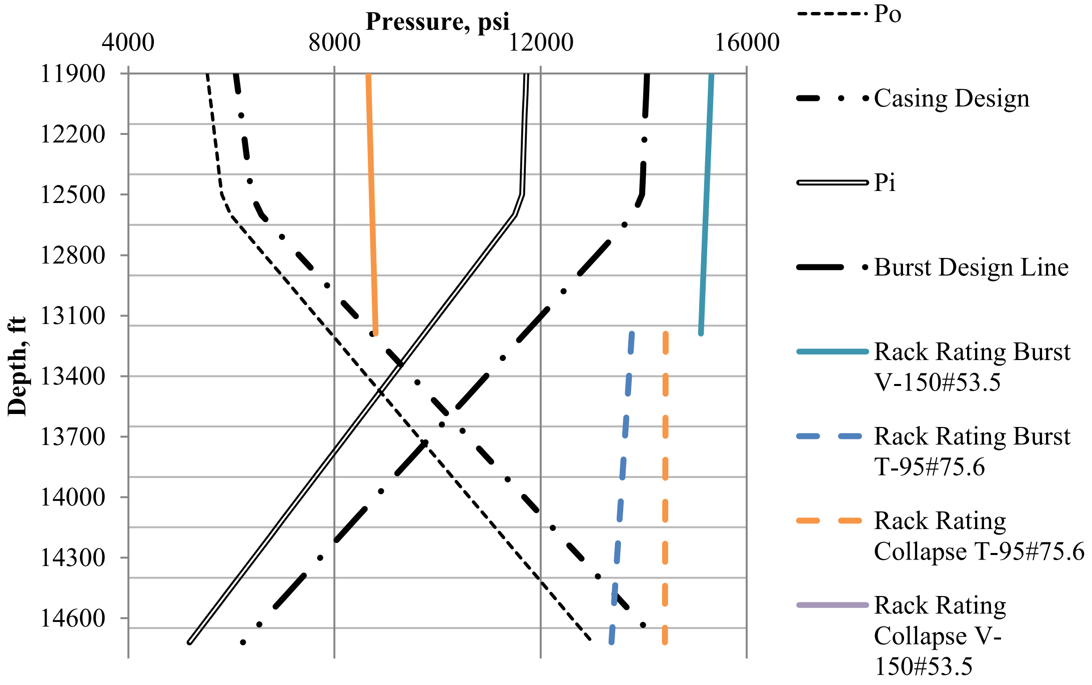

Figure C.0.5: Production casing burst collapse design.

C 3. Bending Force of the Last Casing String

The last casing is a subject to bend to maximum 90 degrees with horizontal well completion design. Assuming uniform contact with the borehole the calculation results in the Table 0.6 were performed according to Rahman's book. The total length of the last segment casing T-95 consists of 1225.2 ft of vertical section, 478.56 ft of bending section, and 914.4 ft of horizontal offset.

Table C.0.8: Bending stress calculation results

Cross sectional area, inch^2	Axial stress w/o bending, psi	Additional stress to bending, psi	Total stress in a pipe, psi	Minimum acceptable yield stress, psi
22.0928	7,515.28	39,031.644	45,546.924	95,000

Table C.0.9: Hook Load calculations

	Surface casing	Intermediate casing	Production casing
Hook Load, lbs	338,450.9	422,108.1	149,873

C 4. System Design

The detailed scheme of the completion design is shown in the Figure C.7. Here, the DHE is connected in series with two ESP assemblies with packers and extension tubings. Basically, the outer DHE pipe is continues as extension pipe and connected to the ESP. This simplifies the installation to one single down trip operation. Two ESP assemblies are necessary for emergency case if one of the pumps would stop working. In this case the well intervention is not needed. The second ESP will continue brine circulation. To rearrange the flow the bypass valve is actuated. The OD of the ESPs assemblies was chosen in such manner that allows installation through the ICD portion of the well. The cable cord is running from the surface and connected to the tubing, *w.f.* pump, DHE, and extension pipe to the ESPs by clips. When the setting depths are reached for each part, the electrically driven packers are actuated simultaneously.

Table C.10: Horizontal well data

	Production side 250m (820.21 ft)
Casing	9 5/8 inch OD
Perforations	1 inch perforations with 20 shots per foot.
Gravel Pack	20/40 size sand with 135D permeability
ICD Screen pipe	6.655 inch ID
	Insulation interval 800m (2624.67 ft)
Casing	7.0 inch ID
	Injection side 15m (52.5 ft)
Perforations	0.6 inch perforations with 10 shots per foot
Extension pipe	5 inch OD (see Figure 0.6) used for open hole completion

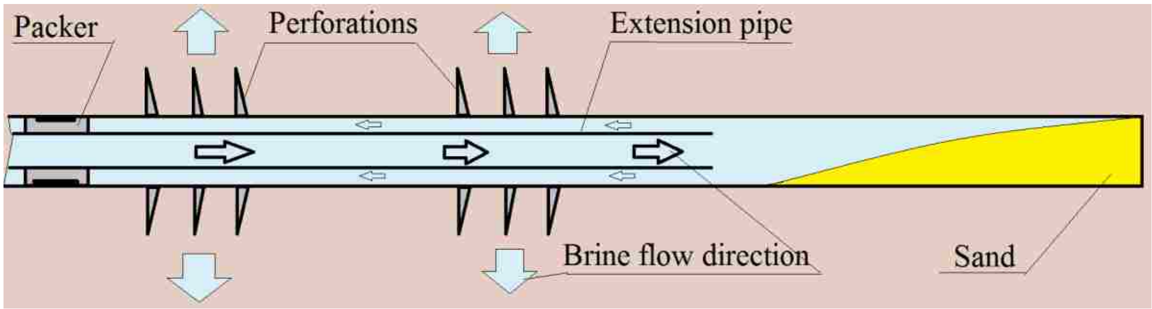

Figure C.0.6: Injection side design scheme, when no casing is used.

Table C.11: Geometric data of chosen casings and tubing in DHE

		DHE size, m
Casing 1	Diameter inner	0.1536
	Diameter outer	0.1936
Casing 2	Diameter inner	0.2190
	Diameter outer	0.2445
Cement sheath	Diameter outer	0.3105
Coiled tubing	Diameter inner	0.1143
	Diameter outer	0.1000

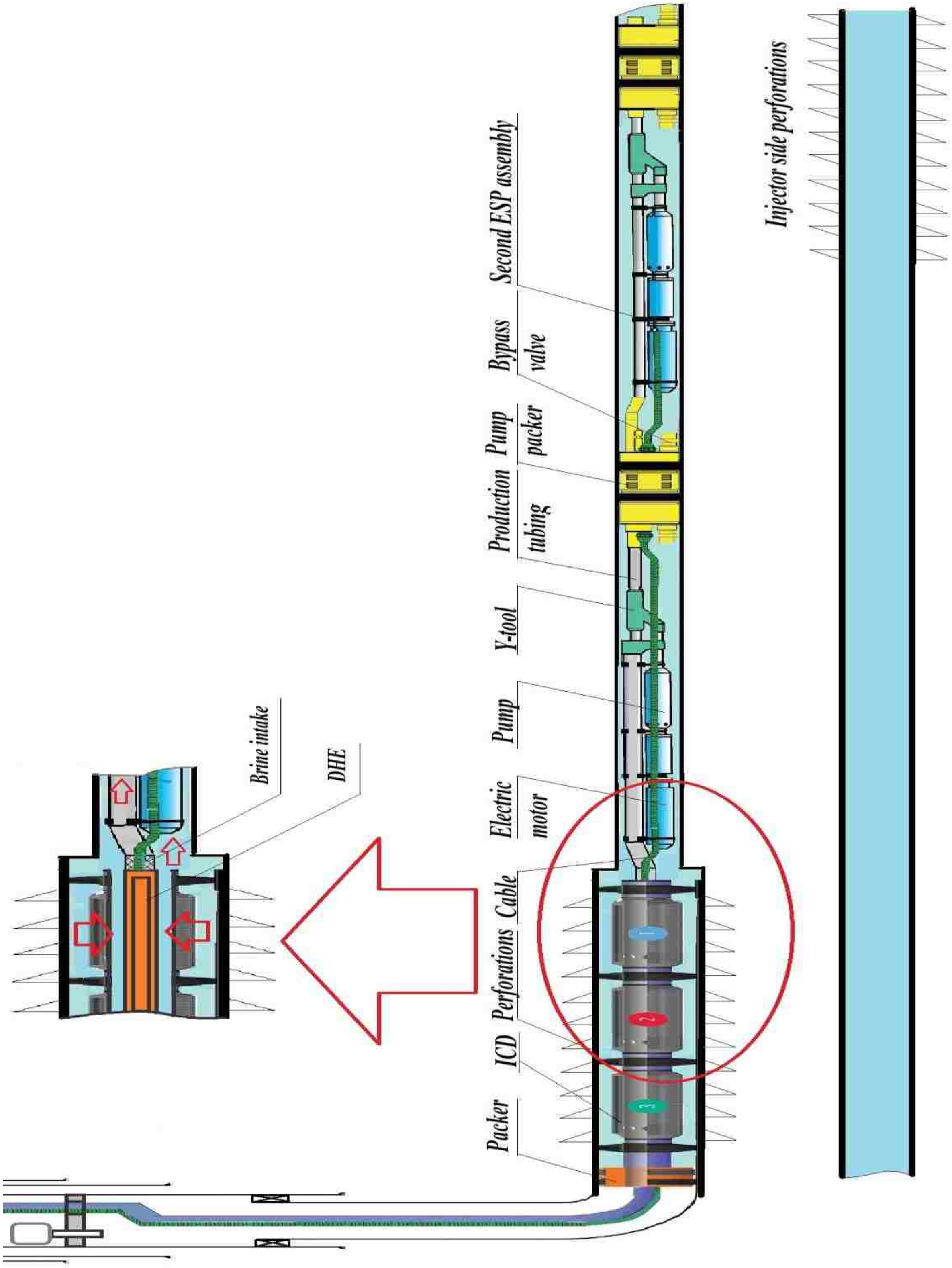

Figure C.0.7: Completion design. Modified from (Centrilift, B. H., 2008).

The *w.f.* pump assembly is illustrated in the Figure C.8. The assembly is installed inside the 7” tubing, which is sealed on both sides. The shell design is demountable. The standard ESP is located inside the shell. The *w.f.* enters from the top, cools the electric motor, captures by the pump and leaves from the exit. The load tubing is holding the entire weight of the assembly. The *w.f.* ESP assembly can be hanging on the load tubing inside the casing or additional dual string packer can be involved into design scheme to support the pump and provide hot stream flow through the packer.

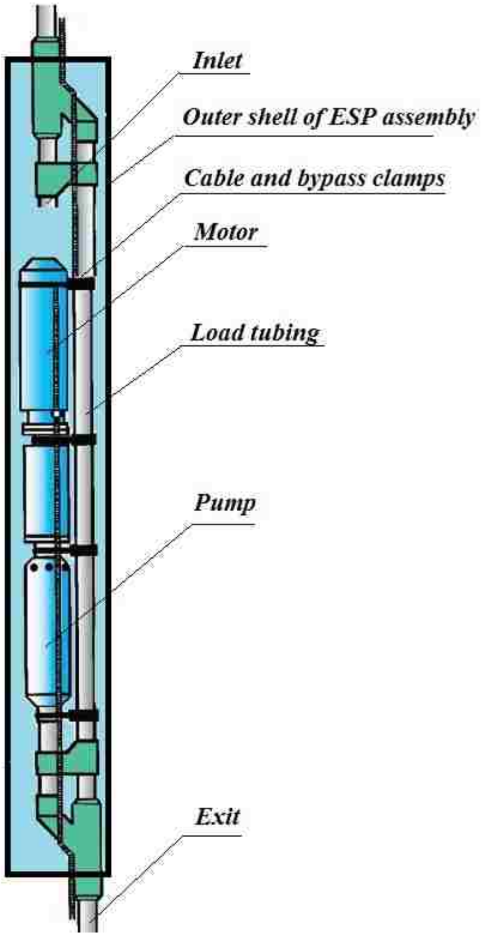

Figure C.0.8: *W.f.* ESP assembly. Modified from (Centrilift, B. H., 2008).

One of the important aspects of the system is insulation. The cold and hot side tubings should be insulated in order to achieve mentioned power production. Insulation should be compact in size, very effective, and thermally and chemically resistant to reaction with carbon dioxide. One of the suggestions is Hyperlast Offshore Technology used by The Dow Chemical Company. The insulation material has low thermal conductivity of 0.15 W/m*K and used in offshore petroleum industry for over 30 years.

The most valuable device of the system is the brine ESP. There are several cases when ICD completion was protected by the gravel pack. The procedure of gravel packing the outer space of the ICD is well explained in (Augustin et al., 2006) as a real industry example. The gravel pack sand is pumped between the ICD OD and casing ID through the industry available tools. However, the classical gravel packing method is complicated, costly, and is not suitable in this project. If the gravel packed system is implemented, the brine pump assembly is required to squeeze through the screen pipe initial diameter. There is a great chance to ruin the completion in this case. Thus, the ICD and the sand prepacked screened protection used by Baker Hughes is a better choice, which is completed into one peace with the DHE installed inside. The brine pumps connected to the DHE through the perforated tubing. In this way the power cable for the pumps is fastened by the clamps along the entire system parts to the surface.

All ICD completions have standalone-screen filtration technique to protect the device from unwanted sand invasion (Henriksen et al. 2005). As an innovative proposal may be interesting the idea of using the gravel pack sand of different mesh size as a pressure resistance in the ICD instead of complicated multipath design. At this technique the prepacked screen pipe will work as a pressure resistance and protect the equipment from the sand invasion. Then the prepacked screen pipes with different size sand filling are separated by the packers to achieve desired brine inflow control.

C 5. Surface Equipment

The switchboard is needed to manage the electric power distribution of the unit, as well as make an electric arrangement of the electric system (Figure C.9).

Figure C.0.9: Electrostart ESP switchboard.

The approximate electric scheme is shown in the Figure C.10.

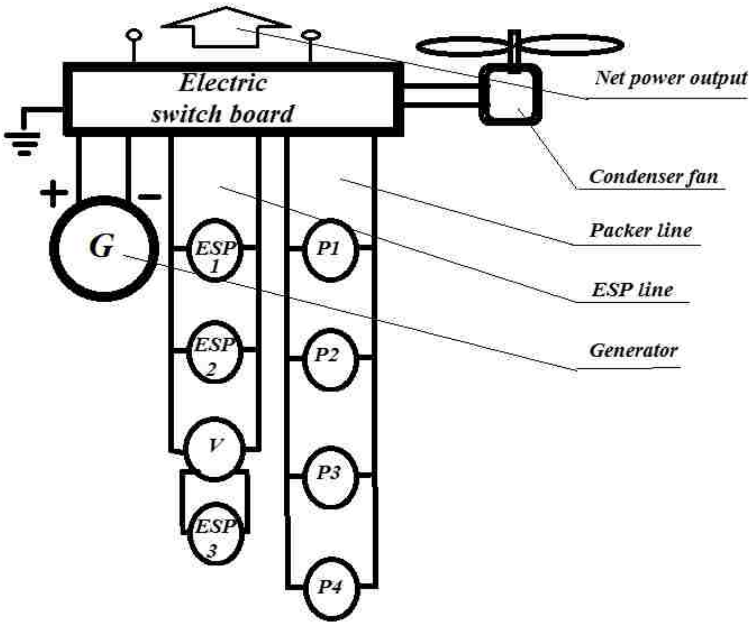

Figure C.0.10 Approximate electric scheme.

The- electric switchboard distributes electric power generated in the system to condenser fan, ESP line, Packers line, and consumer. The ESP line consist of three pumps connected in parallel. In case of one brine ESP is off the second ESP with bypass valve (V) is actuated. The packer line is used to actuate packers at the installation work.

The air driven condenser is used to cool the working fluid. Simple scheme is shown in the figure C.11. The red and blue arrows show the *w.f.* hot inlet and cold outlet. The air is driven vertically up.

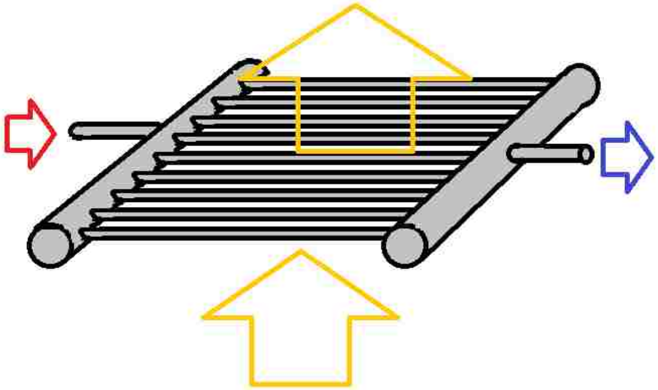

Figure C.0.11: Condenser schematic.

Table C.12: Condenser parameters

Parameter	Value
Outer diameter tubing, m	0.03
Wall thickness, m	0.001
Tubing Material	Copper
Length, m	16
Tubing thermal conductivity, W/mK	385
Tubing wall roughness, m	2e-6
Number of tubings	250
Distance between tubings, m	0.02

APPENDIX D SYSTEM INSTALLATION PROCEDURE

The system installation procedure is introduced in the Table D 01. The installation process is described starting from the perforation operation after the casing design is already run and cemented. After the perforation work, the system is run into the well as a whole assembly (starting from brine pumps and finishing with tubing holder) at one trip. The main parts of the system such as w.f. packer and pump, cold stream tubings, turbine assembly with the packer will be running together inside the production casing. As soon as the brine pump assembly is reached the TD and tubing is set in the wellhead, the electric signal initiates the packers latching mechanisms simultaneously. The next step is electric wiring work according to the scheme; checking the circulations of the brine and *w.f.* loops; connection the w.f. condenser with the wellhead through the safety valves; substitution of the completion fluid by the liquid CO_2, and running the system with necessary adjustments to receive the maximum net power production.

Table D 0.1: System installation procedure

Step	Operation	Notes
1	Run perforation gun into the well to the 18,352.23 ft MD.	Injector perforation
2	Perforate 16m (52.5ft) length injector side	
3	Remove perforation gun	
4	Run perforation gun into the well to the 14,907.35 ft MD.	Producer perforation
5	Perforate 200m length producer interval	
6	Remove perforation gun	
7	Pumping test to ensure that both perforation intervals (producer and injector) provide the required flow rate. If required, increase perforation length	

8	Run two brine pump assemblies 5.5 OD with packers 7.0 OD at 15,000 ft MD	Running the system into the well occur at one trip. The system run starts from two brine pump assemblies with packers, DHE with ICD and prepacked screens, tubings, and *w.f.* pump. The final equipment is turbine assembly with packer.
9	Run 100 ft 5.5 inch perforated pipe as a separation interval from the DHE. The brine will enter the pipe through the perforated holes and later the ESP. Clips the cable to the hanging tubing.	
10	Run ICD into the 14,907.35 ft MD with DHE inside of the prepacked sand screens 250m (820.21 ft)	
11	Run the DHE packer and the outer production tubing assembly. Setting depth is 1409.35 ft MD right after the bending section.	
12	Run 5inch OD 515.35 ft length insulated tubing, connected to the DHE packer by additional packer 7 inch OD.	
13	Run *w.f.* pump assembly, connected to the insulated tubing.	
14	Run 5 inch OD tubing above the *w.f.* ESP.	
15	Run Turbine dual string packer with turbine-generator assembly on top. Setting depth is 20 ft below the surface.	
16	Run 5 inch cold stream tubing to the well head.	
17	Connect the cold stream tubing to the well head by tubing holder	
18	Connect power cable to the electric switch board.	
19	Latch all packers at ones using the power cable installed with the system in previous steps.	
20	Circulate the *w.f.* zone by the w.f. pump. Check for the integrity of the system.	
21	Drive the brine by brine pump and check the temperature change at the DHE and flow rate.	Starting the system
22	Connect the condenser to the wellhead.	

23	Substitute completion fluid in the *w.f.* zone (vertical well and horizontal DHE section) by carbon dioxide fluid.	
24	Start the system. Maintain the brine and *w.f.* flow rates as prescribed for this particular application, check the temperature of the *w.f.* at the DHE and condenser.	

Total measured depth is 18,404.73 ft (From the top to the end of injector perforations).

VITA

Ildar Akhmadullin, was born in 1974, Zainsk, The Union of Soviet Socialist Republics (USSR), received his Bachelor Degree at Kama State University (1996) and Master's Degree at the University of Texas at San Antonio (2010), both in Mechanical Engineering. He was accepted into the LSU Graduate School majoring in Petroleum Engineering in 2012. He anticipates graduating with his Ph.D. degree in August 2016. He plans to continue promoting LSU for many years to come.